CARBON NANOFIBER LAYERS ON METAL AND CARBON SUBSTRATES

PEM fuel cell and microreactor applications

Sergio Pacheco Benito

Graduation committee

Prof. Dr. G. van der Steenhoven, chairman	University of Twente
Prof. Dr. Ir. L. Lefferts, promoter	University of Twente
Dr. A. van Houselt, referee	University of Twente
Prof. Dr. Ir. R.G.H. Lammertink	University of Twente
Prof. Dr. Ir. H.J.M. ter Brake	University of Twente
Dr. Ir. D.C. Nijmeijer	University of Twente
Prof. Dr. F.A. de Bruijn	University of Groningen
Dr. J.H. Bitter	University of Utrecht

The research described in this thesis was carried out at the Catalytic Processes and Materials group of the MESA+ Institute for Nanotechnology and Faculty of Science and Technology of the University of Twente, P.O. Box 217, 7500 AE Enschede, The Netherlands.

This project was financially supported by of the Dutch CW/NWO organization under the project No. 700.55.028.

Cover design: Sergio Pacheco Benito and Bert Geerdink

Printed by: CPI Koninklijke Wöhrmann, Zutphen, The Netherlands

ISBN: 978-90-365-3267-9

Author´s email: ser_pa_ben@yahoo.es

CARBON NANOFIBER LAYERS ON METAL AND CARBON SUBSTRATES

PEM fuel cell and microreactor applications

DISSERTATION

To obtain the degree of doctor at the University of Twente,

on the authority of the rector magnificus,

Prof. Dr. H. Brinksma,

on account of the decision of the graduation committee

to be publicly defended on

Wednesday 26th October, 2011 at 16:45

by

Sergio Pacheco Benito

born on 19 December 1978

in San Sebastián, Basque Country (Spain)

This dissertation has been approved by the promoter

Prof. Dr. Ir. L. Lefferts

To my family and to those that believe in me

"Happiness is not a station you arrive at, but a manner of traveling" (Margaret Lee Runbeck)

"Happiness is not having what you want, but wanting what you have" (Crystal Bennett)

Summary

Carbon nanofibers (CNFs) are small graphitic materials, diameters <100nm, with high surface area and inertness. The growth and immobilization of CNF layers directly on microstructured substrates is interesting to avoid the risk of breathing loose CNFs and facilitate the production of functional substrates. Moreover, the mechanical strength and permeability of the substrate are enhanced by the growth of a CNF layer, which is further used as catalyst support. This thesis describes the preparation of CNF layers on flat and porous substrates and their application as catalyst supports for chemical and electrochemical gas-liquid-solid (G-L-S) catalytic reactions. The last part describes the water wettability properties of CNF layers that can have application in microfluidic devices.

Chapter 2 focuses on the synthesis of homogenous and well-attached CNF layers on flat metal substrates by the decomposition of C_2H_4 at 600°C. Metal nanoparticles growing CNFs are easily formed from NiO, in contrast to Fe and Co oxides, leading to higher carbon deposition rates. However, high activity towards total carbon deposition is generally detrimental for obtaining well-attached and homogenously distributed CNFs, as mainly occurs with Ni and mumetal. CNFs grown from Co and Fe foils are averagely well-attached but not homogenously distributed. Stainless steel presents homogeneous and well-attached CNFs at relatively low carbon growth rates.

Chapter 3 reports on the attachment of CNF layers grown at 450°C. Dense carbon (C) and entangled CNF layers are deposited on all Ni foils after either oxidation or oxidation-reduction pretreatments. CNFs are more crystalline than the C layer, although the addition of H_2 during the reaction increases the amount of defects. Both C and CNF layer thicknesses increase with growth time, but the mechanical stability decreases with growth time, especially for oxidized-reduced samples. Thus, samples oxidized at 500°C generally show better mechanical stability than oxidized-reduced samples at 700°C. The preparation of stable and thick CNF layers on Ni foils involves a compromise between the deposition of a thick C layer and the amount of weakly attached CNFs.

In Chapter 4 a CNF layer is grown on a porous stainless steel substrate. Pd nanoparticles deposition on the CNFs is performed for the catalytic reduction of nitrite (NO_2^-), in an aqueous solution, with H_2. The presence of the CNFs on the stainless steel surface had a significant effect on the reactor performance. Even without the presence of H_2 and Pd, the NO_2^- ions were successfully reduced, which was confirmed by the disappearance of NO_2^- reactant and formation of ammonia (NH_4^+). We proposed that the reductive properties of Fe nanoparticles, which are located at the tip of the grown CNFs, are responsible for the reduction of NO_2^- without hydrogen supply.

Chapter 5 reports the growth of a CNF layer and subsequent Pt nanoparticles deposition on a carbon paper substrate for the electrocatalytic oxygen reduction reaction (ORR). Pt nanoparticles are more superficially located when sputtered than Pt when deposited by the polyol method. The Pt electrochemical surface area, when deposited on CNFs, is much higher than that obtained for commercial Pt/Vulcan. The intrinsic ORR kinetic current increases with Pt loading and is higher for samples prepared by the polyol method. Samples prepared by the polyol method suffer more from internal mass transfer limitations than Pt/Vulcan due to a deeper Pt location. However, the external oxygen diffusion is higher for Pt/CNFs, as compared to Pt/Vulcan, due to the intrinsic morphology of the CNFs that allow a better accessibility to oxygen diffusion.

In Chapter 6 CNF layers are grown on Ni foils at 450°C. The addition of 5% H_2 produces thicker, rougher and more porous CNF layers than when 1% H_2 is used. The roughness and porosity increases with reaction time when 5, 10 or 20% H_2 are used. The water wetting properties of the samples are more significantly influenced by the CNF layer thickness than both surface roughness and porosity. When the CNF layer is thicker than ca. 20μm, the surface is hydrophobic and the contact angle increases with surface roughness and porosity. When the CNF layer is thinner than ca. 20μm, the surface is hydrophilic and the contact angle decreases with increasing surface roughness and porosity. This behavior is attributed to penetration of water, making contact with the hydrophilic C layer.

Samenvatting

Koolstof nanofibers (CNFs) zijn kleine grafitische materialen, diameter <100nm, met een groot oppervlak en inertie. De groei en immobilisatie van CNF lagen direct op micro gestructureerde substraten is interessant om het risico losse CNFs in te ademen te vermijden en de productie van functionele substraten te vergemakkelijken. Bovendien zijn de mechanische sterkte en permeabiliteit van de ondergrond versterkt door de groei van een CNF laag, die verder wordt gebruikt als katalysator ondersteuning. Dit proefschrift beschrijft de bereiding van CNF lagen op vlakke en poreuze ondergronden en hun toepassing als katalysator, ondersteund voor chemische en elektrochemische gas-vloeistof-vaste (G-L-S) katalytische reacties. Het laatste deel beschrijft de eigenschappen van water bevochtiging van CNFs welke toepassing in microfluïdische apparaten kan hebben.

Hoofdstuk 2 richt zich op de synthese van homogene en goed bevestigde CNF lagen op vlakke metalen ondergronden door de ontbinding van C_2H_4 op 600°C. Metalen nanodeeltjes groeiende CNFs worden gemakkelijk gevormd uit NiO, in tegenstelling tot Fe en Co oxides, wat leidt tot een hogere koolstof afzetting. Echter, hoge activiteit naar totale koolstof afzetting is over het algemeen nadelig voor het verkrijgen van goed vastgemaakt en homogeen verdeeld CNFs, zoals vooral gebeurt met Ni en mumetal. CNFs uitgegroeid op Co en Fe folies zijn gemiddeld goed gehecht, maar niet homogeen verdeeld. Roestvrij staal bevat homogene en goed bevestigde CNFs bij relatief lage koolstof groeicijfers.

Hoofdstuk 3 rapporteert over de aanhechting van CNF lagen gegroeid bij 450°C. Dichte koolstof (C) en verstrengeld CNF lagen worden afgezet op alle Ni folies na oxidatie of oxidatie-reductie voorbehandelingen. CNFs zijn kristallijner dan de C-laag, hoewel de toevoeging van H_2 tijdens de reactie de hoeveelheid defecten verhoogt. Zowel de C en CNF laagdiktes nemen toe in tijd, maar de mechanische stabiliteit neemt af, in het bijzonder voor de geoxideerde-gereduceerde monsters. Dus, monsters geoxideerd bij 500°C vertonen over het algemeen betere mechanische stabiliteit dan de geoxideerde-gereduceerde monsters bij 700°C. Bij de bereiding van stabiele en dikke CNF lagen op Ni folies gaat het om een compromis tussen de afzetting van een dikke laag C en de hoeveelheid zwak bevestigde CNFs.

In hoofdstuk 4 wordt een CNF laag gegroeid op een poreus roestvrij stalen ondergrond. Pd nano deeltjes afzetting op de CNFs wordt uitgevoerd voor de katalytische reductie van nitriet (NO_2^-), in een waterige oplossing, met H_2. De aanwezigheid van de CNFs op het roestvast stalen oppervlak had een significant effect op de reactor prestaties. Zelfs zonder de aanwezigheid van H_2 en Pd, werden de NO_2^- ionen met succes teruggedrongen, hetgeen werd bevestigd door het verdwijnen van NO_2^- ionen en de vorming van ammoniak (NH_4^+). We stelden dat de reductieve eigenschappen van de Fe nanodeeltjes, die zich op het puntje bevinden van de gegroeide CNFs, verantwoordelijk zijn voor de reductie van NO_2^- zonder H_2 te leveren.

Hoofdstuk 5 beschrijft de groei van een CNF laag en de daaropvolgende Pt nanodeeltjes depositie op een carbonpapier substraat voor de elektrokatalytische zuurstof reductie reactie (ORR). Gesputterde Pt nanodeeltjes bevinden zich meer aan het oppervlakkig dan wanneer Pt afgezet wordt door de polyol-methode. De Pt elektrochemische oppervlakte, wanneer gedeponeerd op CNFs, is veel hoger dan die verkregen voor commerciële Pt/Vulcan. De intrinsieke ORR kinetische stroom neemt toe met de Pt lading en is hoger voor monsters bereid met de polyol-methode. Monsters bereid met de polyol methode hebben meer last van de interne massa-overdracht beperkingen dan Pt/Vulcan, wat veroorzaakt wordt door een diepere Pt locatie. Echter, de externe zuurstofdiffusie is hoger voor Pt/CNFs, in vergelijking met Pt/Vulcan, als gevolg van de intrinsieke morfologie van de CNFs, die een betere bereikbaarheid tot de zuurstof diffusie toelaat.

In hoofdstuk 6 CNF lagen worden gegroeid op Ni folies bij 450°C. De toevoeging van 5% H_2 produceert dikker, ruwer en poreuzer CNF lagen dan de toevoeging van 1% H_2. De ruwheid en porositeit neemt toe met de reactietijd wanneer 5, 10 of 20% H_2 wordt gebruikt. De water bevochtigings eigenschappen worden sterker beïnvloed door de CNF laagdikte dan door zowel ruwheid van het oppervlak en de porositeit. Wanneer de CNF laag dikker is dan ca. 20µm, dan is het oppervlak hydrofoob, en tevens neemt de contact hoek toe met de ruwheid van het oppervlak en de porositeit. Wanneer de CNF laag dunner is dan ca. 20µm, dan is het oppervlak hydrofiel en de contact hoek neemt af met toenemende ruwheid van het oppervlak en de porositeit. Dit gedrag wordt toegeschreven aan de penetratie van water, contact makend met de hydrofiele C laag

Resumen

Las nanofibras de carbono (CNFs) son pequeños materiales de grafito, diámetro <100nm, con una alta área superficial e inercia. El crecimiento y la inmovilización de las capas de CNFs directamente sobre sustratos microestructurados es interesante para evitar el riesgo de respiración de fibras individuales y facilitar la producción de sustratos funcionales. Por otra parte, la resistencia mecánica y la permeabilidad del sustrato se ven reforzadas por el crecimiento de una capa de CNF, que se utiliza como soporte de catalizador. Esta tesis describe la preparación de capas de CNFs en superficies planas y porosas y su aplicación como soporte de catalizadores para reacciones catalíticas gas-líquido-sólido (G-L-S) químicas y electroquímicas. La última parte describe las propiedades de mojabilidad del agua de las capas de CNFs que pueden tener aplicación en dispositivos de microfluidos.

El capítulo 2 se centra en la síntesis de capas homogéneas y bien adheridas de CNFs sobre láminas planas de metal por descomposición de C_2H_4 a 600°C. Las nanopartículas metálicas que crecen CNFs se forman fácilmente a partir del NiO, a diferencia de óxidos de Fe y Co, dando lugar a mayor cantidad de carbono. Sin embargo, una alta actividad en la deposición de carbono es generalmente perjudicial para la obtención de capas homogéneas y bien adheridas de CNFs, como ocurre principalmente con Ni y mumetal. Las CNFs depositadas a partir de láminas de Co y Fe están en general bien adheridas, pero no repartidas homogéneamente. El acero inoxidable presenta capas homogéneas y bien adheridas de CNFs a tasas de crecimiento relativamente bajas.

El capítulo 3 habla sobre la deposición de CNFs a 450°C sobre substratos de Ni. Una capa densa de carbono (C) y capas de CNFs se depositan después de pretratamientos de oxidación u oxidación-reducción. Las CNFs son más cristalinas que la capa C, aunque la adición de H_2 durante la reacción aumenta la cantidad de defectos. Los espesores de la capa de C y CNFs aumentan con el tiempo, pero la estabilidad mecánica disminuye, especialmente para muestras pre-oxidadas y reducidas. La estabilidad mecánica es mayor para muestras pre-oxidadas. La preparación de capas estables de CNFs implica un compromiso entre la deposición de una capa gruesa de C y la cantidad de CNFs débilmente adheridas.

En el capítulo 4 una capa de CNFs se deposita sobre un sustrato de acero inoxidable poroso. Nanopartículas de Pd se depositan sobre las CNFs para la reducción catalítica de nitrito (NO_2^-), en solución acuosa, con H_2. La presencia de CNFs en la superficie del acero tiene un efecto significativo sobre el rendimiento del reactor. Incluso sin la presencia de H_2 y Pd, los iones de NO_2^- se reducen considerablemente, lo cual fue confirmado por la desaparición de NO_2^- reactivo y la formación de amoníaco (NH_4^+). Proponemos que las propiedades reductoras de las nanopartículas de Fe, que se encuentran en la punta de las CNFs, son responsables de la reducción del NO_2^- sin suministro de hidrógeno.

El capítulo 5 se centra en el crecimiento de capas de CNFs y deposición de nanopartículas de Pt sobre un sustrato de carbón para la reacción electrocatalítica de reducción del oxígeno (ORR). Las nanopartículas de Pt se encuentran más superficiales cuando se emplea el método de bombardeo físico en comparación con el método químico de polyol. El área superficial electroquímica de Pt depositado sobre CNFs es mucho mayor que la obtenida con el Pt/Vulcan comercial. La corriente cinética ORR intrínseca aumenta con la cantidad de Pt y es mayor para las muestras preparadas por el método de polyol. Las muestras preparadas por el método de polyol sufren más de limitaciones internas de transferencia de masa que Pt/Vulcan debido a una mayor penetración del Pt. Sin embargo, la difusión externa de oxígeno es mayor para Pt/CNFs debido a la morfología intrínseca de la CNFs que permiten una mejor accesibilidad para la difusión de oxígeno.

En el capítulo 6, capas CNFs se depositan en láminas de Ni a 450°C. La adición de 5% de H_2 produce capas más gruesas, rugosas y porosas que cuando se usa 1% de H_2. La rugosidad y la porosidad aumentan con el tiempo de reacción cuando se utilizan 5, 10 ó 20% de H_2. La mojabilidad con agua está más significativamente influenciada por el espesor de la capa de CNFs que la rugosidad superficial o porosidad. Cuando el espesor de la capa de CNFs es mayor que ca. 20μm, la superficie es hidrofóbica y el ángulo de contacto aumenta con la rugosidad de la superficie y la porosidad. Cuando el espesor de la capa es menor que ca. 20μm, la superficie es hidrofílica y el ángulo de contacto disminuye con el aumento de la rugosidad superficial y porosidad. Este comportamiento se atribuye a la penetración del agua, haciendo contacto con la capa hidrofílica de C.

Laburpena

Karbono nanofibrak (CNFs) grafito txiki materialak dira, diametroa <100nm dute, azalera handikoak eta bizigabeak dira. CNFs geruzen hazkundea eta ibilgetzea zuzenean sustratu mikroestrukturaduetan egitea interesgarria da banakako zuntz arnasketa arriskua ekiditeko, eta sustratu funtzionalen ekoizpena errazteko. Bestalde, erresistentzi mekanikoa eta sustratuaren iragazkortasuna CNFs geruza baten hazkundearengatik indartuak ikusten dira, non katalizatzaile gisa erabiltzen diren. Tesi honek CNFs geruzen prestakuntza deskribatzen du gainazal lau eta porotsuetan eta bere aplikazioa euskarri katalizatzaileentzat erreakzio gas-likido-solido (G-L-S) katalizatzaile kimiko eta elektrokimikoak. Azken zatian, CNFs geruzen uraren bustigarritasunaren propietateak deskribatzen ditu, non dispositibo mikrofluiduetan aplikazioa izan dezaketen.

Bigarren kapituluan, CNFs geruza homogeneoen eta ondo lotutakoen sintesian oinarritzen da non metalezko xafla lauen gainean C_2H_4 600°C–etan deskonposatzen diren. CNFs-etan hazten diren metalezko nanopartikulak erraz sortzen dira NiO-etatik, Fe eta Co oxidoekin alderantziz, karbono kantitate handiagoa emanez. Hala ere, karbono deposizio-jarduera handi batek arruntki normalean kaltegarria da CNFs geruza homogeneo eta ondo lotutakoentzat, Ni eta mumetalekin gertatzen dena normalean. Co eta Fe xafletatik dauden CNFs metatuak, oro har, ondo lotuak daude, baina ez daude uniformeki banatuak. Altzairu herdoilgaitzak CNFs geruza homogeneo eta ondo lotutakoak ditu hazkunde-tasa nahiko bajuetan.

Hirugarren kapituluan, hitzegiten da CNFs-en gorotza 450°C-etan Ni sustratuen gainean. Karbonozko (C) geruza trinko eta CNFs geruzak gorozten dira oxidazio aurretratamendu eta oxidazio-murrizketa ondoren. CNFs-ak kristalinoagoak dira C geruza baino, haatik, H_2-ren eransketak erreakzioan akatsak haunditzen ditu. C eta CNFs geruzen lodiera denborarekin handitu egiten dira, baina egonkortasun mekanikoa murrizten da, bereziki lagin aurre-oxidatu eta murriztuentzat. Egonkortasun mekanikoa handiagoa da lain pre-oxidatuentzat. CNFs-en geruza egonkorren prestakuntzak eskatzen du C geruza lodi baten gorotza eta CNFs ahulki atxikitako kopuru baten arteko konpromezua.

Laugarren kapituluan CNFs geruza bat altzairu herdoilgaitz porotso sustratu baten gainean metatzen da. Pd baten nanopartikulak CNFs baten gainean metatzen dira, nitrito (NO_2^-) katalitiko baten erredukziorako, ur-soluzioan, H_2-rekin. CNFs-ren presentziak altzairuaren gainazalean eragin nabarmena du erreaktorearen errendimenduan. H_2 eta Pd presentzia gabe ere, NO_2^- ioiak nabarmenki murrizten dira, non NO_2^- erreaktibo eta amoniakoaren formakuntzaren (NH_4^+) desagertzean baieztatu zen. Proposatzen dugu Fe nanopartikulen propietate erreduzitzaileak, CNFs-en puntan aurkitzen direnak, arduradunak direla NO_2^- hidrogenogabeen erredukzioan.

Bostgarren kapituluan CNFs geruzen hazkuntzan oinarritzen da eta Pt nanopartikulen metatzean karbono sustratu batean erreakzio elektrokatalitiko oxigeno murriztatzailearako (ORR). Pt nanopartikulak azalerago aurkitzen dira bonbardaketa metodo fisikoa erabiltzen denean metodo polyol kimikoa erabiltzen denean baino. Pt gorotzaren azalera gainazal elektrokimikoa CNFs-ren gainean handiagoa da Pt/Vulcan komertzialak lortzen duena baino. Prestatutako laginak polyol metodoa erabiliaz, barruko masa transferentzi limitazioa gehiago jasaten dute Pt/Vulcan baino, Pt-ren barneratze handiagoarengatik. Hala ere, oxigeno kanporatze difusioa handiagoa da Pt/CNFs-arentzat CNFs morfologia intrinsekoarengatik, non irisgarritasun hobeagoa eskaintzen duen oxigenoaren difusiorako.

Seigarren kapituluan, CNFs geruzak Ni xafletan metaten dira 450°C-etan. H_2-ren %5-aren gehikuntzak geruza lodiago, latzago eta porotsoago ekoizten du H_2-ren %1 gehitzen denean baino. Latztasuna eta porositatea erreakzio denborarekin handitzen da H_2-an %5, 10 edo 20 erabiltzean. Uraren bustigarritasuna nabarmenagoa da CNFs geruza lodierarekin gainazalaren latztasuna edo porositatearekin baino. CNFs geruza lodia ca. 20µm baino handiagoa bada, gainazal hidrofilikoa da eta kontaktu angulua handitzen da gainazalaren latztasuna eta porositatea handitzen denean. Geruzaren lodiera 20µm baino txikiagoa denean, gainazal hidrofilikoa da eta kontaktu angulua murrizten da gainazalaren latztasuna eta porositatea handitzen denean. Portaera hau uraren barneratzeagatik da, C geruza hidrofilikoarekin kontaktua eginez.

TABLE OF CONTENTS

Chapter 1

Introduction

"A leader is best when people barely know he exists, when his work is done, his aim fulfilled, they will say: we did it ourselves" (Laozi)

1.1 Carbon nanofibers as new functional materials

Carbon nanofibers (CNFs) [1-5] are graphitic materials of 10-100nm (**figure 1.1**) in diameter with high surface area, high thermal and electronic conductivity, high mechanical stability and high inertness. Carbon nanostructures can be produced by catalytic chemical vapor deposition (C-CVD) at high temperatures (400-900°C), arc discharge or laser ablation [6]. C-CVD is widely used in industry and research since it is the most suitable for large-scale production at low cost. In general, the growth of carbon nanostructures requires catalyst nanoparticles (usually Ni, Fe, or Co), a carbon feedstock (hydrocarbon or CO) and high temperatures. The most commonly accepted mechanism for the growth was postulated by Baker *et al.* [7]. According to this mechanism, the hydrocarbon gas first decomposes on the surface of a metal nanoparticle, then carbon diffuses through the particle and finally, it precipitates to form the carbon filament. A general mechanism scheme is shown in **figure 1.2**.

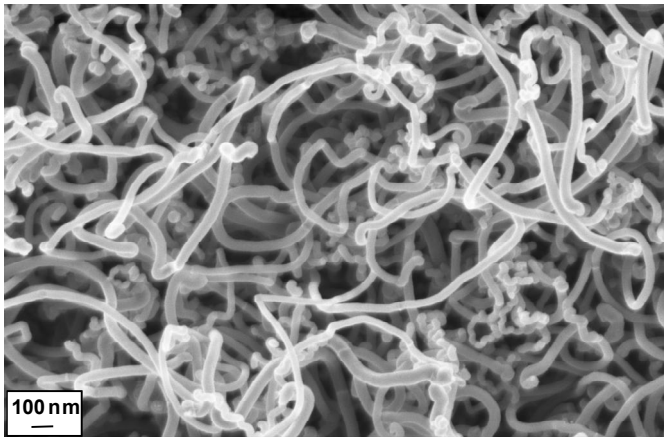

Figure 1.1: *typical scanning electron micrograph of CNFs*

The history of CNFs starts already in 1889 from a US patent [8] reporting the growth of carbon filaments from the decomposition of a carbon containing source in presence of Fe. In the 20th century the research on CNFs was motivated due to the deposition of undesirable carbon filaments on the surface of steam crackers of naphta or ethane (normally made of Fe containing stainless steels) [9-10]. However, the discovery of carbon nanotubes (CNTs) in 1991 [11], and most recently graphene in 2004 [12], has opened a new field of research of these materials. CNFs and CNTs have shown promising results for being used in many

applications such as catalyst supports [13-16], batteries and fuel cells [17-19], hydrogen storage [20-21], polymer reinforcements [22-23], super-capacitors [24] or sensors [25]. Graphene is also considered a promising candidate especially in electronic applications, seen as a potential competitor, or even a future substitute, of silicon.

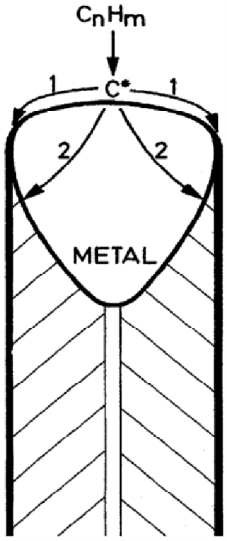

Figure 1.2: *schematic representation of the catalytic growth of a carbon nanofiber: 1) the carbon source decomposes on the surface of the metal particle and carbon atoms are formed; 2) the carbon atoms diffuse through the metal and precipitate in the form of a fiber [4]*

CNFs are often obtained in powder form by the decomposition of a hydrocarbon on pre-deposited metallic nanoparticles on high surface area support material [4, 26]. The size and yield of CNF is a function of the original metal particle size and carbon source [27]. Loose CNFs or CNF agglomerates are usually obtained after refluxing the obtained material in basic and acid solutions to remove the support and the metal particles [28]. However, the growth of CNF layers can also occur directly on polycrystalline flat or macroporous metallic substrates, such as metal foils [29-30], metal foams [31-33] or metal filters [34-37], without further deposition of metal nanoparticles. The controlled growth of homogenous and well-attached layers on these substrates open the possibility of use in applications as microstructured catalyst supports, polymer reinforcements, sensors and materials for enhanced heat transfer [14-15, 38-40].

1.2 Carbon nanofiber layers as catalyst supports

CNFs typically have diameters smaller than 100nm, surface areas higher than 100m^2/g, large pore volume (0,5-2cm^3/g) and minimal or no microporosity (pores smaller than 2nm). When produced in loose powder form, especially in large scale, the handling of the resulting fluffy material might be hazardous. Apart from the danger of breathing them, their small size can induce detrimental pressure drops in fixed-bed catalytic reactions that decrease the performance [41]. Consequently, the direct growth and immobilization of a CNF layer on flat or macroporous microstructured substrates [31-37] becomes of interest. The mechanical strength, permeability and inertness of the substrate can be enhanced by the growth of a high surface area CNF layer, which is further used as promising catalyst support. The CNF layer should show high mechanical strength to prevent catalytic bed plugging, high specific volume in order to afford a high space velocity of the gaseous and liquid reactants, and a high chemical resistance in order to be used in aggressive environments such as highly acidic or basic media [42].

The structure of CNF aggregates, as schematically shown in **figure 1.3**, is suggested to mimic the inverse structure of a conventional porous support material [16], leading to a higher porosity and lower tortuosity that should prevent mass transfer limitations. Tribolet *et al.* [35] reported that the activity of Pd/CNFs synthesized on metal fibers for hydrogenation of acetylene was one order of magnitude higher, as compared to that of Pd/activated carbon, due to efficient heat transfer. Ledoux *et al.* demonstrated that mass and heat transfer limitations of the extremely fast catalytic decomposition of hydrazine (N_2H_4) were overcome by using a CNF layer as catalyst support of Ir [42]. Thakur *et al.* reported on the enhanced mass transfer in the bromate reduction in water after depositing Ru nanoparticles on a CNF layer [43]. Chinthaginjala *et al.* showed fast mass transfer in the hydrogenation of nitrite by using Pd nanoparticles deposited on a thin CNF layer previously grown on a Ni foam [13]. It is the interest of this thesis to study the mass transfer enhancement in aqueous and gas phase of CNF layers grown on metal and carbon substrates, as well as the study of the interaction of water with the CNF layer.

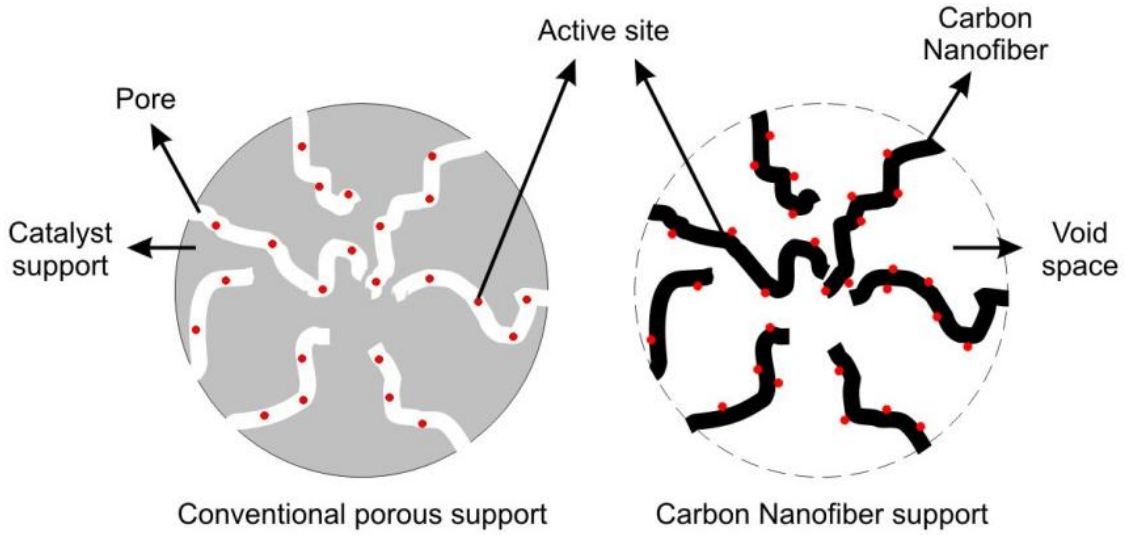

Figure 1.3: *open structure of the CNF support morphology as compared to conventional porous supports [16]*

1.3 Nitrite hydrogenation

Concentrations of harmful nitrogen-containing ions, such as nitrate (NO_3^-), nitrite (NO_2^-) and ammonia (NH_4^+), have increased in the ground waters throughout the world [44]. Sources of these compounds can be attributed to fertilizers, industrial effluents and animal excretion. Although nitrate ions are not directly toxic, they are transformed to harmful nitrite ions *via* reduction processes in the human body. It has been reported that NO_2^- causes blue baby syndrome, and is a precursor to the carcinogenic nitroso-amine as well as hypertension [44-45]. For these reasons, the limit values of the European Community for nitrate, nitrite and ammonium concentrations in drinking water are, respectively, 50, 0,5 and 0,5mg/l. However, for the discharge of waste water the limits are 50 and 10mg/l for nitrate and ammonium concentrations, respectively. Conventional physicochemical techniques, such as ion exchange or reverse osmosis, and biological processes suffer from low selectivity, low conversion and complexity [45]. Catalytic de-nitrification of nitrates and nitrites from aqueous solution *via* hydrogenation over noble-metal solid catalysts is a promising method without the drawbacks of conventional methods [46]. It was reported that over a bimetallic catalyst, nitrate first reduces to nitrite, which in turn is converted to nitrogen and ammonia as a by-product, which is obviously undesired in drinking water. Thus, selectivity to N_2 is of importance.

Hydrogenation of NO_2^- is known to be a fast reaction that induces mass transfer limitations that can be diminished by the use of CNFs as support [13]. Moreover, during this reaction, monometallic catalysts such as Pd or Pt can be used to simplify the complexity of the reaction study. During the catalytic reduction, NO_2^- is converted to nitrogen (N_2) (**eq 1.1**) and the undesired product ammonia (NH_4^+) (**eq. 1.2**). The Pd-catalyzed hydrogenation of nitrite in the presence of hydrogen gas (H_2) typically takes place as follows [47-48]:

$$2NO_2^- + 3H_2 \xrightarrow{Pd} N_2 + 2OH^- + 2H_2O \quad \textbf{(eq. 1.1)}$$

$$2NO_2^- + 6H_2 \xrightarrow{Pd} 2NH_4^+ + 4\,OH^- \quad \textbf{(eq. 1.2)}$$

In this thesis, this fast reaction allows us to test the catalytic activity of Pd nanoparticles deposited on a CNF layer previously deposited on a porous stainless steel tube. It is therefore considered a stainless steel microreactor for nitrite hydrogenation.

1.4 Proton exchange membrane fuel cells

A fuel cell is an electrochemical device that converts hydrogen, or hydrogen-containing fuels, directly into electrical energy and heat through the electrochemical reaction of hydrogen and oxygen into water. They can be continuously fed with a fuel so that the electrical power output is sustained, ideally, indefinitely. In a proton exchange membrane (PEM) fuel cell [49], two half-cell reactions take place simultaneously: the oxidation reaction (**eq. 1.3**, loss of electrons) of H_2 at the anode and the reduction reaction (**eq. 1.4**, gain of electrons) of O_2 at the cathode. The electrons generated travel through the external circuit generating electrical current. These two reactions make up the total oxidation-reduction (redox) reaction of the fuel cell (**eq. 1.5**), which is the formation of water from hydrogen and oxygen gases:

Anode reaction: $2H_2 \rightarrow 4e^- + 4H^+$ **(eq. 1.3)**

Cathode reaction: $O_2 + 4e^- + 4H^+ \rightarrow 2H_2O$ **(eq. 1.4)**

Overall reaction: $2H_2 + O_2 \rightarrow 2H_2O$ **(eq. 1.5)**

Because H_2 and O_2 are converted into water, fuel cells have many advantages over heat engines such as: high efficiency, virtually silent operation and, if hydrogen is the fuel, no pollutant emissions. If the hydrogen is produced from renewable energy sources, such as solar or wind energy, then the electrical power produced can be truly sustainable (**figure 1.4**).

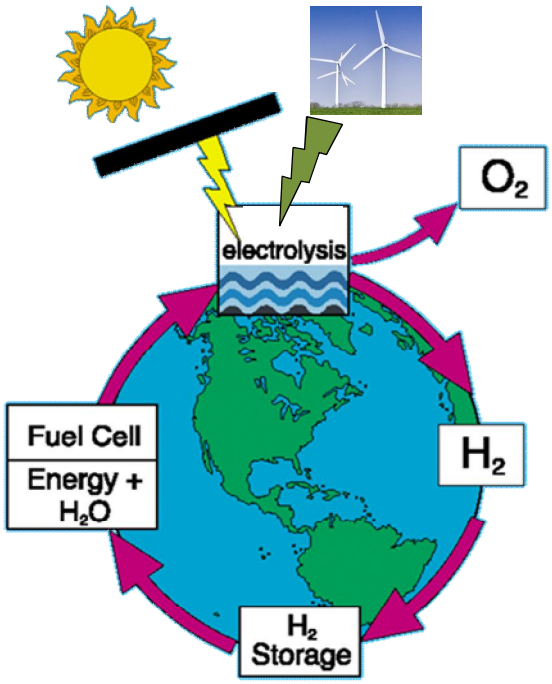

Figure 1.4: *ideal sustainable cycle including the electrolysis of water for producing the H_2 that would feed the fuel cell*

Figure 1.5 shows the main constituents of a PEM fuel cell. Both anode and cathode include a gas diffusion layer and a catalyst layer. In between anode and cathode, a polymeric membrane, such as Nafion®, is sandwiched. The membrane must absorb large quantities of water to conduct H^+ efficiently, being therefore very humidity dependant. Carbon paper and carbon cloths are generally used as gas diffusion layer substrates providing electrical conduction, inertness and mechanical support. Platinum (Pt) is the main component of the catalyst layers since it has the highest electrocatalytic activity and stability for H_2 oxidation and O_2 reduction [50]. However, it is a scarce and expensive metal. The reduction of O_2 is about 100 times slower than that of the oxidation of H_2, thus the cathode reaction limits the power density. To achieve higher efficiency and reduce the usage of Pt, nanoparticles are dispersed on an inert support with high surface area such as

carbon black supports [51]. Moreover, there are mass transport losses resulting from the decrease of the concentration of hydrogen and oxygen at the electrode. For example, with the buildup of water at the cathode, catalyst sites become clogged, restricting oxygen access. It is therefore important to remove this excess water. CNFs have been suggested as new high surface area catalyst supports with high hydrophobicity and low microporosity [17, 52]. The use of a CNF layer directly grown on a carbon paper is suggested in this thesis.

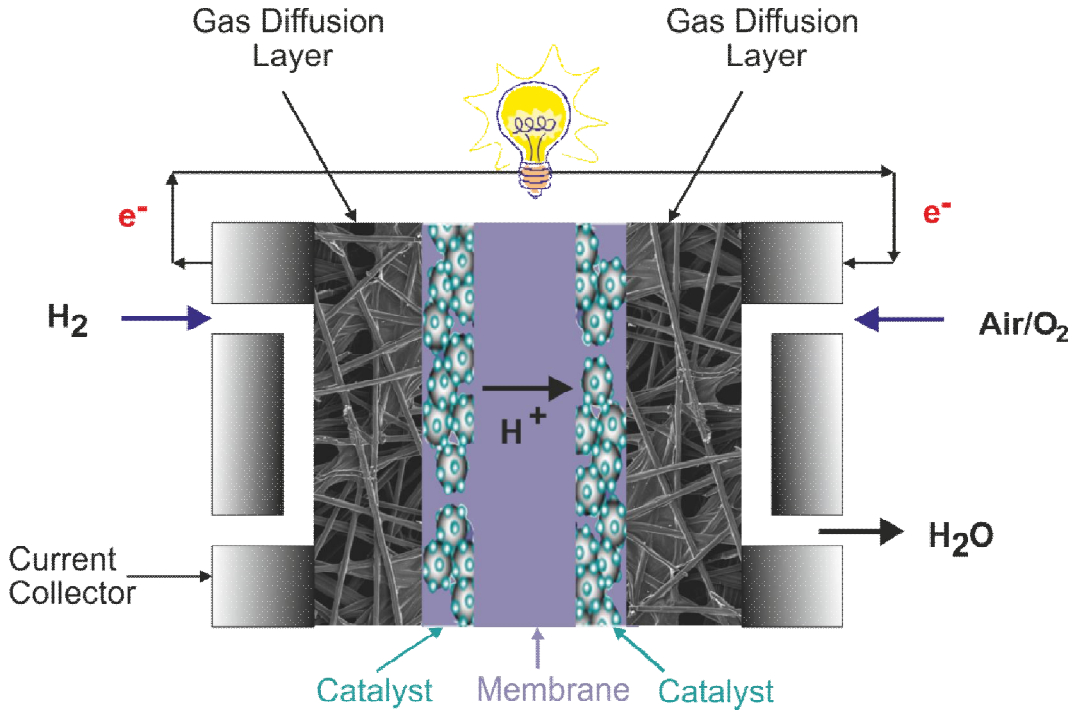

Figure 1.5: *diagram of a single PEM fuel cell showing the different layers. H_2 is introduced in the anode and air or O_2 is introduced in the cathode*

1.5 Wettability of porous layers

One of the properties of porous carbon layers is the ability to possess quite different wetting modes in liquids such as water when varying morphology [53]. Water wettability and repellency are important properties of solid surfaces from both fundamental and practical aspects. The wettability of a surface is assessed by measuring the contact angle that a droplet of water forms on that surface. Surfaces can be hydrophilic, with contact angles <90° or hydrophobic, with contact angles >90° (**figure 1.6**). The wettability of the solid surface strongly depends on both the surface energy of the liquid-solid interface and the surface roughness.

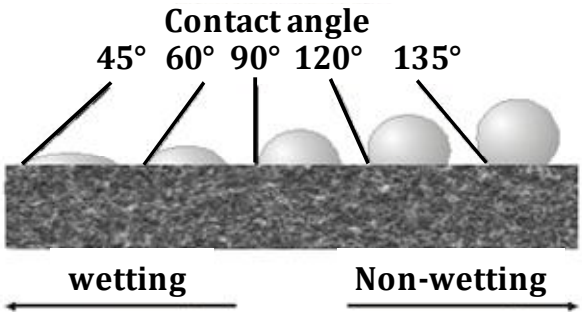

Figure 1.6: *different contact angles of a drop placed on a substrate*

A super-hydrophobic surface, with contact angle higher than 150°, is typically associated with low energy surfaces (such as fluorocarbons or hydrocarbons, but also graphitic materials) and very rough surfaces. There has been intense interest in the preparation and study of super-hydrophobic surfaces [54-59], as well as their applications as self-cleaning surfaces [60] and for drag reduction in microfluidic devices [61-63]. Examples of super-hydrophobic materials in nature [64], such as the lotus leaf, reveal a unique micro- and nano-roughness [65] (**figure 1.7a**). Droplets of liquid adhere strongly or slowly slide on a hydrophilic surface, whereas droplets roll of fast on a super-hydrophobic surface (**figure 1.7b**).

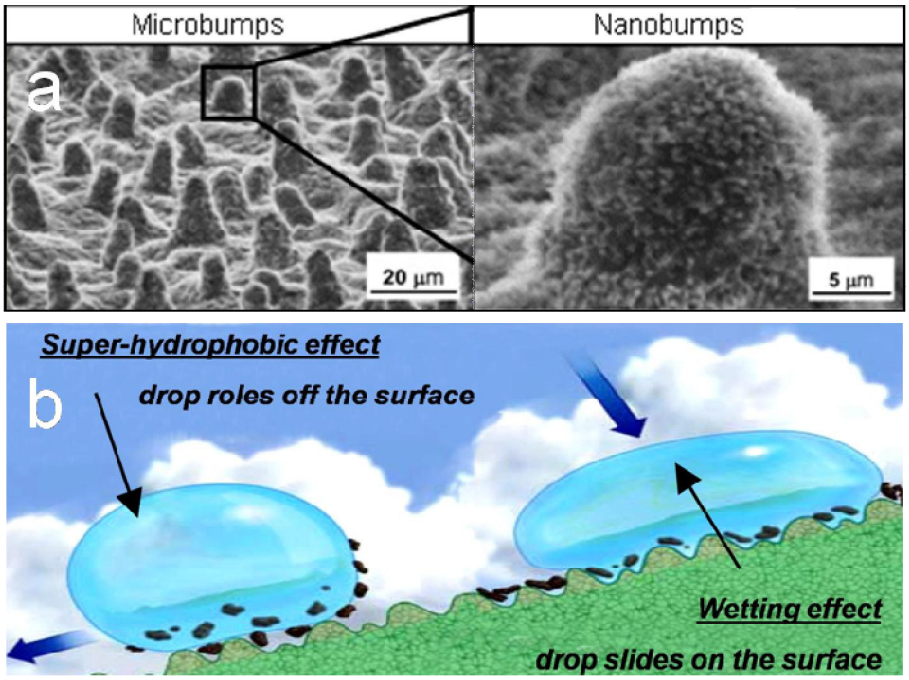

Figure 1.7: *a) micro and nano-bumps on a lotus leaf [65];*
b) different wetting modes on a tilted surface

CNFs or graphitic materials are usually considered hydrophobic, although the water contact angle of dense graphite is slightly below 90° [53, 66-67]. Moreover, the wettability of CNFs can be modified by graphitization treatments [68-69] and incorporation of oxygen groups by gas, liquid or plasma treatments [70-73]. The addition of oxygen normally increases the wettability in water. Hence, CNFs are usually pretreated for increasing the number of anchoring points to deposit metal particles in aqueous solutions. The study of the interaction of small droplets of water with CNF layers can help in the understanding of mass transfer processes in aqueous phase catalytic reactions, as well of the evacuation process of water formed in electrochemical reactions such as in the cathode of a PEM fuel cell.

1.6 Scope and outline of the thesis

The goal of this thesis is the synthesis of CNF layers on flat and microstructured substrates made of metal and carbon, study the influence of reaction parameters on homogeneity, attachment and wettability, and test their performance as catalyst supports in chemical and electrochemical gas-liquid-solid reactions. **Chapter 2** describes the direct growth of CNFs on various metal foils without adding any additional metal particles. The carbon yield of nickel, iron, cobalt or alloys of them are compared. Homogeneity and attachment of the deposited CNFs are presented. **Chapter 3** focuses in more detail on the attachment of the CNF layer to a nickel foil. Here the role of a dense carbon layer present in between the CNF layer and the nickel substrate is reported.

Chapter 4 describes the growth of a CNF layer directly on a porous stainless steel tube to be used as a microreactor. Pd nanoparticles are deposited on the CNF layer and the catalytic reduction (hydrogenation) of nitrite is studied. **Chapter 5** describes the growth of a CNF layer of a porous and microstructured carbon substrate for PEM fuel cells applications. Pt nanoparticles are deposited by means of physical and chemical methods. Moreover, the catalytic activity of the Pt/CNFs is compared with a commercial catalyst.

Finally, **Chapter 6** describes the different wetting modes of the CNF layers deposited on a nickel foil. The effect of the CNF layer thickness, porosity and surface roughness on the contact angle of a water droplet are revealed. **Chapter 7** includes the general conclusions and recommendations.

References

[1] N.M. Rodriguez, J. Mater. Res. 8 (1993) 3233.

[2] J. Rostrup-Nielsen, D.L. Trimm, J. Catal. 48 (1977) 155.

[3] R.T.K. Baker, Carbon 27 (1989) 315.

[4] K.P. De Jong, J.W. Geus, Catal. Rev. Sci. Eng. 42 (2000) 481.

[5] V.V. Chesnokov, R.A. Buyanov, Russ. Chem. Rev. 69 (2000) 623.

[6] T.W. Ebbesen, Carbon Nanotubes: Preparation And Properties. CRC Press, Boca Raton, Florida, 1997.

[7] R.T.K. Baker, M.A. Barber, P.S. Harris, F.S. Feates, R.J. Waite, J. Catal. 26 (1972) 51.

[8] T.V. Hughes, C.R. Chambers, US Patent 405 (1889) 480.

[9] A.I. La Cava, C.A. Bernardo, D.L. Trimm, Carbon 20 (1982) 219.

[10] L.F. Albright, C.F. McConnell, K. Welther, Adv. Chem. Series (1979) 175.

[11] S. Iijima, Nature 354 (1991) 56.

[12] K.S. Novoselov, A.K. Geim, S.V. Morozov, D. Jiang, Y. Zhang*et al.*, Science 306 (2004) 666.

[13] J.K. Chinthaginjala, J.H. Bitter, L. Lefferts, Appl. Catal. A 383 (2010) 24.

[14] N.M. de Almeida Coelho, J.L.B. Furtado, C. Pham-Huu, R. Vieira, Mater. Res. 11 (2008) 353.

[15] C. Pham-Huu, M.J. Ledoux, Top. Catal. 40 (2006) 49.

[16] J.K. Chinthaginjala, K. Seshan, L. Lefferts, Ind. Eng. Chem. Res. 46 (2007) 3968.

[17] K. Lee, J. Zhang, H. Wang, D.P. Wilkinson, J. Appl. Electrochem. 36 (2006) 507.

[18] R. Kannan, V.K. Pillai, J. Indian Inst. Sci. 89 (2009) 425.

[19] R. Chetty, S. Kundu, W. Xia, M. Bron, W. Schuhmann*et al.*, Electrochim. Acta 54 (2009) 4208.

[20] R. Strobel, J. Garche, P.T. Moseley, L. Jorissen, G. Wolf, J. Power Sources 159 (2006) 781.

[21] B. Panella, M. Hirscher, S. Roth, Carbon 43 (2005) 2209.

[22] M.H. Al-Saleh, U. Sundararaj, Carbon 47 (2009) 2.

[23] E. Hammel, X. Tang, M. Trampert, T. Schmitt, K. Mauthner*et al.*, Carbon 42 (2004) 1153.

[24] D. Hulicova-Jurcakova, X. Li, Z. Zhu, R. de Marco, G.Q. Lu, Energy and Fuels 22 (2008) 4139.

[25] M. Trojanowicz, Trends Anal. Chem. 25 (2006) 480.

[26] K.B.K. Teo, C. Singh, M. Chhowalla, W.I. Milne, in: H.S. Nalwa, (Eds.) Encyclopedia of Nanoscience and Nanotechnology, vol 10 (2003) 1.

[27] M.L. Toebes, J.H. Bitter, A. Jos Van Dillen, K.P. De Jong, Catal. Today 76 (2002) 33.

[28] M.K. Van Der Lee, A.J. Van Dillen, J.W. Geus, K.P. De Jong, J.H. Bitter, Carbon 44 (2006) 629.

[29] S. Pacheco Benito, L. Lefferts, Carbon 48 (2010) 2862.

[30] A. Sacco Jr, F.W.A.H. Geurts, G.A. Jablonski, S. Lee, R.A. Gately, J. Catal. 119 (1989) 322.

[31] W. Huang, X.B. Zhang, J. Tu, F. Kong, Y. Ning*et al.*, Phys. Chem. Chem. Phys. 4 (2002) 5325.

[32] N.A. Jarrah, F. Li, J.G. Van Ommen, L. Lefferts, J. Mater. Chem. 15 (2005) 1946.

[33] N.A. Jarrah, J.G. van Ommen, L. Lefferts, J. Catal. 239 (2006) 460.

[34] L. Randall, R.L. Vander Wal, L.J. Hall, Carbon 41 (2003) 659.

[35] P. Tribolet, L. Kiwi-Minsker, Catal. Today 102 (2005) 15.

[36] S.J. Park, D.G. Lee, Carbon 44 (2006) 1930.

[37] F. Xu, X. Liu, S.D. Tse, Carbon 44 (2006) 570.

[38] R.L. Vander Wal, L.J. Hall, Adv. Eng. Mat. 6 (2004) 48.

[39] Y. Yun, R. Gollapudil, V. Shanov, M.J. Schulz, Z. Dong *et al.*, J. Nanosci. Nanotechnol. 7 (2007) 891.

[40] C.R. Dietz, Y.K. Joshi, Nanosca. Microsca. Thermophys. Eng. 12 (2008) 251.

[41] P. Tribolet, L. Kiwi-Minsker, Catal. Today 105 (2005) 337.

[42] M.J. Ledoux, C. Pham-Huu, Catal. Today 102-103 (2005) 2.

[43] D.B. Thakur, R.M. Tiggelaar, Y. Weber, J.G.E. Gardeniers, L. Lefferts*et al.*, Appl. Catal. B: Environmental 102 (2011) 243.

[44] L.W. Canter, Nitrates in ground water. CRC Press, Boca Raton, Florida, 1996.

[45] A. Kapoor, T. Viraraghavan, J. Environm. Eng. 123 (1997) 371.

[46] S. Hörold, K.D. Vorlop, T. Tacke, M. Sell, Catal. Today 17 (1993) 21.

[47] A. Pintar, G. Berčič, J. Levec, AIChE Journal 44 (1998) 2280.

[48] J.K. Chinthaginjala, L. Lefferts, Appl. Catal. B: Environmental 101 (2010) 144.

[49] S. Litster, G. McLean, J. Power Sources 130 (2004) 61.

[50] H.A. Gasteiger, S.S. Kocha, B. Sompalli, F.T. Wagner, Appl. Catal. B: Environmental 56 (2005) 9.

[51] E. Antolini, Appl. Catal. B: Environmental 88 (2009) 1.

[52] Y. Shao, J. Liu, Y. Wang, Y. Lin, J. Mater. Chem. 19 (2009) 46.

[53] A. Yan, X. Xiao, I. Kulaots, B.W. Sheldon, R.H. Hurt, Carbon 44 (2006) 3116.

[54] X. Feng, L. Jiang, Adv. Mater. 18 (2006) 3063.

[55] L. Feng, S. Li, Y. Li, H. Li, L. Zhang*et al.*, Adv. Mater. 14 (2002) 1857.

[56] A. Nakajima, K. Hashimoto, T. Watanabe, Monatshefte Fur Chemie 132 (2001) 31.

[57] X. Zhang, F. Shi, J. Niu, Y. Jiang, Z. Wang, J. Mater. Chem. 18 (2008) 621.

[58] M. Ma, R.M. Hill, Curr. Opin. Colloid Interface Sci. 11 (2006) 193.

[59] X.M. Li, D. Reinhoudt, M. Crego-Calama, Chem. Soc. Reviews 36 (2007) 1350.

[60] R. Blossey, Nat. Mater. 2 (2003) 301.

[61] P. Joseph, C. Cottin-Bizonne, J.M. Benoit, C. Ybert, C. Journet, P. Tabeling, L. Bocquet, Phys. Rev. Lett. 97 (2006).

[62] J. Ou, B. Perot, J.P. Rothstein, Phys. Fluids 16 (2004) 4635.

[63] J. Hyväluoma, J. Harting, Phys. Rev. Lett. 100 (2008).

[64] T. Sun, L. Feng, X. Gao, L. Jiang, Acc. Chem. Res. 38 (2005) 644.

[65] N. Michael, B. Bhushan, Microelectron. Eng. 84 (2007) 382.

[66] I. Morcos, J. Colloid Interface Sci. 34 (1970) 469.

[67] M.E. Schrader, J. Phys. Chem. 79 (1975) 2508.

[68] K. Jian, A. Yan, I. Külaots, G.P. Crawford, R.H. Hurt, Carbon 44 (2006) 2102.

[69] D. Martial, M.P. Rossi, B.M. Kim, G. Korneva, H.H. Bau*et al.*, J. Phys. Chem. B110 (2006) 9850.

[70] W. Xia, C. Jin, S. Kundu, M. Muhler, Carbon 47 (2009) 919.

[71] T.G. Ros, A.J. Van Dillen, J.W. Geus, D.C. Koningsberger, Chem. Eur. J. 8 (2002) 1151.

[72] O. Byl, J. Liu, J.T. Yates Jr, Langmuir 21 (2005) 4200.

[73] W. Brandl, G. Marginean, Thin Solid Films 447-448 (2004) 181.

Chapter 2

The production of a homogeneous and well-attached layer of carbon nanofibers on metal foils

"The problem is not that there are problems. The problem is expecting otherwise and thinking that having problems is a problem" (Theodore Rubin)

Abstract

Carbon nanofibers (CNFs) were deposited on metal foils including nickel (Ni), iron (Fe), cobalt (Co), stainless steel (Fe:Ni 70:11wt%) and mumetal (Ni:Fe 77:14wt%) by the decomposition of C_2H_4 at 600°C. The effect of pretreatment and the addition of H_2 on the rate of carbon formation, as well the morphology and attachment of the resulting carbon layer, were explored. Ni and mumetal show higher carbon deposition rates than the other metals, with stainless steel and Fe the least active. Pretreatment including an oxidation step normally leads to higher deposition rates, especially for Ni and mumetal. Enhanced formation of small Ni particles by in-situ reduction of NiO, compared to formation using Ni carbide, is probably responsible for higher carbon deposition rates after oxidation pretreatment. The addition of H_2 during the CNF growth leads to higher carbon deposition rates, especially for oxidized Ni and mumetal, thus enhancing the effect of the reduction of NiO. The diameters of CNFs grown on metal alloys are generally larger compared to those grown on pure metals. Homogenously deposited and well-attached layers of nanotubes are formed when the carbon deposition rate is as low as 0,1-1mg/(cm^2·h), as mainly occurs on stainless steel.

This chapter is based on the publication: S. Pacheco Benito, L. Lefferts. *Carbon* 2010, 48(10) 2862-72

Chapter 2

2.1 Introduction

Deposition of carbon on catalyst surfaces and reactor walls has historically been detrimental in the industry, since it could cause the deactivation of catalysts, thermal inefficiency and reactor plugging [1-3]. However, since the discovery of carbon nanostructures, new potential industrial applications have emerged. In literature, carbon nanostructures are generally referred to as carbon nanotubes (CNTs) and carbon nanofibers (CNFs) [4]. Carbon nanostructures can be produced by catalytic chemical vapor deposition (C-CVD), arc discharge or laser ablation [5]. C-CVD is widely used in industry and research since it is the most suitable for large-scale production at low cost. In general, the growth of carbon nanostructures requires catalyst nanoparticles (usually Ni, Fe, or Co), a carbon feedstock (hydrocarbon or CO) and high temperatures. The most commonly accepted mechanism for the growth was postulated by Baker *et al.* [6]. According to this mechanism, the hydrocarbon gas first decomposes on the surface of a metal nanoparticle, then carbon diffuses through the particle and finally, it precipitates to form the carbon filament.

Carbon nanostructures offer various advantages such as high surface area, high thermal and electronic conductivity, and high inertness. They are often obtained in powder form by the decomposition of a hydrocarbon on metallic nanoparticles supported on high surface area support material [4, 7]. However, the growth of CNFs on these supports, such as carbon or silica, [8-11] needs the deposition of metal nanoparticles. One of the main advantages of using metallic substrates, such as metal foams [12-14], metal filters [15-18] or metal foils, is that deposition of catalyst particles is not needed to grow CNFs. Moreover, handling carbon in powder form is not as easy and safe as immobilized CNFs, *e.g.* by growing CNF layers on metallic substrates, thus leaving the support material intact. This is especially interesting if CNF layers deposited on metallic substrates are used in applications such as microstructured catalyst supports, polymer reinforcements, sensors and materials for enhanced heat transfer [19-23]. In all these cases, it is desirable to form a homogeneous and well-attached carbon nanostructured layer on the metallic substrates; although it should be noted that most of these applications imply relatively mild shear forces and mechanical stress. In this work,

we will concentrate on the deposition of carbon nanostructures directly onto metal foils.

The deposition of different carbon structures on metal foils by the catalytic decomposition of hydrocarbons at high temperatures (450-850°C) has already been described in literature [24-27]. Over the last decade, Ni, Fe, Co and stainless steel foils have been known for growing carbon nanostructures [28-34]. However, these studies are generally limited to just one type of metal foil, either pure metal or a specific metal alloy. Conditions of CNF growth, as well as the pretreatment of metallic substrates, are known to influence the growth rate and properties of the carbon layer [14]. Furthermore, the addition of H_2 during the catalytic reaction has been reported to influence both the carbon rate and the morphology of the CNFs [35-38]. Efforts have been made to compare the properties of carbon deposited on various metal foils [31, 39-41]. However, these studies do not report on metal alloy foils. Our work aims at providing a systematic study combining the influence of the type of metal (Ni, Fe and Co) and alloy foils (Ni:Fe, 77:14 and 11:70wt%), the pretreatment of the foil and conditions for CNF growth, *e.g.* addition of H_2 during reaction. Furthermore, we will report not only on the rate of carbon deposition, but also on the homogeneity, attachment and morphology of the CNF layers.

2.2 Experimental

2.2.1 Materials

Foils of Ni (787μm thick, 99,5%, Alfa Aesar), Fe (100μm thick, 99,99%, Alfa Aesar), Co (100μm thick, 99,95%, Alfa Aesar), stainless steel type 304 (100μm thick, Fe:Cr:Ni 70:19:11wt%, Alfa Aesar) and mumetal (125μm thick, Ni:Fe:Cu:Mo 77:14:5:4wt%, Alfa Aesar) were used as active catalytic substrates. Round sample pieces of metal foils (10mm in diameter) were prepared from the as-received sheet by wire cut electrical discharge machining (Agiecut Challenge 2). The foils were degreased ultrasonically in acetone and dried at room temperature before being loaded into a quartz tube. Hydrogen and nitrogen (99,999%, Praxair), and ethylene (99,95%, Praxair) were used for CNFs formation without further purification.

2.2.2 Carbon nanostructures formation

An in-house built vertical catalytic chemical vapor deposition (C-CVD) reactor was used to grow carbon nanostructures. It consists of a 45mm outer diameter quartz reactor with a porous quartz plate in the middle to support the metal foils. The temperature was raised in N_2 from room temperature to the desired temperature at a rate of 5°C/min. The samples were first pretreated unless otherwise mentioned. They were either reduced in hydrogen (20% H_2 and balance N_2) under a total flow rate of 100ml/min for 1 hour at 600°C, or oxidized in air (20% air and balance N_2) under a total flow rate of 100ml/min for 1 hour at 700°C, or a combination of both pretreatments. The different pretreatments will be denoted as reduction, no pretreatment (or as-received), oxidation, reduction/oxidation and oxidation/ reduction. N_2 was used to flush the reactor, for safety reasons, when switching between air and hydrogen.

After the pretreatment, ethylene (C_2H_4) was fed into the reactor (20% C_2H_4 and balance N_2) at 600°C for 30 minutes. We used 600°C as a mean value of the temperatures commonly used in literature (400-800°C) for CNF growth on metal foils. The temperature and time of the reaction were kept constant in all experiments. The effect of the addition of hydrogen was studied by adding 10% H_2 (balance N_2) to the gas stream, keeping the concentration of ethylene and the total flow rate constant. Finally, ethylene and hydrogen (if used), gas streams were shut off and the system was cooled down to room temperature under 100ml/min of N_2 at a rate of 10°C/min. A series of samples were cooled down immediately after the pretreatment, to calculate the weight before carbon deposition, without being further used. Carbon is assumed to be deposited similarly on both sides of the metal foils.

2.2.3 Characterization

The averaged reaction rates, in mg/(cm^2·h), were calculated from the difference in weight after the pretreatment and after the catalytic reaction, including the weight of any loose carbon, and from the total surface area of flat metal foils, including the edges. The weights were measured in a Metler Toledo AE163 balance with precision up to 0,01mg. The attachment of the carbon layer was assessed by the difference in weight between the sample after synthesis,

including loose carbon, and after shaking it vigorously using tweezers for 30 seconds. The weight loss percentage is calculated accounting for the total weight of carbon deposited. The morphology of the metal substrates and the carbon nanostructures was studied using scanning electron microscope LEO 1550 FEG, equipped with an in-lens and a secondary electrons detector. Poorly attached carbon was removed before examining the surface morphology. The average diameter of CNFs was calculated measuring 30 nanofibers per sample.

2.3 Results and discussion

2.3.1 Influence of metal composition, pretreatment and hydrogen addition

Figures 2.1a and 2.1b (note the different scales) show that the amount of carbon deposition follows a general trend regarding the type of catalyst, independent of the pretreatment and addition of H_2: Fe ~ stainless steel < Co < Ni < mumetal. A similar trend has been reported for the decomposition of C_2H_2/H_2 at similar temperatures as in this study [42]; it is claimed that the deposition is slow on Fe, moderate on Co and fast on Ni. However, Sacco *et al.* [39] observed an opposite trend for the decomposition of gas mixtures containing CH_4-CO-H_2 on Fe, Co and Ni foils at similar temperatures and longer reaction times (3-8 hours as compared to 30 minutes in this study). We believe it is not possible to make a direct comparison because of the different gas mixtures. Moreover, it was reported that CO, which was not used in our study, is mainly responsible for carbon deposition on Fe and Co foils. In addition to this, we observe that the activity of stainless steel is comparable to Fe and that mumetal outperforms Ni.

Without adding H_2, stainless steel is more active than Fe, which hardly grows any carbon (**figure 2.1a**). However, when H_2 is added, Fe grows more carbon than stainless steel after reduction, oxidation and reduction/oxidation pretreatments (**figure 2.1b**). Following the general trend describe before, Ni is more active than the other metals (except mumetal) when the pretreatment includes an oxidation step, and especially in combination with the addition of H_2 (**figure 2.1b**). The highest rate for Ni, 46mg/(cm^2·h), is obtained after reduction/oxidation (**figure 2.1b**) resulting in a detached carbon carpet, which will be described later. As an exception to the general trend, Co is somewhat more active than Ni after reduction or without any pretreatment (**figure 2.1a**). Mumetal

is significantly more active than all the other metals, for all combinations of pretreatments and addition of hydrogen (**figures 2.1a and 2.1b**). Both mumetal and Ni are especially active when the pretreatment includes an oxidation step (**figure 2.1a**), and especially in combination with the addition of H_2. The maximum rate achieved by mumetal was 136mg/(cm^2·h).

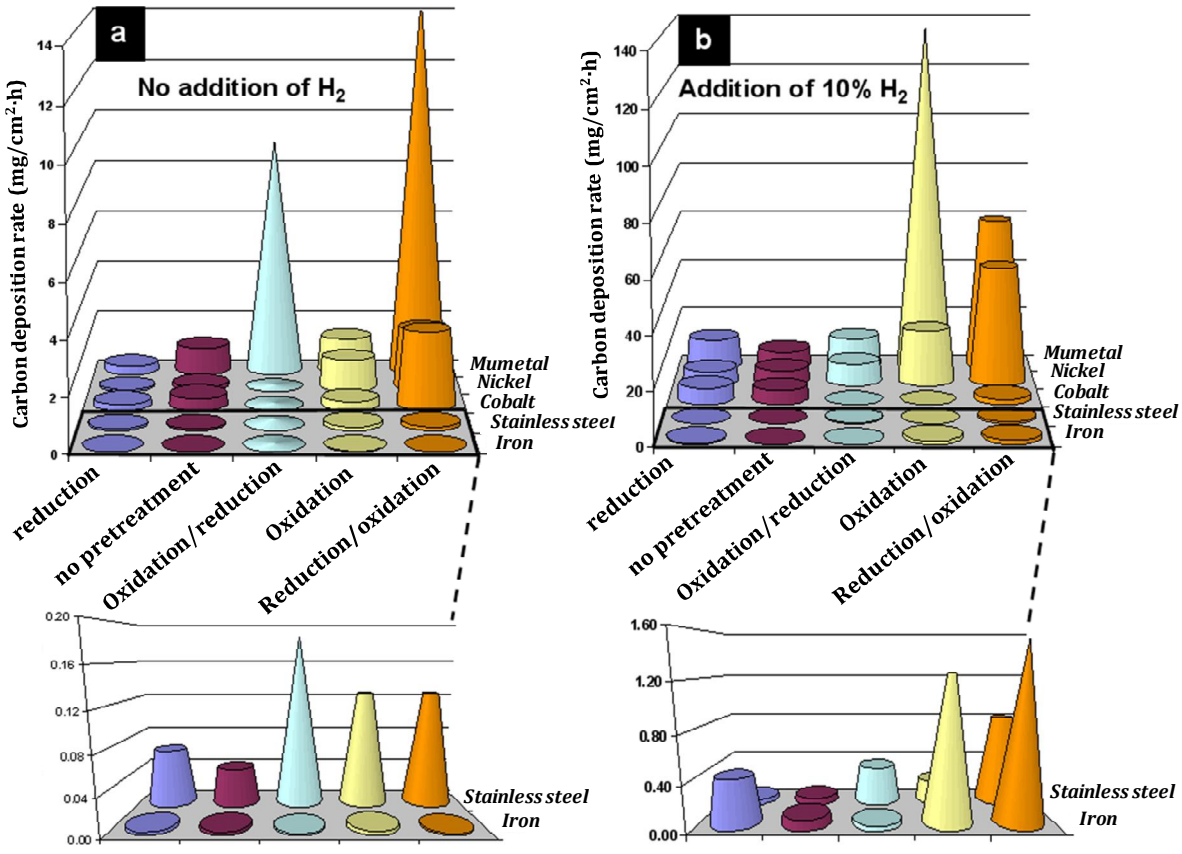

Figure 2.1: *average carbon deposition rates for different metal foils and different pretreatments after reaction with C_2H_4 at 600°C. a) Without addition of H_2 during the reaction. b) 10% H_2 is added to the reaction stream*

The pretreatment of the metals increases the carbon deposition rate following this general trend: reduction < no pretreatment < oxidation/reduction < oxidation < reduction/oxidation (**figures 2.1a and 2.1b**). We observe that the pretreatment containing an oxidation step generally leads to more carbon deposition (**figure 2.1a**), especially when H_2 is added (except Co) (**figure 2.1b**). Our observations agree with Geurts *et al.* [43] and Randall *et al.* [15] regarding the

increase of carbon deposition rate after pre-oxidation of metal alloys. Moreover, as-received samples grow at least similar amounts of carbon as compared to reduced or oxidized/reduced samples (**figures 2.1a and 2.1b**). This agrees with results of Lobo *et al.* [24], who reported higher carbon deposition rates on as-received Ni foils as compared to reduced samples. We believe this is caused by the presence of an oxide layer on the as-received metal foils, as will be explained in more detail later. Exceptionally, mumetal shows less carbon growth after oxidation as compared to oxidization/reduction (**figure 2.1a**); however, if H_2 is added, oxidation pretreatment leads to more carbon growth than reduction/oxidation pretreatment (**figure 2.1b**). Oxidized stainless steel also shows less carbon growth than oxidized/reduced sample if H_2 is added (**figure 2.1b**), in agreement with the observations of Martínez-Hansen *et al.* on stainless steel meshes [38]. The authors used similar pretreatments as in this study except reduction/oxidation, which leads to the highest rate according to our observations. Co deviates from the general trend when (i) H_2 is added during the reaction and (ii) the pretreatment includes an oxidation step (**figure 2.1b**). In this case, a lower amount of carbon is formed in comparison to reduced and as-received Co. Reduced Fe also deviates from the trend when H_2 is added, leading to more carbon deposition than as-received and oxidized/reduced samples (**figure 2.1b**).

Generally speaking, we observe that the addition of H_2 increases the amount of carbon deposition for all combinations of metals and pretreatments (**figures 2.1a and 2.1b**). These results agree with literature regarding the decomposition of hydrocarbons on different metal foil surfaces [1, 24-26, 40, 42, 44-45]. In the absence of H_2, carbon formation ceases because of deactivation of the catalyst by carbon encapsulation; H_2 appears to gasify encapsulating carbon [1, 26, 46-48]. Park *et al.* [44] found that at a ratio H_2/C_2H_2 3:1, the growth of CNTs on stainless steel foils type 304 (the same as in this work) also ceased within a few minutes, in contrast to sustained growth when a 30:1 H_2/C_2H_2 ratio is used. In our study, deactivation probably also happens, unfortunately we cannot observe that. We have used a H_2/C_2H_4 ratio of 1:2 and we observe that stainless steel produces nanofibers in most cases, as will be discussed in detail later. A higher amount of H_2 is probably needed to prevent encapsulation with carbon when C_2H_2 is used, because it is more reactive than C_2H_4. On the contrary, Jackson *et al.* [49] observed

the presence of CNFs on stainless steel foils exclusively at ratios H_2/C_3H_6 greater than 20:1. We observe that the enhancement effect of H_2 strongly depends on the type of pretreatment. The largest enhancement is observed on Ni and mumetal after oxidation, resulting in an increase of 3-6 times in activity (**figures 2.1a and 2.1b**). Our observations on as-received and reduced samples agree with Bernardo *et al.* [42] who reported that the effect of H_2 is more important for Co than Fe when decomposing C_2H_2 at 400-625°C. However, after reduction/oxidation and oxidation pretreatment the addition of H_2 increases the carbon growth on Fe, but decreases the carbon growth on Co.

2.3.2 Attachment of the carbon layers

The attachment has been divided in 3 different groups. Samples with a weight loss <3% are considered to have good attachment. If the weight loss is between 3-20%, the attachment is considered moderate. If the weight loss is >20%, the attachment is considered to be poor. **Table 2.1** shows that Fe and stainless steel have the best attached carbon layers for all the combinations of pretreatments and addition of H_2. However, as shown in **figures 2.1a and 2.1b**, the amount of carbon deposited is quite low in all cases. CNTs grown on stainless steel, at 770°C and in presence of H_2, were also reported to be well anchored to the substrate [30].

Table 2.1: *attachment of carbon to various metal foils with different pretreatments, and post reaction with C_2H_4 at 600°C with/without addition of 10% H_2*

	Reduction	No pretreat.	Oxidation/ Reduction	Oxidation	Reduction/ Oxidation	Reduction + H_2	No pretreat. + H_2	Oxidation/ Reduction + H_2	Oxidation + H_2	Reduction/ Oxidation + H_2
Mumetal	±			+	-		±	-		
Nickel	+				±			-		
Cobalt	+				±			+		
Stainless steel	+									
Iron	+									

+ : good attachment; ± : moderate attachment; - : poor attachment

Without adding H_2, the attachment of carbon to Co is good independent of the pretreatment, except for the reduction/oxidation pretreatment (**table 2.1**). If H_2 is added, the pretreatments including an oxidation step lead to good attachment. However, the as-received and reduced samples result in moderate attachment, which is in agreement with the observations of Sacco *et al.* [39], who used gas mixtures containing CH_4/H_2 on Co foils at 623°C after reduction in H_2.

The attachment of the deposited carbon on Ni is good if H_2 is not added, except in the case of reduction/oxidation pretreatment (**table 2.1**). However, the attachment becomes poorer if H_2 is added to the reaction mixture (**table 2.1**). This is in agreement with the observation of loose carbon on as-received Ni foils when decomposing C_2H_2/H_2 [24], and on reduced Ni foils when decomposing mixtures of gases containing CH_4/H_2 [39]. Moreover, we observed by eye that the combination of oxidation pretreatment with addition of H_2 leads to the formation of mountains of loose carbon (as high as 2 mm), similar to observations by Lobo *et al.* [24], or a carpet of carbon that easily detaches.

Mumetal shows well-attached carbon deposition only if the sample is oxidized and H_2 is not added (**table 2.1**). For the remaining combinations of pretreatment and addition of H_2, the attachment is either moderate (mainly without adding H_2), or bad (**table 2.1**). This is in agreement with Nishiyama *et al.* [50], who observed carbon detached from a Ni:Cu 98:2wt% alloy foil, as compared to 5wt% Cu in mumetal. Besides, similar to the results with Ni, the combination of addition of H_2 and pretreatments including oxidation leads to the formation of mountains of loose carbon visible by eye (as high as 5 mm).

2.3.3 Homogeneity and morphology of the carbon layers

We observe that the morphology of the carbon layers deposited on the metal foils can be divided in four typical types according to the presence and homogeneity of CNFs (**figure 2.2**). We would like to remind the reader that the samples are analyzed after removing any loose carbon. The first group includes all samples with homogeneous deposition of CNFs all over the surface, as presented in **figure 2.2a**. The second group includes the samples with inhomogeneous coverage of CNFs on the surface (**figure 2.2b**). Samples with small amount of scattered CNFs

are included in the third group (**figure 2.2c**). The group 4 includes those samples with no clear CNF deposition, instead formation of granule shaped deposits is observed (**figure 2.2d**).

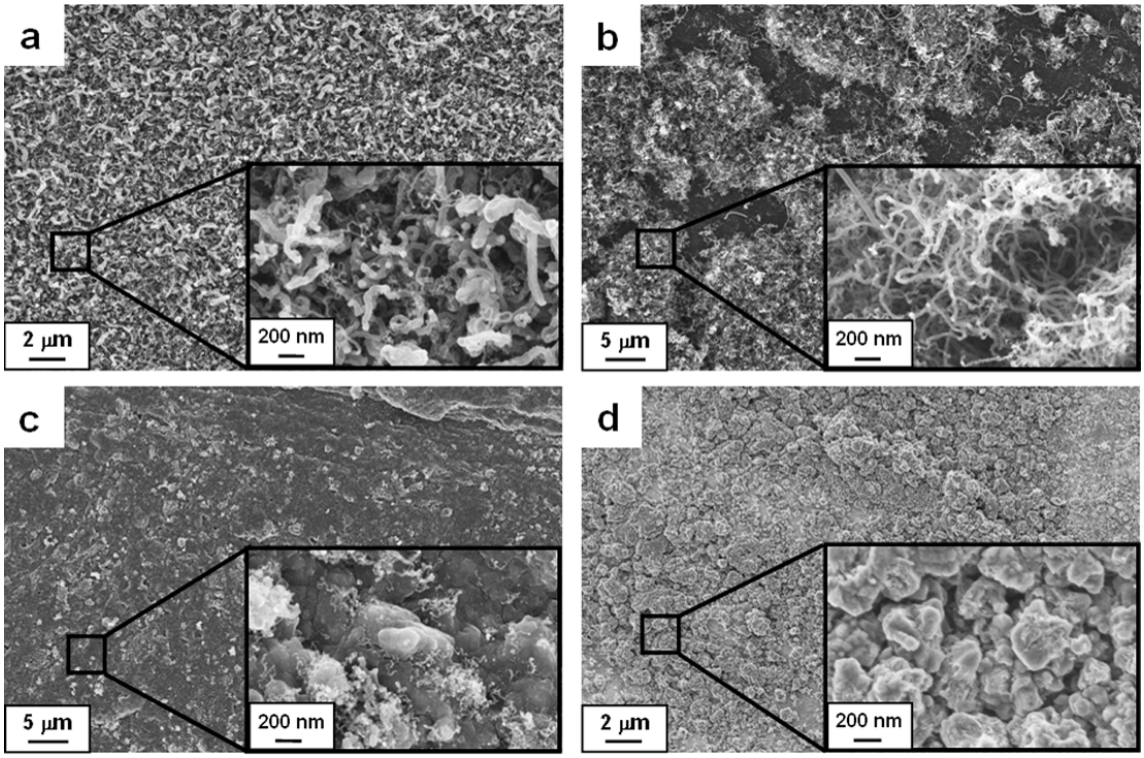

Figure 2.2: *types of morphology of the carbon layer deposited on different metal foils at two different magnifications. a) Homogeneous deposition of CNFs on stainless steel foil after oxidation/reduction and without adding H_2 during reaction. b) Non-homogeneous deposition of CNFs on mumetal foil after reduction and after addition of 10% H_2 during reaction. c) Scattered CNFs on Ni foil after oxidation and without adding H_2 during reaction. d) No deposition of CNFs on Ni foil without pretreatment and without adding H_2 during reaction.*

Figure 2.3 shows that, generally speaking, CNFs grow more homogeneously on stainless steel as compared to the other metals. Without adding H_2, as-received and reduced stainless steel samples are not able to grow CNFs (**figure 2.3a**). However, if H_2 is added, the density increases although the nanofibers are not uniformly distributed (**figure 2.3b**). If the sample is oxidized before the deposition, just a few CNFs are observed (**figure 2.3a**); in contrast, if H_2 is added, CNFs are more homogeneously distributed (**figure 2.3b**). If a

combination of pretreatments is used, the homogeneity of the fibers is good, independent of the addition of H_2 (**figures 2.3a and 2.3b**). In literature, homogeneous distribution of carbon nanostructures using other pretreatments and reaction conditions has also been reported. Baddour *et al.* [34] obtained different CNT coverage on stainless steel plates by varying the etching time of pretreatment with HCl. The authors used C_2H_2 without adding H_2 and higher temperatures, 650-850°C, as compared to 600°C and C_2H_4 used in this study. Unfortunately, no observations on the attachment of the carbon layer have been reported. Martínez-Hansen *et al.* [38] also reported the need of HCl pretreatment in combination with oxidation/reduction on stainless steel mesh to obtain a homogeneous layer of CNTs. On the contrary, we are able to prepare a homogenous layer of CNFs on stainless steel without acid pretreatment; a lower synthesis temperature (600°C), in comparison with their work (700-900°C), might be responsible of this difference.

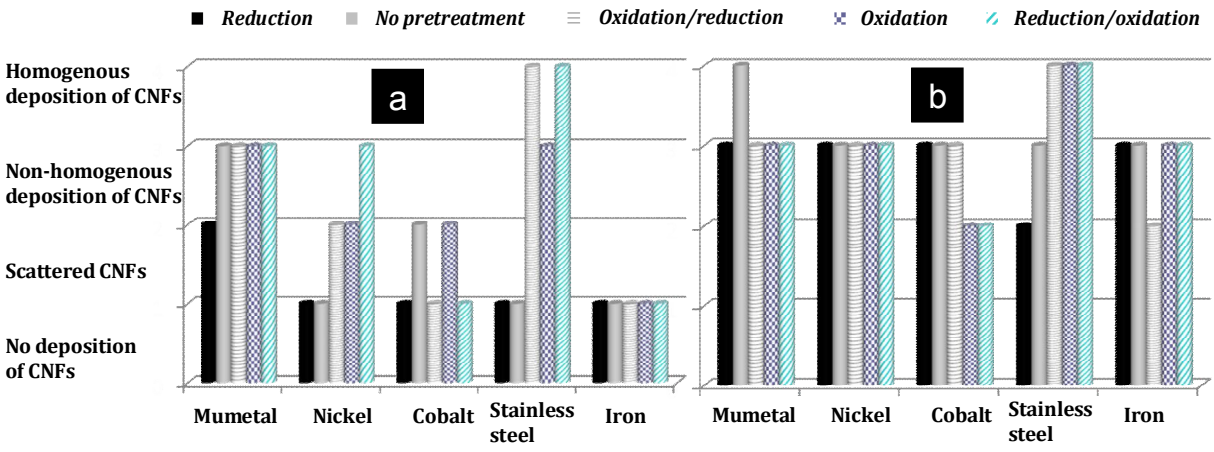

Figure 2.3: *homogeneity of the CNF layers on the different metal foils with different pretreatments after reaction with C_2H_4 at 600°C. a) Without addition of H_2 during the reaction. b) With addition of 10% H_2 during the reaction*

Mumetal is the only metal that, in terms of homogeneity, shows CNFs independent of the kind of pretreatment used or the addition of H_2 (**figures 2.3a and 2.3b**). If the sample is reduced and no H_2 is added, scattered CNFs are formed (**figure 2.3a**). Generally, the uniformity of CNFs along the surface is quite high, as was reported for CNTs grown on a similar alloy containing less Ni and Fe, and

more Cu (63%Ni, 2,5%Fe, 28-34%Cu) [31], as compared to mumetal (77%Ni, 14%Fe, 5%Cu, 4%Mo). However, most of the samples show regions of inhomogeneity, which is probably due to the removal of loose nanofibers (**figures 2.3a and 2.3b**). Exceptionally, the combination of the as-received sample and addition of H_2 results in the formation of better homogeneously distributed CNFs (**figure 2.3b**).

Ni samples form granules (**figure 2.2d**), rather than fibers, if the samples are reduced (50-200nm granules) or not pretreated (300-500nm granules) (**figure 2.3a**). The foil is able to grow CNFs in a scattered mode, not uniformly distributed, when the pretreatment contains an oxidation step (**figure 2.3a**). Sacco *et al.* [39] reported the presence of a thin carbon over-layer on Ni foils within which Ni fragments and scattered carbon filaments were embedded. If H_2 is added, the density of fibers increases in all cases, but still the CNFs are not evenly distributed on the surface (**figure 2.3b**). Our observations agree with Du *et al.* who found scattered CNTs on reduced Ni grids [29], despite some differences in the reaction conditions such as shorter reaction times, 2-15 minutes, and higher temperatures, 650-850°C, as compared to 30 minutes at 600°C used in this study.

Co foil does not show nanofibers in case of reduction or oxidation/reduction pretreatment (**figure 2.3a**); in those cases, granules of about 200-500nm are formed. As-received and oxidized Co produce scattered CNFs and granules of about 100-300nm (**figure 2.3a**). When H_2 is added, more CNFs grow, but they are still not uniformly distributed (**figure 2.3b**). The combination of an oxidative pretreatment and addition of H_2 results in the growth of only few CNFs (**figure 2.3b**).

Fe is the least active metal in this study for deposition of CNFs. If the amount of deposited carbon is very low, the color of the surface remains metallic gray; increasing density of CNFs would turn the color to black. Without addition of H_2 during the reaction, grains or flakes of different sizes (100-500nm approximately) are observed, independent of the pretreatment (**figure 2.3a**). The addition of H_2 helps to deposit either scattered CNFs or a combination of granules and CNFs (**figure 2.3b**).

2.3.4 Size of the carbon nanostructures

Figure 2.4 shows the average diameters of CNFs for all samples containing fibers, as well as the width of diameters distribution, deducted from the standard deviation. The largest diameters, as well as the diameter distribution, are observed on the metal alloys, stainless steel and mumetal. **Figure 2.5a** shows a typical SEM image for both alloys in which nanofibers with diameters larger than 100nm are observed, along with nanofibers thinner than 50nm. Varanasi *et al.* [33] also observed a wide range of CNTs diameters, 20-100nm, grown on other Ni/Cu substrate (Cu:Ni:Mn 55:44:1wt%). Moreover, our results agree with observations of Tribolet *et al.* [16] who observed thicker CNFs on stainless steel, as compared to Ni, grown on metallic filters from C_2H_6/H_2 at 620-680°C after oxidation/reduction pretreatment. Abad *et al.* [51] also found thicker nanostructures grown from stainless steel when compared to the same sample coated with Co nanoparticles; however, it must be mentioned that the authors used plasma enhanced CVD at 650°C and NH_3 pretreatment. Stainless steel presents the largest CNF diameters after reduction/oxidation pretreatment if H_2 is not added (**figure 2.4a**), and after oxidation pretreatment if H_2 is added (**figure 2.4b**).

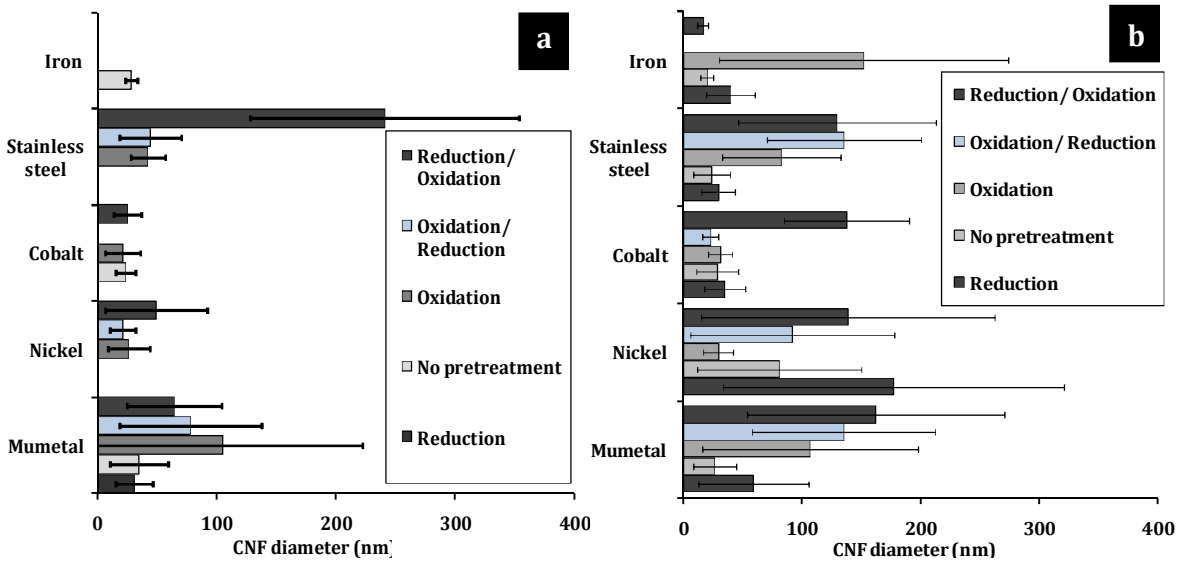

Figure 2.4: *average diameters and standard deviation of carbon nanofibers deposited on metal foils with different pretreatments after reaction with C_2H_4 at 600°C. a) Without addition of H_2 during the reaction; b) with addition of 10% H_2 during the reaction*

CNFs grown from mumetal are, as observed on stainless steel, thicker when the pretreatment contains an oxidation step (**figure 2.4a**); this effect is enhanced even more if H_2 is added (**figure 2.4b**). The average CNF diameter grown from Ni is smaller than 50nm in absence of H_2 (**figure 2.4a**); however, thicker fibers are observed when H_2 is added (**figure 2.4b**). In addition, reduced Ni samples result in a much broader distribution. **Figure 2.5b** shows a typical SEM image of CNFs deposited on Ni with diameters ranging from 10 and 100nm. Co is the metal that grows CNFs with most uniform diameters independent of pretreatment and addition of H_2 (**figures 2.4a and 4b**). The diameters of the few nanofibers grown on Fe, if any, are below 50nm (**figure 2.4a**). Fe forms fibers as thick as 150nm only after oxidation pretreatment and addition of H_2 (**figure 2.4b**). **Figure 2.5c** illustrates a typical SEM image of thinner CNFs grown on Co and Fe, as compared to the other metals (**figure 2.5c**).

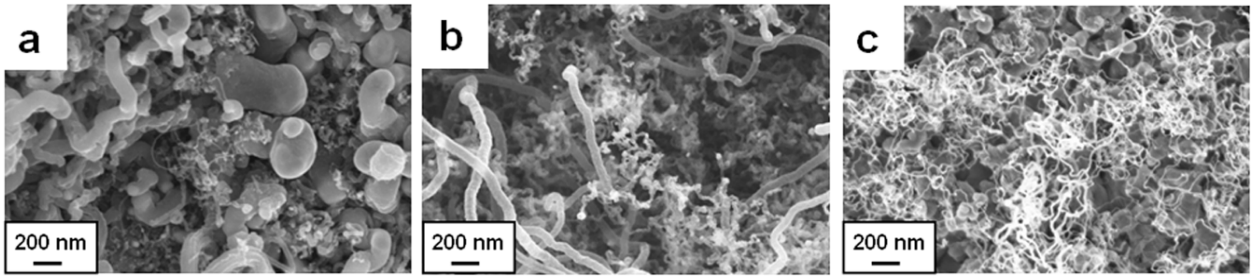

Figure 2.5: *typical pictures of the size of the nanofibers produced after reaction with C_2H_4 at 600°C on various metal foils. a) Oxidized mumetal, no addition of H_2 during reaction; b) reduced nickel, addition of 10% H_2 during reaction; c) oxidized/reduced cobalt, addition of 10% H_2 during reaction.*

Mumetal is able to grow CNFs in a spider-like manner (**figure 2.6a**). All fibers contain metal particles in the tip, as can be seen in the right panel by using the secondary electron detector, highlighting the metal particles. Tip growth has also been observed on other Ni/Cu substrates (Cu:Ni:Mn 55:44:1wt%) [33]. The growth mechanism of carbon on mumetal is apparently different as compared to octopus type of growth (similar ensembles of several CNFs emanating from one metal particle, but now without metal particles at the tip) as observed on Ni/Cu alloys [46, 52-53]. However, sometimes the metal nanoparticles are located in the middle of the fiber (**figure 2.6b**). CNFs grown from Ni also have metal

nanoparticles mainly located in the tip of the fibers, similar to the Ni based alloy, namely mumetal (**figure 2.6c**). For Co we also observe metal nanoparticles in the tip of the nanofibers as well as CNFs with rough surface, maybe because of surface defects (**figure 2.6d**). **Figure 2.6e** shows the different fiber morphologies growing from stainless steel such as straight, curly [44] and twisted nanofibers. In **figure 2.6f** we observe metal nanoparticles in the tip of CNFs on stainless steel by using the secondary electron detector, indicating a tip-growth mechanism. It is interesting to note that also different fibers grow from one metal nanoparticle and these fibers seem to have a quite rough surface.

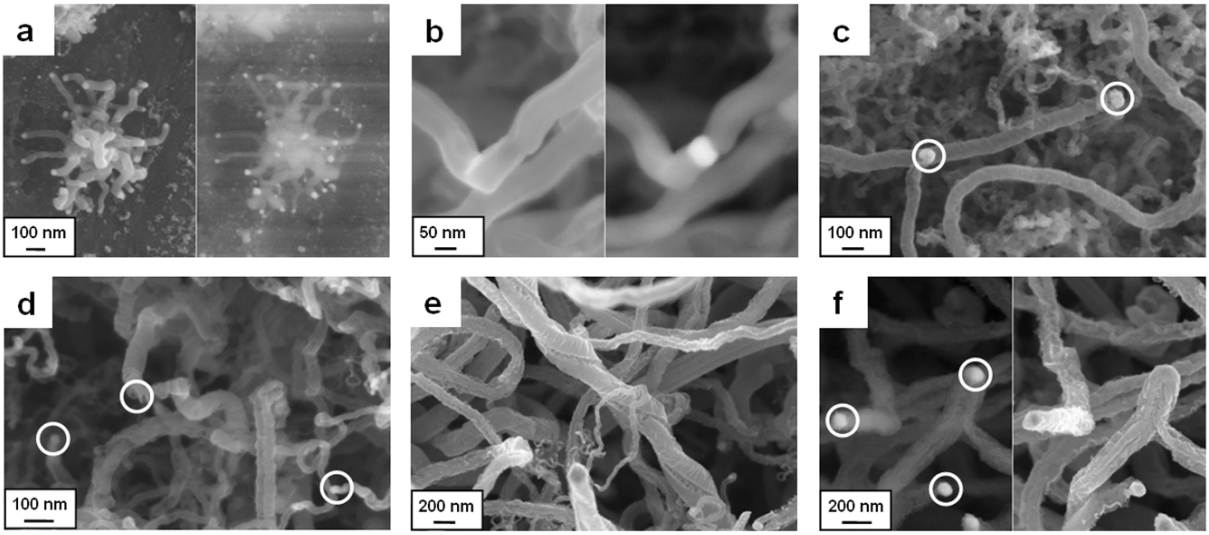

Figure 2.6: *morphology of carbon nanofibers produced after reaction with C_2H_4 at 600°C on various metal foils. a) As-received mumetal, no addition of H_2 during reaction; b) oxidized/reduced mumetal, addition of 10% H_2 during reaction; c) reduced Ni, addition of 10% H_2 during reaction; d) reduced Co, addition of 10% H_2 during reaction; e) f) reduced/oxidized stainless steel, addition of 10% H_2 during reaction*

2.4 General discussion

Our observations clearly show that the pretreatment strongly influences the rate of carbon deposition on all metal foils. **Table 2.2** shows the ratio of the averaged carbon deposition rates after oxidation and after reduction pretreatment. If H_2 is not added, oxidized mumetal and especially Ni present a higher rate than reduced samples (**table 2.2**). However, the increase of the rate is not so large for the rest of the metals. If H_2 is added, the enhancement of the rate because of

oxidation is larger for mumetal than for Ni (**table 2.2**). On the other hand, Fe hardly changes, the ratio of the averaged carbon rates decreases for Co and stainless steel shows a remarkable increase (**table 2.2**).

Table 2.2: *ratio of average carbon deposition rates on different metal foils after oxidation and reduction pretreatments*

	Rate after oxidation /rate after reduction	
	Without adding H_2	**Adding 10% H_2**
Mumetal	**4,7**	**11,4**
Nickel	**15,4**	**3,7**
Cobalt	**1,4**	**0,0**
Stainless steel	**1,8**	**17,0**
Iron	**1,0**	**1,2**

Earlier it was described how small Ni particles, needed to grow CNFs, are formed on Ni foam during decomposition of C_2H_4 [14]. It was proposed that the presence of NiO (created during pre-oxidation) increases the rate of CNF formation because of direct formation of nanoparticles by *in-situ* NiO reduction. This occurs as opposed to the slow formation of Ni nanoparticles on polycrystalline metallic Ni by the decomposition of meta-stable Ni_3C (from pre-reduced sample). The average rates contain information about the rate of nanoparticles formation (initiation), the rate of deactivation by encapsulation and the rate of CNF formation for individual nanoparticles. We observed that the initiation rate is an important factor for the growth of CNFs on Ni foam at 450°C [14] (600°C in this study). For the reduced sample it took about 30 minutes to start significant carbon growth, whereas initiation occurred within 5 minutes on the oxidized sample. We therefore speculate that the initiation rate determines to a significant extent the rate of CNF growth on Ni and Ni rich alloy foils. The presence of small amounts of Cu in mumetal (5wt%) might be responsible for the significant increase in the carbon deposition rate, as has been suggested in literature for Ni-Cu and Fe-Cu alloys [1, 45, 47, 50, 54-55]. Moreover, Cu has been reported to facilitate the reduction of NiO and therefore the formation of Ni nanoparticles is influenced, possibly increasing the carbon deposition rate [47, 56].

Without adding H_2, CNF growth on stainless steel is hardly enhanced by pre-oxidation (**table 2.2**), despite the fact that stainless steel contains 11wt% Ni. Apparently, the oxide layer on stainless steel contains rather Fe and chromium oxides instead of Ni oxides. The effect of chromium (19wt% in stainless steel) in decreasing the carbon deposition rates was already suggested by others [32, 49, 57-58]. We speculate that oxidation pretreatment influences the composition of the oxide layer, thus increasing Ni and Fe oxides. Therefore, the addition of H_2 might reduce Fe and Ni from the oxides formed during oxidation pretreatment, leading to an increase of the carbon deposition rate (**table 2.2**). We also observe that Fe and Co show similar carbon deposition rates after both oxidation and reduction pretreatment, independent of the addition of H_2 (**table 2.2**). This might due to difficult formation of small metal nanoparticles suitable to grow CNFs from the chemically stable Fe and Co oxides [41], as compared to NiO. It is known that FeO is more active than Fe and Fe_2O_3 for CNF formation [59]. The fact that we observe hardly any enhancement of CNF formation when oxidizing Fe indicates that the oxide layer contains mainly F_2O_3.

We observe clear differences in the carbon deposition rates when comparing samples oxidized before the reaction, namely as-received, oxidized and reduced/oxidized samples (**figure 2.1**). We also observe differences, in a minor extent, when comparing samples reduced before the reaction, namely reduced and oxidized/reduced samples (**figure 2.1**). Therefore, these differences might be due to differences in the morphology of the samples; *e.g.* grain sizes. Our group previously observed [14] that the grain sizes in Ni foam varies with the pretreatment and the grain sizes decrease in the order: reduction > oxidation/reduction. The rate of CNF formation increases in the same order, in agreement with our observations. Park *et al.* [60] also found a correlation between the grain size, modified by hydrogen plasma pretreatment, and the amount of CNTs grown on stainless steel: the larger the grain size, the poorer the CNT growth. It is described in literature that the presence of surface defects and grain boundaries on metallic materials increases the rate of carbon deposition on the surface by the decomposition of a hydrocarbon [14, 28, 34, 61].

Figures 2.7a and 2.7b show the variation of both homogeneity and attachment of CNF layers with carbon deposition rate. The rates of the reactions are changed by the combinations of various pretreatments and addition of H_2 (logarithmic scale). Besides, it should be noted that the data on the rates includes well and poorly attached carbon; however, the homogeneity was judged only for well-attached carbon layers. **Figure 2.7a** shows that the attachment of carbon to metal foils becomes poor as the carbon deposition rate increases. The attachment is good if the rate is lower than 0,3mg/(cm^2·h). It is either good or moderate if the rate is in the range 0,3-9mg/(cm^2·h). Finally, attachment becomes poor if the rates are higher than 9mg/(cm^2·h). Ni and mumetal are the only metals that grow poorly attached CNFs. Moreover, the attachment of carbon on Fe and stainless steel is good, independent of the carbon deposition rate.

In **figure 2.7b** we observe that the homogeneity of CNFs mostly increases with the carbon deposition rate. Just few or even no CNFs are observed in the case of rates lower than 0,07mg/(cm^2·h). In the range from 0,07-2mg/(cm^2·h), homogeneity increases in the order: Ni ~ Co < Fe ~ mumetal< stainless steel. At rates higher than 2mg/(cm^2·h), Ni, Co and mumetal still present inhomogeneous distribution of CNFs. As an exception, mumetal shows homogeneous distribution of CNFs only at a rate of approximately 7mg/(cm^2·h). From **figures 2.7a and 2.7b** we conclude that stainless steel is the only metal that combines well-attached CNFs with a homogeneous distribution, specifically at rates higher than 0,1mg/(cm^2·h). Ni and mumetal are able to grow a high amount of CNFs, but they are in many cases poorly attached. The homogeneity of CNFs on Fe and Co increases with the carbon deposition rate, although not reaching a complete coverage of well-attached CNFs.

Chinthaginjala *et al.* [37, 62] reported on the formation of a microporous carbon layer between the Ni support and the CNF layer grown by the decomposition of C_2H_4 on Ni foam. We claimed an important role of this microporous layer to induce good attachment to the Ni foam, observing that the addition of H_2 decreases its thickness and, therefore, the attachment to the substrate. We speculate this argument could be valid for the other metals foils, apart from Ni, since it is known that Fe and Co foils are also initially covered with a

carbon over-layer [41]. Depending on the growth temperature and the kind of material, the existence of other carbon structures, apart from CNFs, might represent an important fraction of the total carbon deposition. Our study has been carried out at only one temperature, 600°C, for all the different metals and we have referred generally to carbon deposition rates instead of CNFs deposition rates. In comparison with Ni foam, we believe that the moderate and bad attachment observed on Ni foils in our study might be due to the use of both higher temperatures (600°C as compared to 440-450°C for nickel foam) and H_2 addition.

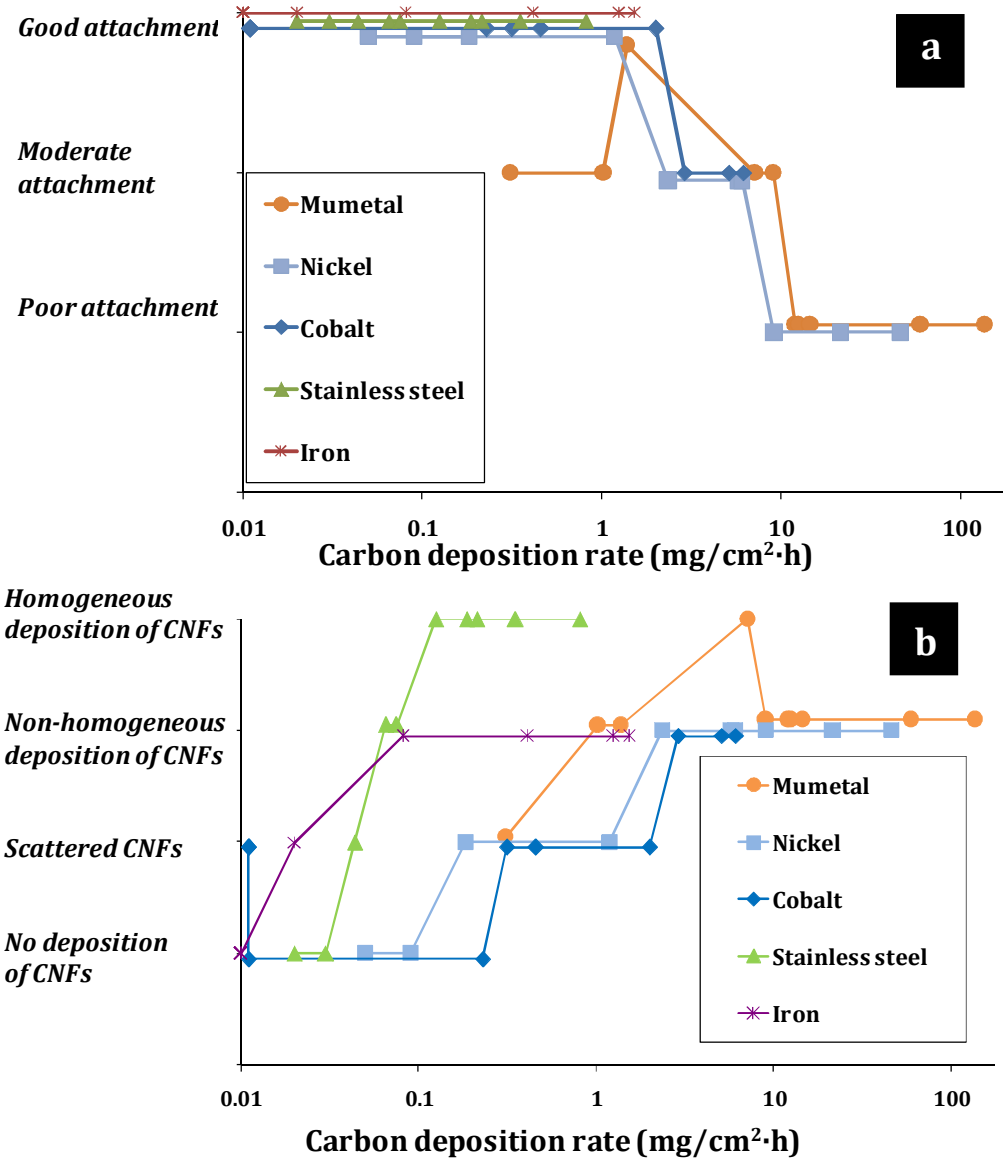

Figure 2.7: *level of attachment (a) and homogeneity (b) of CNF layers deposited on different metal foils as a function of the average carbon deposition rate after reaction with C_2H_4 at 600°C*

2.5 Conclusions

By tuning the type of metal catalyst, pretreatment conditions and the addition of H_2 in the gas mixture, the rates of carbon deposition on metal foils by the decomposition of C_2H_4 at 600°C vary. Ni is especially active for the formation of CNFs after oxidation pretreatment, particularly when H_2 is added to the stream. Mumetal shows the highest carbon growth rate for all combinations of pretreatments and addition of H_2. It is extremely active after reduction/oxidation pretreatment and especially after oxidation. The presence of oxidized Ni and Cu in mumetal, in combination with the addition of H_2, is responsible for the high rates on mumetal. On the contrary, metal oxides present in Co, Fe and stainless steel foils do not lead to high carbon deposition rates. This indicates that metal nanoparticles growing CNFs are easily formed from NiO, in contrast to Fe and Co oxides. Generally speaking, the diameters of CNFs deposited on metal alloys, namely mumetal and stainless steel, are thicker than pure metals. Co and Fe generally grow thinner CNFs.

Carbon deposition rates influence the homogeneity and attachment of CNF layers. High activity towards CNFs formation is generally detrimental for obtaining well attached CNF layers, as mainly occurs with Ni and mumetal. They either grow scattered CNFs, or many CNFs not well attached to the surface. Co and Fe averagely present good attached CNFs, but not homogenously distributed. Stainless steel is the most versatile metal foil; it is possible to achieve homogeneous and well attached CNFs at relatively low carbon growth rates, *i.e.* 0,1-1 mg/(cm^2·h).

Acknowledgements

The authors greatly acknowledge Dr. A. van Houselt for valuable scientific discussions.

References

[1] A.I. La Cava, C.A. Bernardo, D.L. Trimm, Carbon 20 (1982) 219.

[2] J.L. Figueiredo, Materials and Corrosion - Werkstoffe und Korrosion 49 (1998) 373.

[3] P.G. Menon, J. Mol. Catal. 59 (1990) 207.

[4] K.B.K. Teo, C. Singh, M. Chhowalla, W.I. Milne, in: H.S. Nalwa, (Eds.) Encyclopedia of Nanoscience and Nanotechnology, vol 10 (2003) 1.

[5] T.W. Ebbesen, Carbon Nanotubes: Preparation And Properties. CRC Press, Boca Raton, Florida, 1997.

[6] R.T.K. Baker, M.A. Barber, P.S. Harris, F.S. Feates, R.J. Waite, J. Catal. 26 (1972) 51.

[7] K.P. De Jong, J.W. Geus, Catal. Rev. Sci. Eng. 42 (2000) 481.

[8] M.J. Ledoux, C. Pham-Huu, Catal. Today 102-103 (2005) 2.

[9] W.Z. Li, D.Z. Wang, S.X. Yang, J.G. Wen, Z.F. Ren, Chem. Phys. Lett. 335 (2001) 141.

[10] S.S. Tzeng, K.H. Hung, T.H. Ko, Carbon 44 (2006) 859.

[11] D.B. Thakur, R.M. Tiggelaar, J.G.E. Gardeniers, L. Lefferts, K. Seshan, Surf. Coat. Technol. 203 (2009) 3435.

[12] W. Huang, X.B. Zhang, J. Tu, F. Kong, Y. Ning*et al.*, Phys. Chem. Chem. Phys. 4 (2002) 5325.

[13] N.A. Jarrah, F. Li, J.G. Van Ommen, L. Lefferts, J. Mater. Chem. 15 (2005) 1946.

[14] N.A. Jarrah, J.G. van Ommen, L. Lefferts, J. Catal. 239 (2006) 460.

[15] L. Randall, R.L. Vander Wal, L.J. Hall, Carbon 41 (2003) 659.

[16] P. Tribolet, L. Kiwi-Minsker, Catal. Today 102 (2005) 15.

[17] S.J. Park, D.G. Lee, Carbon 44 (2006) 1930.

[18] F. Xu, X. Liu, S.D. Tse, Carbon 44 (2006) 570.

[19] N.M. de Almeida Coelho, J.L.B. Furtado, C. Pham-Huu, R. Vieira, Mater. Res. 11 (2008) 353.

[20] C. Pham-Huu, M.J. Ledoux, Top. Catal. 40 (2006) 49.

[21] R.L. Vander Wal, L.J. Hall, Adv. Eng. Mater. 6 (2004) 48.

[22] Y. Yun, R. Gollapudil, V. Shanov, M.J. Schulz, Z. Dong, *et al.*, Nanosci. Nanotechnol. 7 (2007) 891.

[23] C.R. Dietz, Y.K. Joshi, Nanosca. Microsca. Thermophys. Eng. 12 (2008) 251.

[24] L.S. Lobo, D.L. Trimm, J. Catal. 29 (1973) 15.

[25] C.A. Bernardo, L.S. Lobo, J. Catal. 37 (1975) 267.

[26] B.J. Cooper, D.L. Trimm, J. Catal. 62 (1980) 35.

[27] T. Baird, J.R. Fryer, B. Grant, Carbon 12 (1974) 591.

[28] E.F. Kukovitsky, S.G. L'vov, N.A. Sainov, V.A. Shustov, Appl. Surf. Sci. 215 (2003) 201.

[29] C. Du, N. Pan, Mater. Lett. 59 (2005) 1678.

[30] S. Talapatra, S. Kar, S.K. Pal, R. Vajtai, L. Ci*et al.*, Nat. Nanotechnol. 1 (2006) 112.

[31] N.K. Reddy, J.L. Meunier, S. Coulombe, Mater. Lett. 60 (2006) 3761.

[32] C. Masarapu, B. Wei, Langmuir 23 (2007) 9046.

[33] C.V. Varanasi, J. Bulmer, L. Brunke, J. Burke, J. Baca*et al.*, Vacuum Science and Technology A: Vacuum, Surfaces and Films 26 (2008) 832.

[34] C.E. Baddour, F. Fadlallah, D. Nasuhoglu, R. Mitra, L. Vandsburger*et al.*, Carbon 47 (2009) 313.

[35] C. Park, R.T.K. Baker, J. Catal. 179 (1998) 361.

[36] D. Sebastián, I. Suelves, M.J. Lázaro, R. Moliner, J. Power Sources 192 (2009) 51.

[37] J.K. Chinthaginjala, L. Lefferts, Carbon 47 (2009) 3175.

[38] V. Martínez-Hansen, N. Latorre, C. Royo, E. Romeo, E. García-Bordejé*et al.*, Catal. Today 147 (2009) S71-S75.

[39] A. Sacco Jr, F.W.A.H. Geurts, G.A. Jablonski, S. Lee, R.A. Gately, J. Catal. 119 (1989) 322.

[40] G.A. Jablonski, F.W. Geurts, A. Sacco Jr, R.R. Biederman, Carbon 30 (1992) 87.

[41] G.A. Jablonski, F.W.A.H. Geurts, A. Sacco Jr, Carbon 30 (1992) 99.

[42] C.A. Bernardo, L.S. Lobo, Stud. Surf. Sci. Catal. 6 (1980) 409.

[43] F.W.A.H. Geurts, R.G. Cnossen, A. Sacco Jr, R.R. Biederman, Carbon 32 (1994) 1151.

[44] D. Park, Y.H. Kim, J.K. Lee, Carbon 41 (2003) 1025.

[45] Y. Nishiyama, Y. Tamai, J. Catal. 33 (1974) 98.

[46] I. Alstrup, M.T. Tavares, C.A. Bernardo, O. Sørensen, J.R. Rostrup-Nielsen, Materials and Corrosion - Werkstoffe und Korrosion 49 (1998) 367.

[47] Y. Li, J. Chen, L. Chang, Y. Qin, J. Catal. 178 (1998) 76.

[48] P.E. Nolan, D.C. Lynch, A.H. Cutler, Carbon 34 (1996) 817.

[49] P.R.S. Jackson, D.L. Trimm, D.J. Young, J. Mater. Sci. 21 (1986) 3125.

[50] Y. Nishiyama, K. Moriguchi, N. Otsuka, T. Kudo, Mater. Corros. 56 (2005) 806.

[51] M.D. Abad, J.C. Sánchez-López, A. Berenguer-Murcia, V.B. Golovko, M. Cantoro *et al.*, Diamond Relat. Mater. 17 (2008) 1853.

[52] C.A. Bernardo, I. Alstrup, J.R. Rostrup-Nielsen, J. Catal. 96 (1985) 517.

[53] C. Pham-Huu, R. Vieira, B. Louis, A. Carvalho, J. Amadou *et al.*, J. Catal. 240 (2006) 194.

[54] J. Zhang, D.M.I. Cole, D.J. Young, Mater. Corros. 56 (2005) 756.

[55] N. Krishnankutty, N.M. Rodriguez, R.T.K. Baker, J. Catal. 158 (1996) 217.

[56] R. Moliner, Y. Echegoyen, I. Suelves, M.J. Lázaro, J.M. Palacios, Int. J. Hydrogen Energy 33 (2008) 1719.

[57] Y.M. Shyu, F. Chau-Nan Hong, Diamond Relat. Mater. 10 (2001) 1241.

[58] J.L. Figueiredo, Materials and Corrosion - Werkstoffe und Korrosion 50 (1999) 696.

[59] R.T.K. Baker, J.R. Alonzo, J.A. Dumesic, D.J.C. Yates, J. Catal. 77 (1982) 74.

[60] D. Park, Y.H. Kim, J.K. Lee, J. Mater. Sci. 38 (2003) 4933.

[61] C. Bernardo, D.L. Trimm, Carbon 14 (1976) 225.

[62] J.K. Chinthaginjala, D.B. Thakur, K. Seshan, L. Lefferts, Carbon 46 (2008) 1638.

Chapter 3

Influence of reaction parameters on the attachment of a carbon nanofiber layer on Ni foils

"I would like to have enough money to live as tranquil as poor people" (Pablo Picasso)

Abstract

Dense carbon (C) and entangled carbon nanofiber (CNF) layers are deposited on nickel foils by decomposition of ethylene in presence of different H_2 concentrations at 450°C for different reaction times. Both C and CNF layer thicknesses increase with time, but samples pre-oxidized at 500°C normally lead to thinner CNF layers and thicker C layers, as compared to samples pre-oxidized and reduced at 700°C. CNFs are more crystalline than the C layer, although the addition of H_2 during the reaction increases the amount of defects. The mechanical stability of CNFs decreases with growth time, especially for oxidized-reduced samples. The addition of H_2 creates a maximum in the CNF thickness that coincides with a minimum in the C layer thickness, at 5% H_2 concentration for samples oxidized at 500°C and at 20% H_2 concentration for samples oxidized-reduced at 700°C. The CNF layer stability increases with the C layer thickness but decreases with the CNF layer thickness. The ratio between the C layer thickness and the CNF thickness determines in the end the mechanical stability of the CNF layer.

This chapter is based on the publication: S. Pacheco Benito, L. Lefferts. *Surface and Coating Technology* (submitted)

Chapter 3

3.1 Introduction

Carbon nanofibers (CNFs) [1-5] and carbon nanotubes (CNTs) [6-12] have recently attracted intense research efforts with the expectation that these materials have unique properties. CNFs and CNTs can be synthesized *via* three main processes: arc-discharge [13-15], laser ablation [16-17], or catalytic chemical vapor deposition (C-CVD). With regard to large-scale synthesis, the C-CVD route is by far the most feasible option in terms of cost and energy requirements. CNFs and CNTs offer various properties such as high surface area, high thermal and electronic conductivity, high mechanical stability and high inertness. These properties make CNFs and CNTs promising for many applications such as catalyst supports [18-21], batteries and fuel cells [22-24], hydrogen storage [25-26], polymer reinforcements [27-28], supercapacitors [29], sensors and nanoprobes [30] and super-hydrophobic layers [31-32]. Our main interest is in applications of thin layers of CNF supported on mesoscopic structured material, *i.e.* foams, foils and other surfaces.

In general, the growth of carbon nanostructures requires catalyst nanoparticles (usually Ni, Fe, or Co), a carbon feedstock (hydrocarbon or CO) and high temperatures (400-1000°C). The most commonly accepted mechanism for the growth of CNFs was postulated by Baker *et al.* on pre-shaped Ni nanoparticles [33]. According to this mechanism, the hydrocarbon first decomposes on the surface of a metal nanoparticle, then carbon diffuses through the particle and finally, it precipitates to form the carbon filament. However, Chinthaginjala *et al.* [34] showed that CNFs and a dense carbon layer (C layer) grow simultaneously on Ni foams, suggesting that an alternative mechanism might occur on polycrystalline materials. This C layer looks apparently dense but it has high surface area and it grows specially the first minutes of the reaction, when the Ni particles are still too big to form CNFs [34]. The C layer forms between the substrate and the CNF layer and facilitates the attachment of the C and CNF layers to the substrate. The deposition of a dense C layer and carbon filaments on metal foils has also been reported in literature [35-40].

One advantage of growing CNFs on polycrystalline metal, *e.g.* foils, is that deposition of catalyst nanoparticles is not needed. Apparently, nanoparticles are created either as a result of any pretreatment or during the initial stages of carbon deposition [40-41]. However, the type of pretreatment determines the carbon deposition rate [41-42], as we observed in **chapter 2**. Moreover, it is well known that addition of H_2 during catalytic CNF growth influences both the carbon deposition rate as well as the morphology of the CNFs. Hydrogen is known to either accelerate [43-50] or suppress [51-52] the formation of CNFs or CNTs depending on the H_2/hydrocarbon ratio and the type of catalyst. High H_2 concentrations normally lead to low initial deposition rates, but the total level of deposition increases because of reduced deactivation rates. The addition of H_2 has also been reported to decrease the diameter of CNFs [53-56].

Formation of carbon and CNFs on metal surfaces has been studied intensively in the past because these phenomena are a nuisance in *e.g.* stainless-steel reactor pipes in steam-cracking units, operating at temperatures higher than 700°C [57-58]. In contrast, controlled preparation of CNF layers on pure metals, aiming at preparation of a functional material, has not been studied in great detail so far. Furthermore, characterization of CNF layers on surfaces in terms of mechanical stability has not been addressed, whereas this is of crucial importance when aiming at applications of the resulting materials as catalyst support, nano-electronics, super-capacitors or polymer reinforcement [18, 56, 59-63]. Poor mechanical stability would not only compromise the performance for the targeted applications, but loose fibers could also induce a risk for human health [64-65]. There are no systematic studies available on the influence of reaction conditions on the attachment of dense and filamentary carbon layers on Ni foils.

In **chapter 2**, we observed that homogeneity and attachment of carbon layers deposited on different metal foils at 600°C varied with the composition of the metal foil, addition of H_2 and type of pretreatment. In this chapter, we report on the factors that control the attachment of the CNFs to a Ni foil. We have systematically studied the influence of reaction parameters, such as H_2 concentration, reaction time and pretreatment, on the attachment of the C layer and CNF layer on the Ni foil.

3.2 Experimental

3.2.1 Materials

Nickel foils (0,1mm thick, 99,5%, Alfa Aesar) were used as active catalytic substrates. Square sample pieces (10 x 10mm) were prepared from the as-received sheet by wire cut electrical discharge machining (Agiecut Challenge 2). The foils were degreased ultrasonically in acetone and dried at room temperature before being loaded into a quartz tube. Hydrogen, nitrogen and air (99,999%, Praxair), and ethylene (99,95%, Praxair) were used for CNFs formation without further purification.

3.2.2 Carbon nanostructures formation

An in-house built vertical catalytic chemical vapor deposition (C-CVD) reactor was used to grow carbon nanostructures. It consists of a 12mm inner diameter quartz reactor. The temperature was raised in N_2 from room temperature to the desired temperature at a rate of 7,5 °C/min. The samples were first pretreated according to two different methods. The first pretreatment consists of oxidation in air (20% air and balance N_2) under a total flow rate of 100ml/min for 1 hour at 500°C. The second pretreatment consists of oxidation in static air for 1 hour at 700°C followed by reduction in hydrogen (20% H_2 and balance N_2) for 2 hours at 700°C. N_2 was used to flush the reactor for 5 minutes, for safety reasons, when switching between air and hydrogen. The different pretreatments will be denoted as Oxid 500 and Oxid/Red 700 respectively.

After the pretreatment, the temperature was adjusted to 450°C in N_2. The CNFs were grown using a gas mixture of hydrogen and ethylene (C_2H_4) in nitrogen with a total flow rate of 100ml/min. The concentration of C_2H_4 (25% v/v) was kept constant in all experiments and the nitrogen flow was adjusted whenever hydrogen concentration (0–50%) was modified. The CNF growth time was varied between 5 and 180 minutes. Finally, ethylene and hydrogen (if used) gas streams were shut off and the system was cooled down to room temperature under 100ml/min of N_2 at a rate of 10°C/min.

3.2.3 Characterization

The mechanical stability of the carbon layers was characterized by flowing nitrogen (120l/min) for 1min over the flat samples in a cylindrical quartz tube

(11mm diameter) at a linear speed of 21m/s. The attachment of the carbon layers was assessed by the difference in weight between the sample after synthesis, including loose carbon, and after blowing it with nitrogen. The weight loss percentage is calculated accounting for the total weight of carbon deposited. The weights were calculated using a Metler Toledo AE163 balance with precision up to 0,01mg. The morphology and cross sections of the carbon layers were studied using a scanning electron microscope (SEM) JEOL 6250LV, equipped with secondary electrons detector. Cross sections were obtained by cutting the samples with a pair of scissors after immersing them shortly in liquid N_2 to prevent the loss of the weakly attached fibers. The averaged thicknesses of the carbon layers were calculated from 10 measurements of the thickness at different locations at cross section in SEM pictures using the freeware ImageJ [66]. Raman spectra were taken with a Bruker Senterra Raman Spectrometer equipped with a cooled CCD detector (-60°C), 532nm laser, 2mW, and 50x10µm aperture. Spectra were acquired at a resolution of 9-15cm^{-1} and 10 scans were accumulated for each spectrum.

3.3 Results

Figure 3.1 shows one typical top view morphological picture of a dense C layer (**figure 3.1a**), a porous and entangled CNF layer (**figure 3.1b**) and one cross section picture clearly showing a dense C layer under a porous CNF layer (**figure 3.1c**), typical for the results obtained in this study. In contrast to the results on CNF growth on Ni foils at 600°C shown in **chapter 2**, all the samples of the present study at 450°C present either homogenous dense carbon layers or homogenous CNF layers.

3.3.1 Influence of pretreatment

Figure 3.2 shows the morphology of the fresh and pretreated Ni foil. The fresh sample (**figure 3.2a**) does not show clear grain boundaries. However, oxidation at 500°C (**figure 3.2b**) induces the formation of grains in the range 5-20µm. The typical weight increase after oxidation at 500°C is 0,08mg, resulting in an estimated thickness of 60nm of NiO (density 6,7g/cm^3 [67]). Oxidation-reduction at 700°C (**figure 3.2c**) creates grains in the range 0,5-5µm, in agreement with previous results on Ni foam [41]. The weight increase was below the detection limit (0,01mg).

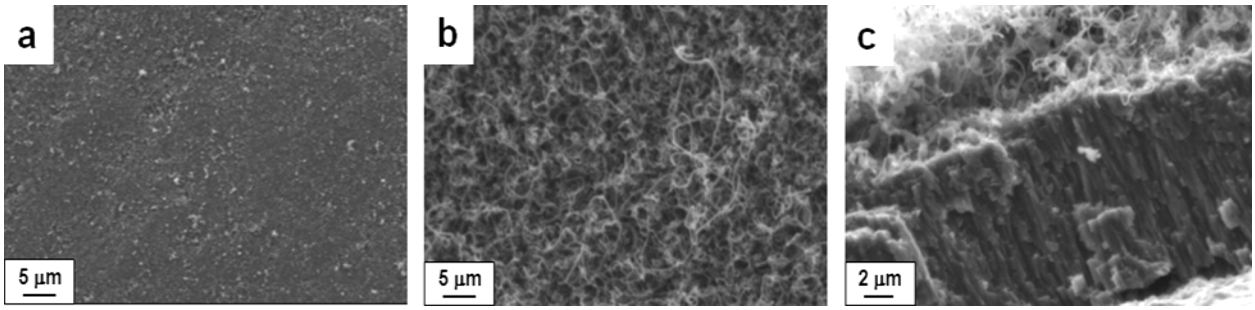

Figure 3.1: *representative SEM pictures of the carbon layers obtained at 450°C before the air flow test. a) Dense C layer grown on an oxidized/reduced sample after 60 min of reaction and 0% H_2; b) porous and entangled CNF layer grown on an oxidized/reduced sample after 60 min of reaction and 10% H_2; c) cross section showing both C and CNF layer grown on an oxidized sample after 60 min of reaction and 0,3% H_2*

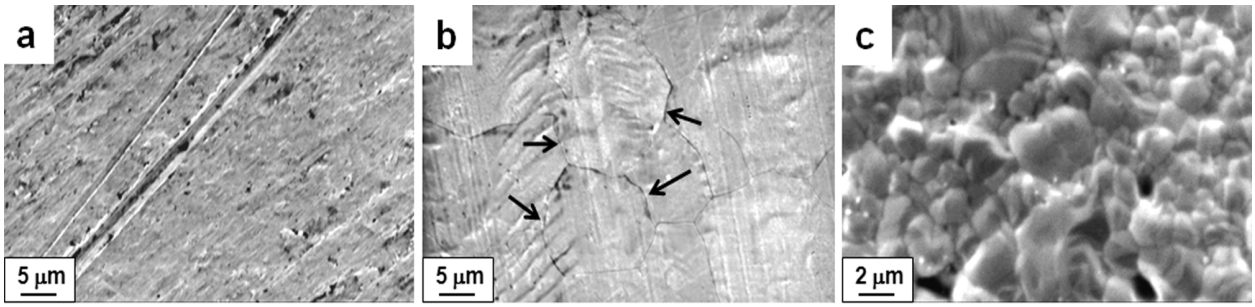

Figure 3.2: *influence of pretreatment on the grain size of a Ni foil.*
a) No pretreatment; b) oxidation at 500°C; c) oxidation-reduction at 700°C

3.3.2 Influence of H_2 concentration

Figure 3.3 shows representative SEM pictures of both CNF as well as C layers formed when adding different concentrations of H_2 during growth on Oxid/Red 700 samples. The magnification has been adjusted depending on the thickness of the C and CNF layers to allow assessment of the thickness of both layers. If the C layer is not clearly visible in the low magnification SEM picture, a representative inset with higher magnification of the C layer is presented.

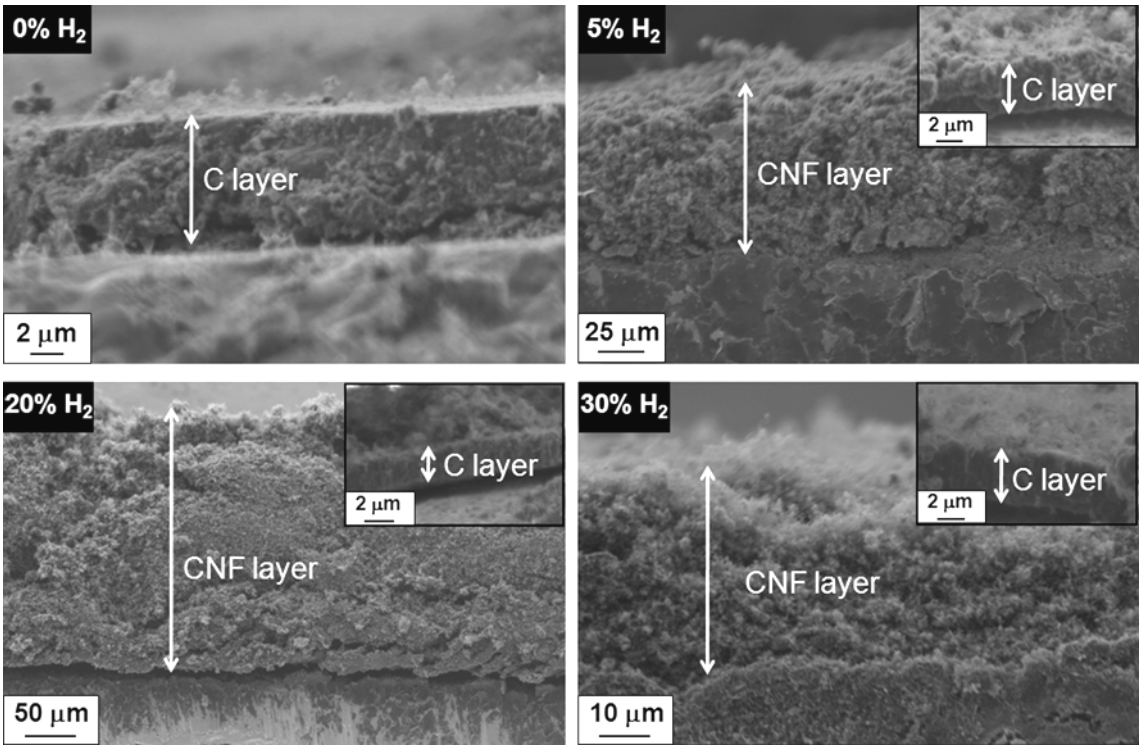

Figure 3.3: *cross section SEM pictures of the dense carbon layer and CNF layer for oxidized/reduced samples, 60 min of reaction at 450°C and different concentrations of H_2. Insets of the carbon layers taken in other spots at higher magnification are added when they are not clearly visible at lower magnification*

The influence of H_2 was studied by varying the H_2 concentration between 0 and 30% for the samples oxidized at 500°C and between 0 and 50% for the samples oxidized and reduced at 700°C, as shown in **figure 3.4**. **Figure 3.4a** shows the influence of the H_2 concentration on the thickness of the CNF layer before removing any loosely attached carbon. The thickness of the CNF layer shows a maximum at intermediate H_2 concentrations, *i.e.* at 5% H_2 for samples oxidized at 500°C and at 20%H_2 for samples oxidized/reduced at 700°C. It is interesting to note that, for both pretreatments, no CNFs are formed in absence of H_2 addition. It is widely known that the addition of H_2 is necessary to prevent catalyst deactivation on metal foils, enabling CNF growth [39, 46-47, 68-70]. Moreover, we observe that there is no formation of CNFs if 50% H_2 is added for Oxid/Red 700 samples (**figure 3.4a**).

Figure 3.4b shows the variation of the C layer thickness, before the air flow test, with the addition of H_2. For both pretreatments, the C layer thickness decreases with the H_2 concentration, reaching a minimum at 5% H_2 for the Oxid 500 samples and at 20% H_2 for the Oxid/Red 700 samples (**figure 3.4b**). This result for the Oxid/Red 700 samples agrees well with our previous observations on Ni foam that the C layer thickness decreases with increasing H_2 concentration from 0 to 14% [34]. The H_2 concentration at which the C layer is the thinnest coincides with the one at which the CNF layer is the thickest (**figures 3.4a and 3.4b**). The C layer is always thicker, independent of the amount of H_2 added, if the samples are oxidized at 500°C. Moreover, the CNF layer is generally much thicker than the C layer.

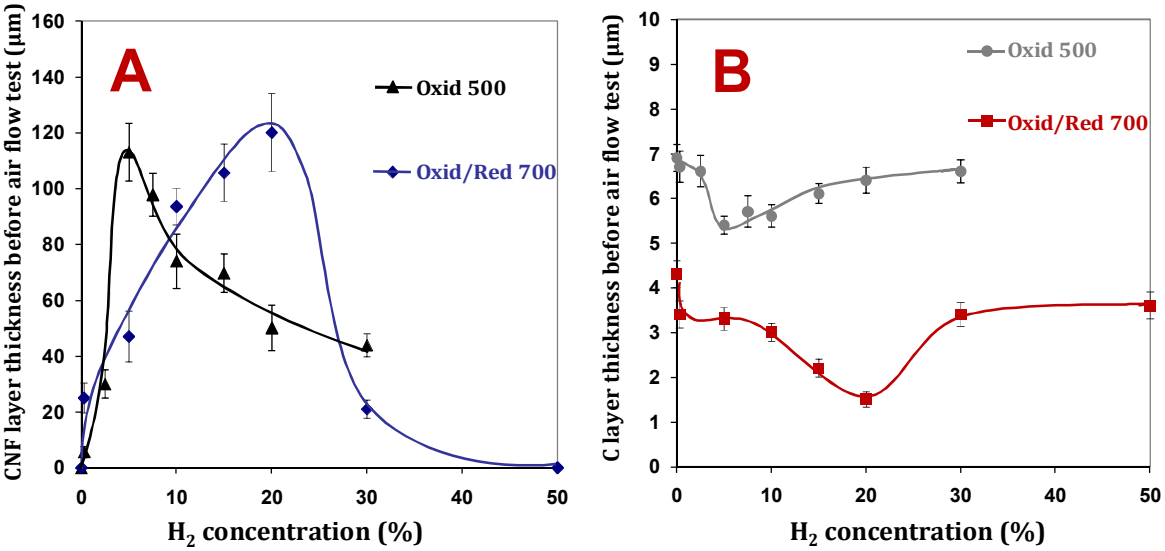

Figure 3.4: *influence of H_2 addition during the carbon growth for 60 min. a) On the CNF layer thickness before the air flow test; b) on the C layer thickness before the air flow test*

3.3.3 Influence of reaction time

Figure 3.5 shows representative SEM pictures of both CNF as well as C layer thicknesses deposited after different reaction times using 10% H_2 for samples oxidized at 500°C. If the C layer is not clearly visible in the low magnification SEM picture, representative inset higher magnification pictures of the C layer are presented.

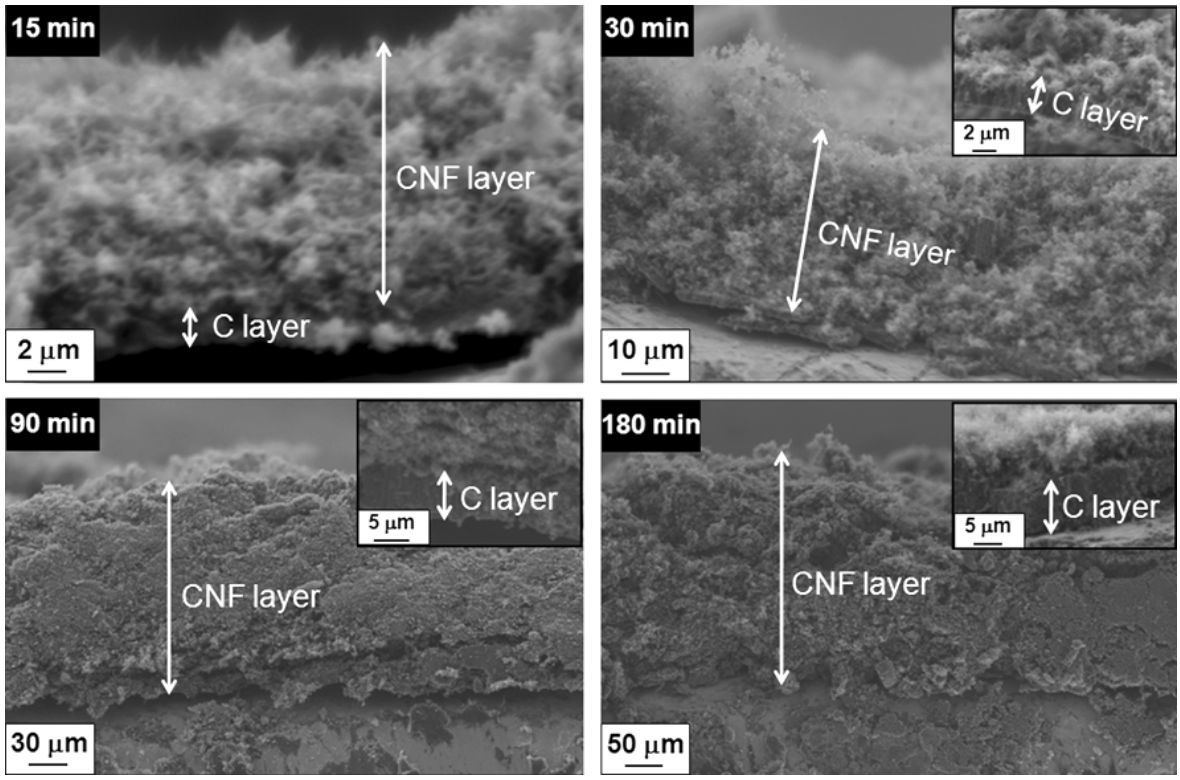

Figure 3.5: *cross section SEM pictures of the dense C layer and CNF layer for oxidized samples, addition of 10% H_2 at 450°C and different times of reaction. Insets of the C layers taken in other spots at higher magnification are added when they are not clearly visible*

Figure 3.6 presents the resulting dependence of both the CNF and C layer thicknesses, before the air flow test, with the reaction time. For this study two H_2 concentrations, 0,3% and 10%, per pretreatment have been used. **Figure 3.6a** shows that, as expected, the CNF layer thickness increases with time. The layers are clearly thicker when the H_2 concentration is higher, independent of the pretreatment. However, the Oxid/Red 700 samples present thicker CNF layers, as compared to the Oxid 500 samples, for the selected H_2 concentrations.

Figure 3.6b shows that in all cases the C layer thickness increases with time, but not linearly. It is interesting to note that the growth of the C layer is relatively fast during the first 60 minutes and then it grows slower. Furthermore, the Oxid 500 samples present thicker C layer thickness than the Oxid/Red 700 samples, independent of the time of reaction.

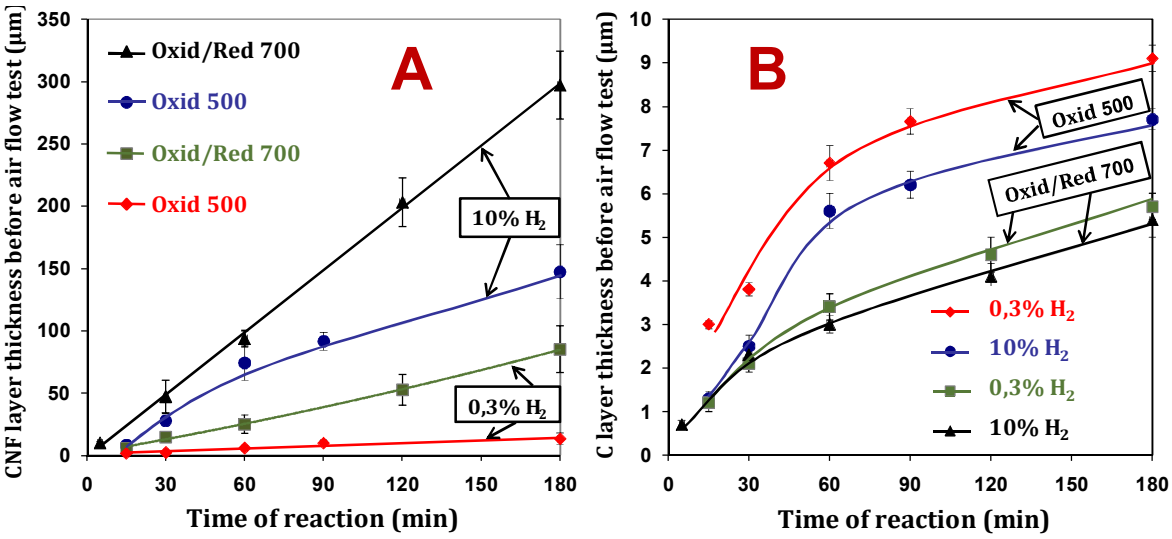

Figure 3.6: *influence of time of the reaction a) on the CNF layer thickness before the air flow test; b) on the C layer thickness before the air flow test*

3.3.4 Attachment

Figure 3.7a shows the dependence of the carbon weight loss, as a result of the air flow test, with the H_2 concentration for both pretreatments and after 60 min of carbon growth. We observe that, similarly to the dependence of the CNF layer thickness with the H_2 concentration shown in **figure 3.4a**, the carbon weight loss increases with H_2 addition reaching a maximum and then it decreases. The maxima of the carbon weight loss coincides with the maxima shown in **figure 3.3a**, *i.e.* at 5% H_2 concentration for the samples oxidized at 500°C and at 20% H_2 concentration for samples oxidized-reduced at 700°C. Interestingly, oxidation at 500°C leads to lower carbon weight loss than the oxidation-reduction at 700°C pretreatment, independent of the H_2 concentration.

Figure 3.7b shows the variation of the carbon weight loss with the reaction time for both pretreatments and 0,3% and 10% H_2 concentration. The carbon weight loss increases with the reaction time in all cases. Moreover, samples oxidized-reduced at 700°C show clearly a higher carbon weight loss than samples oxidized at 500°C, for the same H_2 concentration. However, the combination of Oxid/Red 700 samples with 0,3% H_2 result in lower carbon weight loss than the combination of Oxid 500 samples with 10% H_2 during the first 80 minutes (**figure 3.7b**). When samples are oxidized at 500°C and the H_2 concentration is as low as

0,3%, the weight loss remains below 10%. On the other hand, samples oxidized-reduced at 700°C and 10% H_2 reach a carbon weight loss as high as 83%.

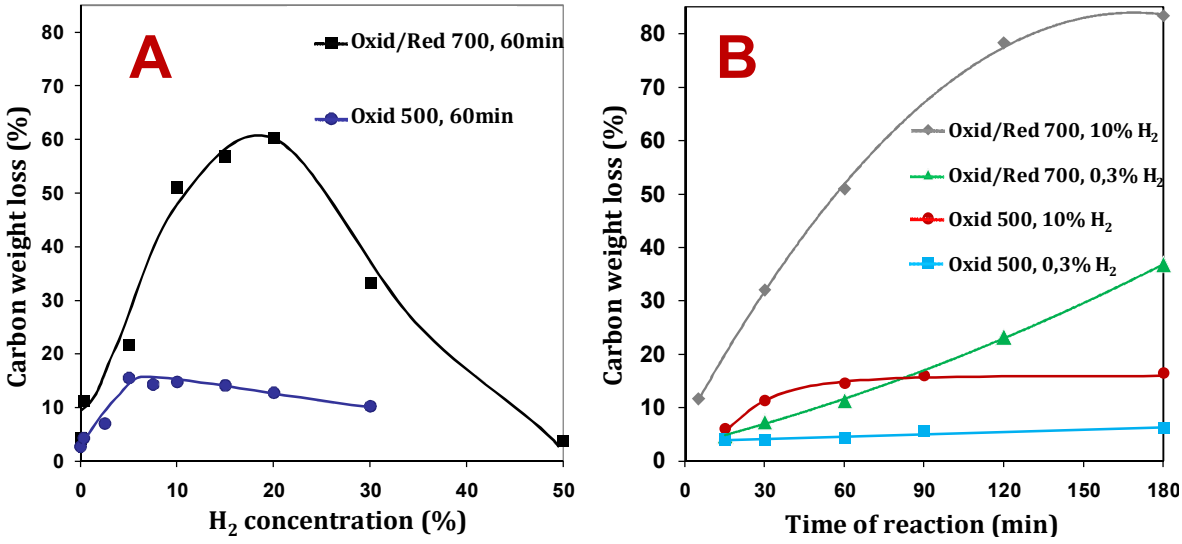

Figure 3.7: *influence of reaction parameters on the carbon weight loss (%) accounting for the total amount of carbon deposited. a) Amount of hydrogen; b) time of the reaction*

3.3.5 Raman spectroscopy

Figure 3.8 shows normalized Raman spectra, in the range 750-1950cm^{-1}, of a set of selected samples with different pretreatment, H_2 concentration and time of reaction (solid lines). The exact conditions of each sample are summarized in **table 3.1**. No considerable differences have been found in the remaining Raman spectra from 200-3500cm^{-1}. All samples show the two most prominent peaks assigned to carbon: one centered at 1347±4cm^{-1} and other one centered at 1590±4cm^{-1}. The first peak is usually termed as the D band and it indicates the presence of disordered carbon (nano and micro-crystalline graphite and amorphous carbon); whereas the second peak is usually termed as G band and it denotes the presence of crystalline graphitic sp^2 carbon [71-74]. The intensity ratio of the D and G bands, I_D/I_G, is widely used for characterizing the defect quantity in graphitic materials. A low ratio denotes highly ordered graphite with high crystallinity.

I_D/I_G has been calculated following two different methods. The first one takes into account the height intensity of both peaks with respect to the baseline. The second method uses the integrated intensity area of both peaks after the

deconvolution of the spectra in four bands (dashed lines in **figure 3.8**), which is the minimum number of bands necessary for obtaining a good fit to the spectra. **Table 3.1** presents the I_D/I_G values for the two methods. The values obtained are in the same order as previously reported in literature for CNFs [72, 75-76]. It appears that both methods result in similar trends in the ratios as function of the preparation conditions, demonstrating that the simplified calculation based on peak heights is acceptable in this case. We clearly observe that the samples containing exclusively the C layer (**samples A and B**) reveal more defects than the rest of the samples that contain a CNF layer, independent of the pretreatment and reaction conditions. This result agrees well with the fact that the C layer is nano-crystalline, previously reported on Ni foam [34], whereas ordering in CNFs is much more pronounced. Interestingly, for similar pretreatment and reaction time (**samples C and D**), we observe that the addition of H_2 makes CNFs less crystalline, in agreement with observations in literature [77]. If the CNF layer thickness is quite thin (**sample E**), the apparent crystallinity is probably affected by a contribution of the disordered C layer to the Raman peak.

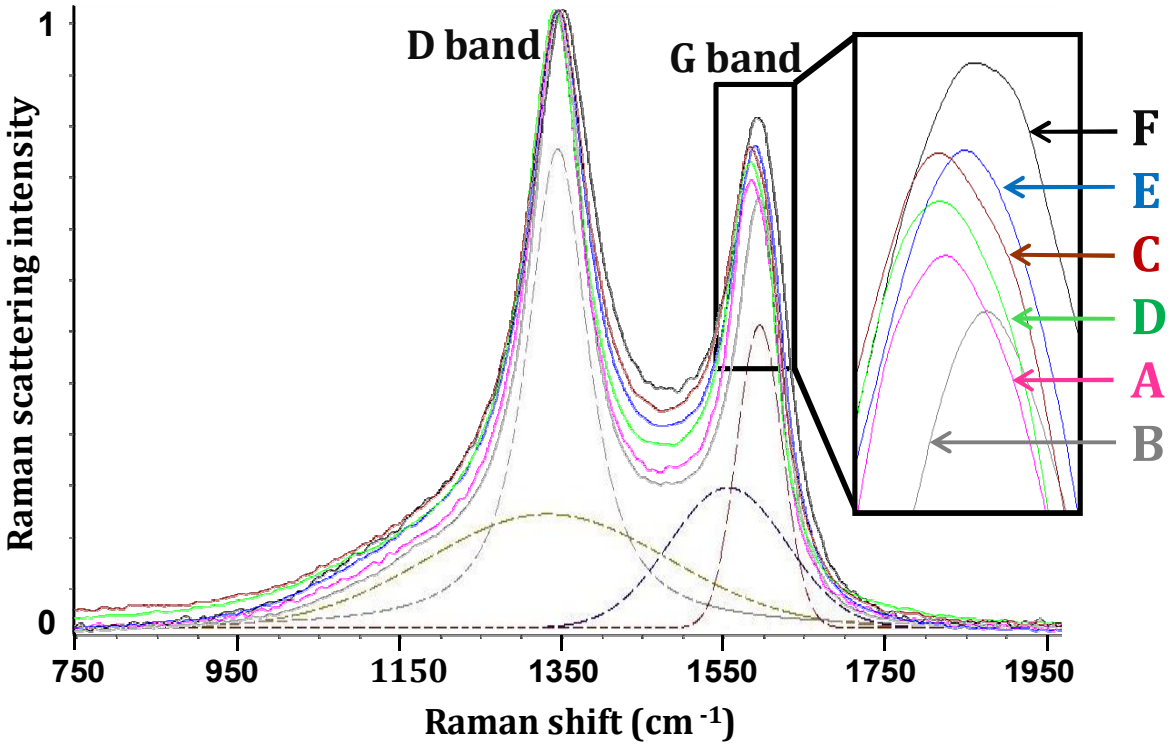

Figure 3.8: *normalized Raman spectra of samples A-F after reaction conditions according to table 3.1*

Table 3.1: *ratio between intensities of D and G bands in Raman for series of samples varying pretreatment, H_2 concentration and reaction time*

Sample	*Pretreatment*	*H_2 conc. (%)*	*Reaction time (min)*	*C layer thickness (µm)*	*CNF layer thickness (µm)*	*I_D/I_G height*	*I_D/I_G area*
A	***Oxid/red 700***	0	60	4,3	0	1,38	2,91
B	***Oxid 500***	0	60	7,0	0	1,40	2,80
C	***Oxid/red 700***	5	60	3,3	47	1,30	2,58
D	***Oxid/red 700***	20	60	1,5	120	1,34	2,73
E	***Oxid 500***	0,3	30	3,8	2,0	1,29	2,57
F	***Oxid 500***	0,3	180	7,7	9,7	1,21	2,52

3.4 Discussion

3.4.1 Effect of C and CNF layer thickness

Figure 3.9a shows the carbon weight loss as function of the thickness of the CNF layer, before the air flow test, obtained by varying the reaction time and operating with 10% H_2 addition. We observe that samples oxidized-reduced at 700°C present more carbon loss than samples oxidized at 500°C, independent of the CNF layer thickness. This difference becomes more significant for thicker layers, *e.g.* for a CNF layer thickness of 95µm, the carbon weight loss increases from 17% (Oxid 500 sample) to 51% (Oxid/Red 700 sample). Remarkably, samples oxidized at 500°C show very limited carbon weight loss, increasing from 5 to 17% with increasing CNF layer thickness. **Figure 3.9b** shows the carbon weight loss as function of the C layer thickness obtained by variation of H_2 concentration and reaction time for Oxid 500 samples. There are two main observations: 1) when the reaction time is varied, the carbon weight loss increases with the C layer thickness; 2) when the H_2 concentration is changed, the carbon weight loss decreases with the C layer thickness. The second observation agrees well with our previously reported results on Ni foam [53].

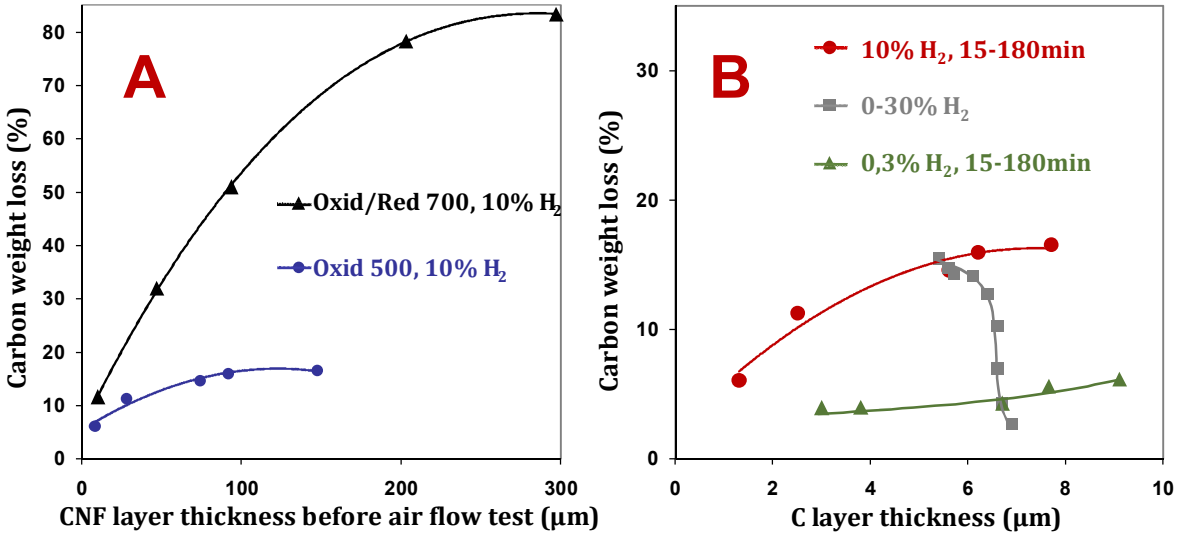

Figure 3.9: *carbon weight loss after the air flow test as function of: a) CNF layer thickness before the air flow test obtained by varying the reaction time; b) the C layer thickness for the samples oxidized at 500°C*

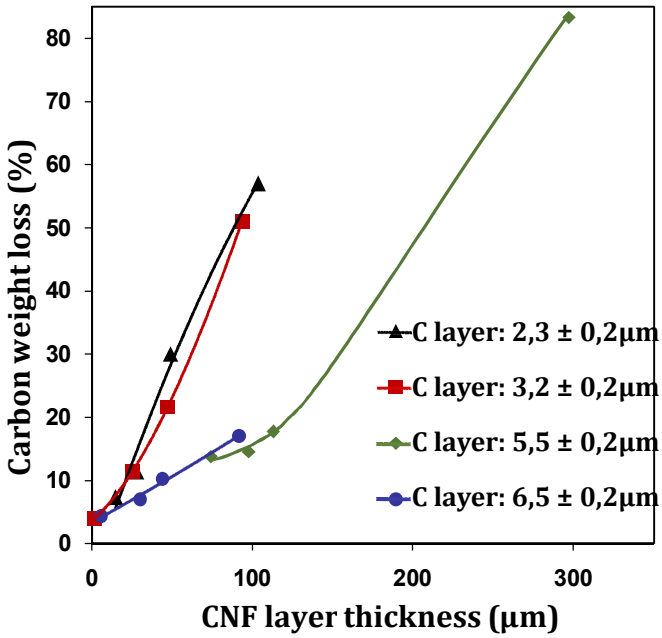

Figure 3.10: *influence of CNF layer thickness on the carbon weight loss for similar C layer thickness*

In order to separate the effects of C layer thickness *versus* CNF layer thicknesses, we selected samples with similar C layer thickness and varying CNF layer thickness, by using data obtained with different pretreatments and reaction conditions. **Figure 3.10** shows the relation between the carbon weight loss and the

CNF layer thickness for four series of samples with similar C layer thicknesses. It is clear that in all cases the carbon weight loss increases with the CNF layer thickness, independent of the C layer thickness. However, the loss of CNFs is more pronounced when the C layer is thinner. This corresponds to the fact that Oxid/Red 700 samples generally grow thinner C layers than Oxid 500 samples (**figures 3.4b and 3.6b**), leading to higher carbon weight loss (**figures 3.7 and 3.9a**).

We are also able to select data with similar CNF layer thickness and varying C layer thickness, by using data obtained at different pretreatments and reaction conditions. **Figure 3.11** shows the relation between the carbon weight loss and the C layer thickness for three series of samples with similar CNF layer thicknesses. It is clear that in all cases the carbon weight loss decreases when the C layer thickness increases, independent of the CNF layer thickness. Therefore, CNFs that grow from thinner C layers are weaker bonded than CNFs growing from thicker C layers. This supports our hypothesis that the CNFs are attached to the metal substrate *via* roots in the C layer as proposed in our earlier work [34]; thus, the thicker the C layer, the stronger the growing CNFs are rooted to the C layer. Moreover, the effect of the C layer on the carbon weight loss becomes more sensitive when the CNF layer thickness increases.

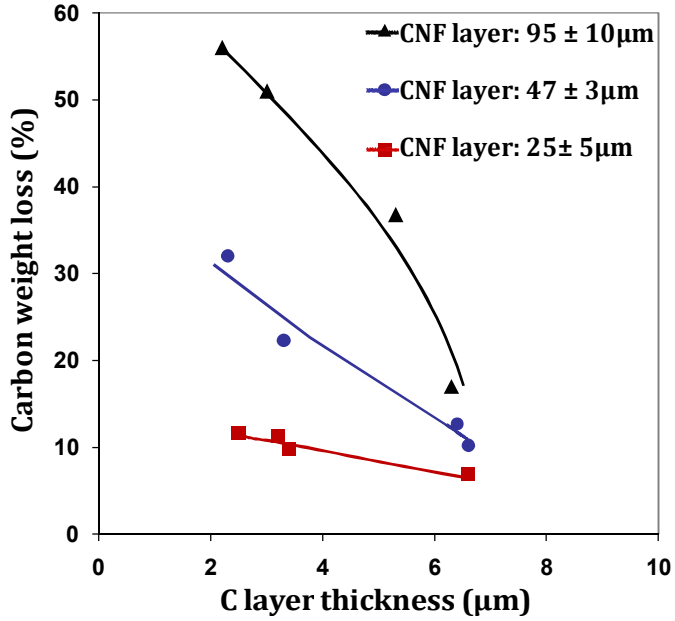

Figure 3.11: *influence of the C layer thickness on the carbon weight loss for similar CNF layer thickness*

3.4.2 Influence of reaction parameters on attachment

We propose that the mechanical stability of the CNFs is influenced by both the C and CNF layer thicknesses. **Figure 3.12** shows the dependence of the carbon weight loss with the ratio between the C layer thickness and CNF layer thickness for all combinations of pretreatments and reaction conditions used in this study. It can be observed that when the ratio is higher than 0,2 the carbon weight loss is less than 7%. Whereas if the ratio is lower than 0,2 the carbon weight loss increases significantly. Therefore, the description based on the ratio of thicknesses C/CNF can explain the effects observed in **figures 3.10 and 3.11**.

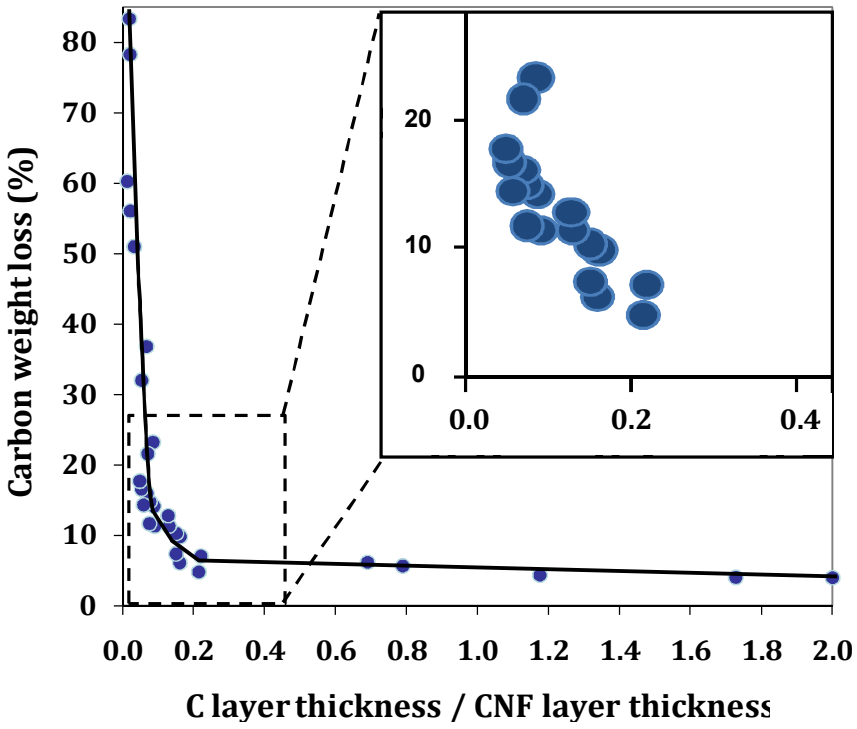

Figure 3.12: *carbon weight loss after the air flow test as function of the ratio between the C layer thickness and the CNF layer thickness before the air flow test*

When the reaction time increases, both C and CNF layer thicknesses increase (**figure 3.6**); therefore, the carbon weight loss also increases with the reaction time (**figure 3.7b**). However, the addition of H_2 leads to a maximum in CNF layer thickness at intermediate H_2 concentration (**figure 3.4a**), that coincides with a minimum in C layer thickness (**figure 3.4b**). Therefore, the description based on ratio of C/CNF thicknesses can explain the maximum in CNF loss as observed in **figure 3.7a**.

As we presented in **figure 3.4a**, Oxid 500 samples grow thicker CNF layers than Oxid/Red 700 samples approximately in the range 3-8% H_2 concentration. However, the C layer of Oxid 500 samples is thicker than Oxid/Red 700 samples independent of the H_2 concentration (**figures 3.4b**). Again, the description based on ratio of C/CNF thicknesses explains also that Oxid 500 samples result in a better attachment than Oxid/Red 700 samples.

Jarrah *et al.* reported [41] that, without adding H_2, the formation of small Ni particles on Ni foam *via in-situ* reduction of NiO (oxidation pretreatment) is faster than *via* formation and decomposition of meta-stable Ni_3C (oxidation-reduction pretreatment). Interestingly, without addition of H_2, we do not observe CNF growth on Ni foil for any pretreatment (**figure 3.4a**), instead a thicker C layer after oxidation (**figure 3.4b**). The ability of the Ni foam to grow CNFs without addition of external H_2 [41] is probably due to the relatively high surface area of the Ni foam, as compared to the Ni foil, therefore more H_2 is formed according to **eq. 3.1**:

$$C_2H_4 \longrightarrow 2C + 2H_2 \qquad \textbf{(eq. 3.1)}$$

H_2 enables or increases the CNF growth rate by preventing catalyst deactivation *via* encapsulation due to excess carbon on the Ni surface [68, 78-80]. This autocatalytic effect of H_2 [69] is probably more important for the Ni foam, that has relatively high surface area, than for the Ni foil because of the higher ethylene conversion. In our study we observe an optimum in CNF layer thickness with H_2 concentration (**figure 3.4a**) probably due to the competitive adsorption of hydrogen and ethylene for the active sites [53, 81]. Moreover there is a sharp increase of the CNF growth rate with H_2 for oxidized samples, as compared to oxidized-reduced, probably because of fast formation of Ni nanoparticles from NiO in presence of H_2.

3.5 Conclusions

Carbon layers comprising both dense C layers and entangled CNF layers have been prepared by decomposition of ethylene on nickel foils in presence of hydrogen at 450°C at different reaction times. The stability of the CNF layer is determined by the ratio between the thickness of the C layer and the CNF layer. When the ratio is higher than 0,2, the carbon weight loss is smaller than 7%. For lower ratios the carbon weight loss can increase up to 85%. Therefore, the preparation of stable and thick CNF layers on Ni foils involves a compromise between the deposition of a thick C layer and the amount of weakly attached CNFs. The C layer thickness increases faster for samples oxidized at 500°C than samples oxidized-reduced at 700°C. Oxidized and oxidized-reduced samples present a maximum in the CNF layer thickness, at 5% and 20% H_2 concentration respectively, which coincides with a minimum in the C layer thickness. Both C and CNF layer thicknesses increase with growth time, but the mechanical stability decreases with growth time, especially for oxidized-reduced samples. Thus, samples oxidized at 500°C generally show better mechanical stability than oxidized-reduced samples at 700°C.

Acknowledgements

The author greatly acknowledges Dr. Barbara Mojet for scientific discussions on Raman spectroscopy.

References

[1] N.M. Rodriguez, J. Mater. Res. 8 (1993) 3233.

[2] J. Rostrup-Nielsen, D.L. Trimm, J. Catal. 48 (1977) 155.

[3] R.T.K. Baker, Carbon 27 (1989) 315.

[4] K.P. De Jong, J.W. Geus, Catal. Rev. Sci. Eng. 42 (2000) 481.

[5] V.V. Chesnokov, R.A. Buyanov, Russ. Chem. Rev. 69 (2000) 623.

[6] K.B.K. Teo, C. Singh, M. Chhowalla, W.I. Milne, in: H.S. Nalwa, (Eds.)Encyclopedia of Nanoscience and Nanotechnology, vol 10 (2003), p 1.

[7] T.W. Ebbesen, Carbon Nanotubes: Preparation And Properties. CRC Press, Boca Raton, Florida, 1997.

[8] P. Serp, M. Corrias, P. Kalck, Appl. Catal. A-General 253 (2003) 337.

[9] C. Öncel, Y. Yürüm, Fullerenes Nanotubes and Carbon Nanostructures 14 (2006) 17.

[10] N. Bajwa, X. Li, P.M. Ajayan, R. Vajtai, J. Nanosci. Nanotech. 8 (2008) 6054.

[11] R.H. Baughman, A.A. Zakhidov, W.A. De Heer, Science 297 (2002) 787.

[12] P.M. Ajayan, Chem. Rev. 99 (1999) 1787.

[13] D.S. Tang, S.S. Xie, B.H. Chang, L.F. Sun, Z.Q. Liu *et al.*, Nanotechnology 13 (2002).

[14] T.W. Ebbesen, P.M. Ajayan, Nature 358 (1992) 220.

[15] D.S. Bethune, C.H. Kiang, M.S. De Vries, G. Gorman, R. Savoy *et al.*, Nature 363 (1993) 605.

[16] W.K. Maser, E. Muñoz, A.M. Benito, M.T. Martínez, G.F. De La Fuente *et al.*, Chem. Phys. Lett. 292 (1998) 587.

[17] A. Thess, R. Lee, P. Nikolaev, H. Dai, P. Petit *et al.*, Science 273 (1996) 483.

[18] J.K. Chinthaginjala, J.H. Bitter, L. Lefferts, Appl. Catal. A 383 (2010) 24.

[19] N.M. de Almeida Coelho, J.L.B. Furtado, C. Pham-Huu, R. Vieira, Mater. Res. 11 (2008) 353.

[20] C. Pham-Huu, M.J. Ledoux, Top. Catal. 40 (2006) 49.

[21] J.K. Chinthaginjala, K. Seshan, L. Lefferts, Ind. Eng. Chem. Res. 46 (2007) 3968.

[22] K. Lee, J. Zhang, H. Wang, D.P. Wilkinson, J. Appl. Electrochem. 36 (2006) 507.

[23] R. Kannan, V.K. Pillai, J. Indian Inst. Sci. 89 (2009) 425.

[24] R. Chetty, S. Kundu, W. Xia, M. Bron, W. Schuhmann*et al.*, Electrochim. Acta 54 (2009) 4208.

[25] R. Strobel, J. Garche, P.T. Moseley, L. Jorissen, G. Wolf, J. Power Sources 159 (2006) 781.

[26] B. Panella, M. Hirscher, S. Roth, Carbon 43 (2005) 2209.

[27] M.H. Al-Saleh, U. Sundararaj, Carbon 47 (2009) 2.

[28] E. Hammel, X. Tang, M. Trampert, T. Schmitt, K. Mauthner*et al.*, Carbon 42 (2004) 1153.

[29] D. Hulicova-Jurcakova, X. Li, Z. Zhu, R. de Marco, G.Q. Lu, Energy and Fuels 22 (2008) 4139.

[30] M. Trojanowicz, Trends Anal. Chem. 25 (2006) 480.

[31] P.C. Tsai, S. Pacheco, C. Pirat, L. Lefferts, D. Lohse, Langmuir 25 (2009) 12293.

[32] H. Liu, J. Zhai, L. Jiang, Soft Matter 2 (2006) 811.

[33] R.T.K. Baker, M.A. Barber, P.S. Harris, F.S. Feates, R.J. Waite, J. Catal. 26 (1972) 51.

[34] J.K. Chinthaginjala, D.B. Thakur, K. Seshan, L. Lefferts, Carbon 46 (2008) 1638.

[35] T. Baird, J.R. Fryer, B. Grant, Carbon 12 (1974) 591.

[36] T. Baird, Carbon 15 (1977) 379.

[37] P.R.S. Jackson, D.L. Trimm, D.J. Young, J. Mater. Sci. 21 (1986) 3125.

[38] A. Sacco Jr, F.W.A.H. Geurts, G.A. Jablonski, S. Lee, R.A. Gately, J. Catal. 119 (1989) 322.

[39] G.A. Jablonski, F.W. Geurts, A. Sacco Jr, R.R. Biederman, Carbon 30 (1992) 87.

[40] D. Mata, M. Ferro, A.J.S. Fernandes, M. Amaral, F.J. Oliveira*et al.*, Carbon 48 (2010) 2839.

[41] N.A. Jarrah, J.G. van Ommen, L. Lefferts, J. Catal. 239 (2006) 460.

[42] S. Pacheco Benito, L. Lefferts, Carbon 48 (2010) 2862.

[43] D. Venegoni, P. Serp, R. Feurer, Y. Kihn, C. Vahlas*et al.*, Carbon 40 (2002) 1799.

[44] H. Neumayer, R. Haubner, Diamond Relat. Mater. 13 (2004) 1191.

[45] K. Bladh, L.K.L. Falk, F. Rohmund, Appl. Phys. A 70 (2000) 317.

[46] L.S. Lobo, D.L. Trimm, J. Catal. 29 (1973) 15.

[47] D. Park, Y.H. Kim, J.K. Lee, Carbon 41 (2003) 1025.

[48] C. Park, R.T.K. Baker, J. Catal. 179 (1998) 361.

[49] P. Pinheiro, M.C. Schouler, P. Gadelle, M. Mermoux, E. Dooryhée, Carbon 38 (2000) 1469.

[50] Z. Yu, D. Chen, B. Tøtdal, T. Zhao, Y. Dai *et al.*, Appl. Catal. A 279 (2005) 223.

[51] C. Singh, M.S.P. Shaffer, A.H. Windle, Carbon 41 (2003) 359.

[52] P. Mcallister, E.E. Wolf, J. Catal. 138 (1992) 129.

[53] J.K. Chinthaginjala, L. Lefferts, Carbon 47 (2009) 3175.

[54] L. Dong, J. Jiao, S. Foxley, D.W. Tuggle, C.L. Mosher *et al.*, J. Nanosci. Nanotechnol. 2 (2002) 155.

[55] H. Zhang, G. Cao, Z. Wang, Y. Yang, Z. Shi, *et al.*, J. Phys. Chem. C 112 (2008) 12706.

[56] D.B. Thakur, R.M. Tiggelaar, J.G.E. Gardeniers, L. Lefferts, K. Seshan, Chem. Eng. J. 160 (2010) 899.

[57] L.F. Albright, J.C. Marek, Ind. Eng. Chem. Res. 27 (1988) 743.

[58] L.F. Albright, C.F. McConnell, K. Welther, Adv. Chem. Series (1979) 175.

[59] T. Hiraoka, T. Yamada, K. Hata, D.N. Futaba, H. Kurachi *et al.*, J. Am. Chem. Soc. 128 (2006) 13338.

[60] Y. Yun, R. Gollapudil, V. Shanov, M.J. Schulz, Z. Dong *et al.*, J. Nanosci. Nanotechnol. 7 (2007) 891.

[61] R.L. Vander Wal, L.J. Hall, Adv. Eng. Mater. 6 (2004) 48.

[62] S. Talapatra, S. Kar, S.K. Pal, R. Vajtai, L. Ci *et al.*, Nat. Nanotechnol. 1 (2006) 112.

[63] L. Gao, A. Peng, Z.Y. Wang, H. Zhang, Z. Shi *et al.*, Solid State Commun. 146 (2008) 380.

[64] A. Genaidy, R. Sequeira, M. Rinder, A. A-Rehim, Sci. Total Environ. 407 (2009) 5825.

[65] C.W. Lam, J.T. James, R. McCluskey, S. Arepalli, R.L. Hunter, Critical Reviews in Toxicology 36 (2006) 189.

[66] W.S. Rasband: ImageJ. http://rsb.info.nih.gov/ij/download.html

[67] H. Li, S. Zhu, H. Xi, R. Wang, Microporous Mesoporous Mater. 89 (2006) 196.

[68] A.I. La Cava, C.A. Bernardo, D.L. Trimm, Carbon 20 (1982) 219.

[69] C.A. Bernardo, L.S. Lobo, J. Catal. 37 (1975) 267.

[70] B.J. Cooper, D.L. Trimm, J. Catal. 62 (1980) 35.

[71] N. Larouche, B.L. Stansfield, Carbon 48 (2010) 620.

[72] Y. Liu, C. Pan, J. Wang, J. Mater. Sci. 39 (2004) 1091.

[73] M.S. Dresselhaus, G. Dresselhaus, R. Saito, A. Jorio, Phys. Rep. 409 (2005) 47.

[74] A. Jorio, M.A. Pimenta, A.G. Souza Filho, R. Saito, G. Dresselhaus *et al.*, New J. Phys. 5 (2003) 139.1.

[75] D.B. Thakur, R.M. Tiggelaar, J.G.E. Gardeniers, L. Lefferts, K. Seshan, Surf. Coat. Technol. 203 (2009) 3435.

[76] Y. Wang, S. Serrano, J.J. Santiago-Avilés, Synthetic Metals 138 (2003) 423.

[77] F. Ohashi, G.Y. Chen, V. Stolojan, S.R.P. Silva, Nanotechnology 19 (2008).

[78] J.L. Figueiredo, D.L. Trimm, J. Catal. 40 (1975) 154.

[79] D. Chen, K.O. Christensen, E. Ochoa-Fernández, Z. Yu, B. Tøtdal*et al.*, J. Catal. 229 (2005) 82.

[80] J.L. Figueiredo, D.L. Trimm, J. Chem. Technol. Biotechnol. 28 (1978) 611.

[81] L.S. Lobo, D.L. Trimm, J.L. Figueiredo, Proceedings of the 5th International Congress on Catalysis 2 (1973) 1125.

Chapter 4

Carbon nanofibers in catalytic membrane microreactors

"All that is necessary for the triumph of evil is that good men do nothing" (Edmun Burke)

Abstract

We report on the fabrication and operation of new hybrid membrane microreactors for gas-liquid-solid (G-L-S) reactions. The presented reactors consist of porous stainless steel tubes onto which carbon nanofibers (CNFs) are grown as catalyst support, all encapsulated by a gas permeable coating. Such reactors benefit from a controlled G-L-S interface of a membrane reactor and high surface area of carbon nanofibers as catalyst support. Preparation steps such as porous stainless steel hollow fiber fabrication, CNF growth on the stainless steel surface, palladium (Pd) catalyst immobilization and an outer gas permeable polymeric coating steps are presented. The fabricated microreactors have high surface area, mechanical strength and catalytic activity for nitrite reduction in water. Results proved high nitrite reduction performance of these reactors, even without the presence of Pd or additional H_2 supply. Our results suggest intrinsic reductant properties and catalytic activity of the reactors, which make them very suitable for hydrogenation reactions.

This chapter is based on the publication: H.C. Aran, S. Pacheco Benito, M.W.J. Luiten-Olieman, S. Er, M. Wessling, L. Lefferts, N. E. Benes, R.G.H. Lammertink. *Journal of Membrane Science*2011, 381 (1-2) 244-250

Chapter 4

4.1 Introduction

Microreactors are miniaturized devices for carrying out chemical reactions, which in recent years have become favorable for chemical technology due to their small dimensions (characteristic length). The high surface to volume ratio in these devices provides them improved heat and mass transfer compared to macro-scale reactors [1-5]. In this chapter we particularly focus on heterogeneously catalyzed gas-liquid-solid (G-L-S) reactions in microreactors. Typical reactor designs applied for these reaction systems are the falling film microreactors [4], dispersed phase microreactors [6], catalyst trap microreactors [7] and mesh microreactors [8-9].

Recently, an alternative membrane reactor design for these reactions in microsystems was demonstrated [3]. In contrast to most of the other designs, in membrane reactors the gas and liquid phases are contacted precisely where the solid catalyst is located. These phases can be independently controlled during the process and the gas-liquid interface is well-defined and stabilized by the membrane [10-12]. In a previous work [3], the contacting of the gas and liquid reactants using a porous ceramic (alumina-Al_2O_3) membrane was performed, which also acts as support for the solid (S) catalyst. The stabilization of the G-L-S interface in the porous Al_2O_3 membrane was obtained by a selective surface modification technique.

The aim of this chapter is to utilize porous metallic materials with carbon nanofibers (CNFs) as catalyst support for a G-L-S reaction process using a membrane reactor concept: porous metallic membrane microreactors (**figure 4.1**). Carbon nanofibers (CNFs) are very promising materials as catalyst support, which is due to their favorable physical and chemical characteristics. CNFs have a high surface area (>100m^2/g) and large pore volumes (>0.5cm^3/g) leading to low tortuosity and efficient internal mass transfer [13-16]. Moreover, CNFs can be strongly attached to the metal substrate, as shown in **chapters 1 and 2** as well as in literature [17-19].

In the reactor concept (**figure 4.1**), the liquid flows in the tube side of the hollow fiber and the contact between the liquid and gas phases takes place on the porous hollow fiber (in microscale) where the CNF catalyst support is located. The outer surface of the porous hollow fiber is covered with a dense gas permeable

polymeric coating in order to stabilize the G-L-S interface. In this concept, the gas is continuously supplied to the reaction zone through the membrane along the whole length of the reactor. The developed reactor is tested for a model multiphase reaction, the catalytic reduction of nitrite ions in water.

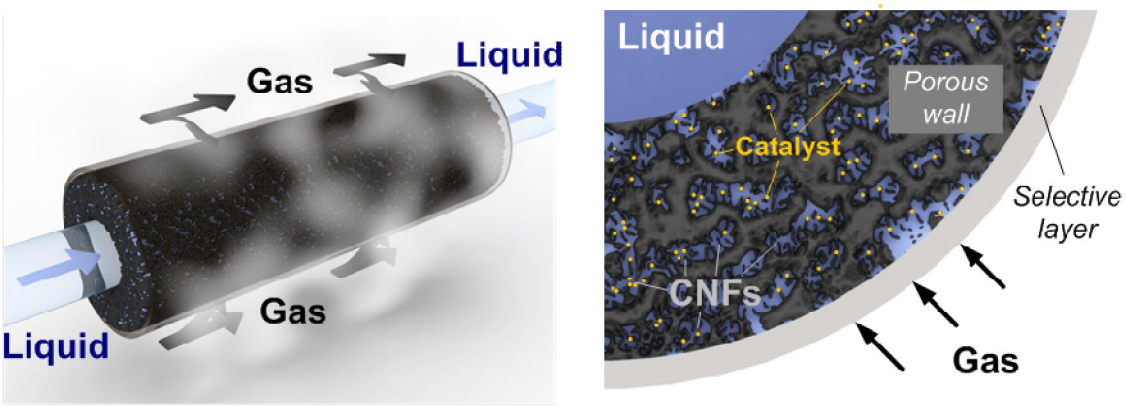

Figure 4.1: *gas-liquid contacting in porous metallic membrane microreactors for multiphase reactions: porous stainless steel membrane decorated with carbon nanofibers (CNFs) as catalyst support. The reactor is encapsulated with a selective, gas permeable PDMS layer*

4.2 Experimental

4.2.1 Materials

Stainless steel powder (316L, Epson Atmix Corporation, D50, with particle size 4,17μm), polyethersulfone (PES; Ultrason, 6020P) and N-methylpyrrolidone (NMP; 99,5%, Aldrich) were used for the stainless steel suspension preparation. PES and the stainless steel powder were dried prior to use. The other chemicals were used without further treatment. Hydrogen, nitrogen (99,999%, Praxair), and ethylene (99,95%, Praxair) were used for CNFs formation without further purification. Palladium (II) 2,4-pentanedione ($Pd(acac)_2$; Alfa Aesar, 34,7%) and toluene (Merck) were used for the catalyst precursor solution. For the PDMS coating a General Electric PDMS RTV 615 kit was used (purchased from Permacol B.V.), which consisted of two components; a vinyl terminated pre-polymer (RTV-A) and a Pt-catalyzed cross-linker (RTV-B). Toluene (Merck) was used as solvent for PDMS.

4.2.2 Reactor preparation

Four different types of samples were prepared: *SS* (porous SS hollow fibers), *SS+CNF* (porous SS hollow fibers with CNFs), *SS+CNF+Pd* (porous SS hollow fibers with CNFs and Pd) and *SSH2* (porous SS hollow fibers with H_2 treatment at 725°C).The preparation steps of the all samples are shown in **figure 4.2**. All the samples were coated with PDMS (gas permeable) on the outer surface before operation in nitrite hydrogenation.

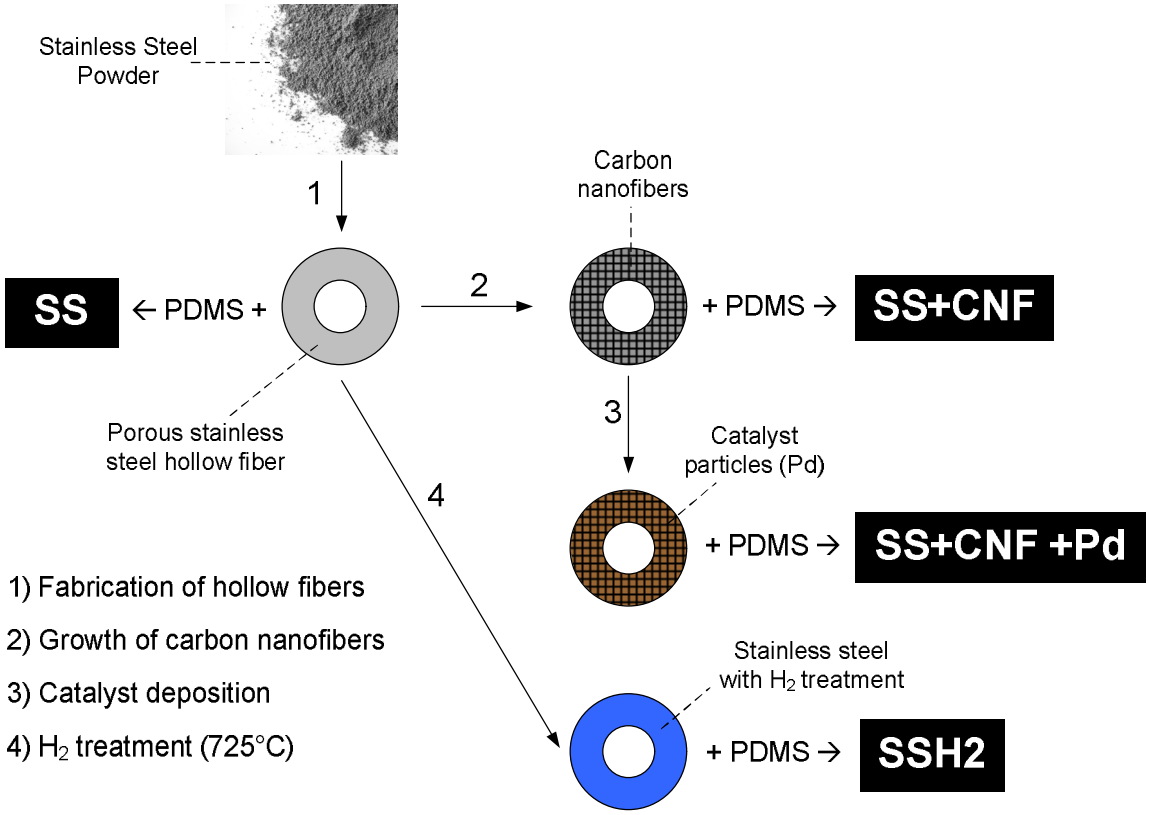

Figure 4.2: *preparation steps of porous metallic membrane microreactors: four samples with various properties (SS, SS+CNF, SS+CNF+Pd and SSH2) are represented in cross-sectional view.*

Fabrication of porous metallic hollow fibers: modified from previous work [20], a stainless steel suspension consisting of 80wt% stainless steel powder, 5wt% PES (binder) and 15wt% NMP (solvent) was prepared. The prepared suspension was pressurized in a stainless steel vessel using nitrogen (2 bars) and pressed through a spinneret with an inner diameter of 0,8mm and an outer diameter of 2,0mm, followed by immersion in a coagulating bath. The air gap was

3cm and de-ionized water was pressed through the bore of the spinneret (7ml/min). The fibers were kept in a water bath for 1 day for removal of the NMP and consequently dried for 1 day. Finally, the samples were sintered at 1100°C for 30min in N_2 atmosphere.

Growth of carbon nanofibers (CNFs): catalytic chemical vapor deposition method was used to grow CNFs on the surfaces of the porous stainless steel hollow fibers. The hollow fibers were placed in an in-house built 12mm inner diameter quartz reactor. Based on results from **chapter 2** and after few optimization tests, the samples were heated up to 725°C (heating rate = 7,5°C/min) in diluted air (9% air and balance N_2). The total flow was always kept at 100ml/min, unless otherwise mentioned. Next, they were treated with hydrogen (100%) for 2h and then in diluted air (9% air and balance N_2) for 1h at the same temperature. Then the temperature in the reactor was decreased to 700°C with N_2. For the growth of the CNFs a gas mixture of hydrogen and ethylene (C_2H_4) in nitrogen was fed to the reactor (25% C_2H_4, 5% H_2 and balance N_2) for 2h with a total flow of 200ml/min. After the growth step, the samples were cooled down to room temperature under N_2 flow. Lastly, an aqueous ultrasound treatment was applied to the samples in order to remove the loose carbon nanofibers from the metal surface, followed by a drying step under vacuum at 100°C overnight.

Catalyst deposition: the porous metallic hollow fiber with carbon nanofibers were immersed in a precursor solution consisting of 300mg $Pd(acac)_2$ in 50ml toluene for 24h. Consequently, the samples were dried overnight at 50°C, calcined for 1h and reduced for 1h at 250°C.

SSH2 sample preparation (H_2 treatment): same procedure was followed as for the growth of carbon nanofibers, where only the final growth step with the carbon source ethylene (C_2H_4) was skipped.

PDMS coating: adapted from Dutczak *et al.* [21], a PDMS/toluene solution was pre-crosslinked before the coating procedure. RTV-A and RTV-B components (3,75wt% in total) of the PDMS kit were dissolved in toluene and kept at 80°C for 2h. Following that, the cross-linking reaction was continued at 60°C until the viscosity of the solution reached approximately 100mPa·s. The viscosity

measurements were carried out at 25°C with a Brookfield DV-II+ Pro viscometer using a spindle nr-61.

The pre-crosslinked PDMS/toluene solution was coated at the outer surface of the hollow fiber using an automated set-up with an immersion/pull up velocity of 0,9cm/s. The hollow fiber samples were dip-coated in the solution with a contact time of approximately 30s, as described in detail elsewhere [21]. The end of the hollow fiber was sealed by glue prior to the coating step. Finally, the coated hollow fibers were placed in an oven at 60°C for 8h to finalize the crosslinking reaction.

4.2.3 Reactor characterization

The cross-sections of the prepared samples were examined by Scanning Electron Microscopy (SEM; JEOL TSM 5600 and LEO 1550 FEG-SEM) and with energy dispersive X-ray analysis (EDX; Thermo Noran Vantage system). The weight increase of the samples before and after the carbon nanofiber growth was determined with an analytical balance. BET measurements were carried out by using the N_2-adsorption isotherm obtained at 77 K (Micromeritics Tristar) to determine the active surface area of the samples. The elemental characterization of the samples was performed by X-ray fluorescence spectroscopy (XRF).

4.2.4 Reactor operation

The prepared reactors were tested for the catalytic reduction of nitrite (NO_2^-) ions in water (**figure 4.3**). The conversion of NO_2^- ions in water and the formation of the reaction product ammonia (NH_4^+) were measured. An aqueous NO_2^- solution with initial concentration 50mg/l was prepared as the liquid reactant and fed to the microreactor (tube side) with a flow rate of 0,1ml/min. Hydrogen (H_2) or Argon (Ar) was fed to the shell side of the reactor module (100ml/min). The NO_2^- and NH_4^+ concentrations at the reactor in- and outlet were measured by an ion chromatograph (Dionex ICS 1000).

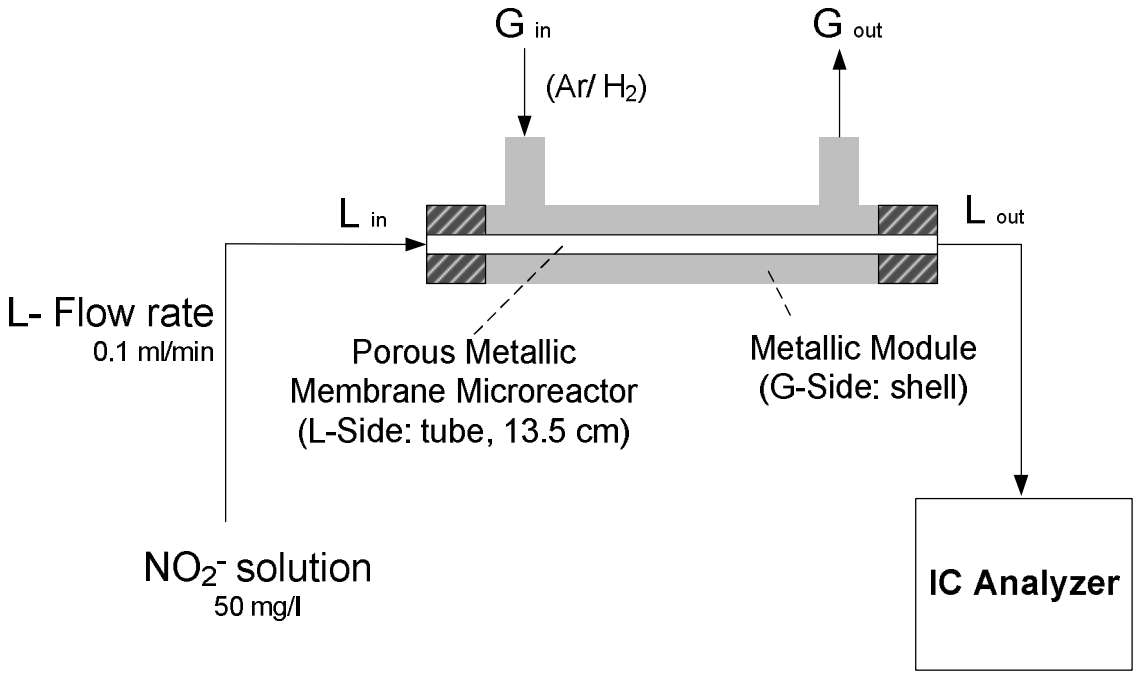

Figure 4.3: *schematic representation of the experimental setup and operational parameters*

4.3 Results and discussion

4.3.1 Reactor characterization

Figure 4.4 shows the cross-section of a sintered porous stainless steel hollow fiber. The hollow fiber has high mechanical strength together with high porosity. The wall of the hollow fiber (**a**) contains thin and long macrovoids. This structure is favorable for the diffusive transport of the NO_2^- reactant (liquid phase) in the porous structure during the operation, so that the immobilized catalyst is easily accessible for the liquid reactant. Furthermore, the outer skin of the hollow fiber (**b**) does not contain macro voids and presents a smoother and denser structure. This is beneficial for applying a thin and defect free PDMS layer in the later stage of reactor preparation. The BET surface area of the porous stainless steel hollow fibers was ~0,4m^2/g.

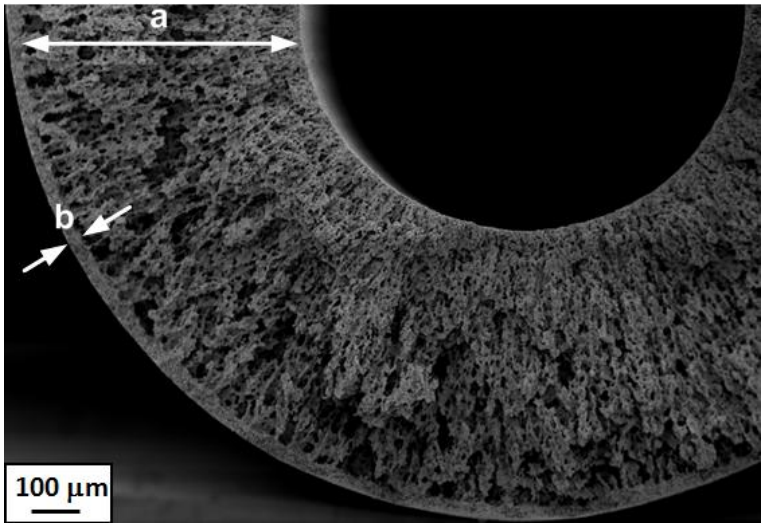

Figure 4.4: *cross-section of a porous stainless steel hollow fiber. a) Wall of the hollow fiber with thin macrovoids; b) outer skin of the hollow fiber with a denser structure*

As can be seen in **figure 4.5**, CNFs grow along the full cross-section of the porous stainless steel hollow fiber. The CNF deposition on the hollow fibers can be identified both visually and by SEM analysis (**figure 4.5**). A clear difference in morphology can be seen between samples with and without CNFs. The weight increase due to the CNF growth was ~16%. The BET surface area of the whole sample after the CNF growth was to ~21,3m^2/g, significantly higher than before the growth. The surface area of only the carbon on the surface was calculated as ~131m^2/g, which is in the same range with values reported in the literature [18, 23-24].

We also observe metal-nano-particles (iron, nickel) on the tip of the grown nanofibers (tip-growth [22]), as can be seen in **figure 4.6a**. The EDX results (not shown here) qualitatively showed carbon content was highest near the outer skin of the sample, which is most likely because the packing density of porous stainless steel was higher at the outer skin compared to the inner wall of the hollow fiber (**figure 4.4**). This may also be caused by the better access of the hydrocarbon source (ethylene gas) to the outer surface of the porous hollow fiber during the CNF growth. The adhesion strength of the carbon nanofibers has been investigated by an aqueous ultrasonic treatment and only a little amount of loose CNFs were released. No considerable weight loss was measured.

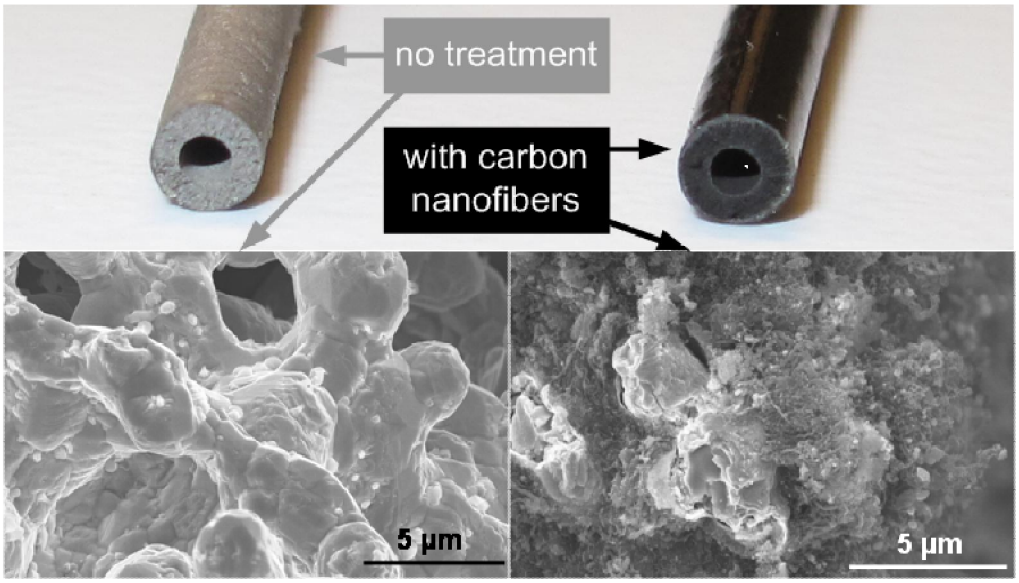

Figure 4.5: *porous stainless steel hollow fibers before (left) and after (right) the growth of the carbon nanofibers.*

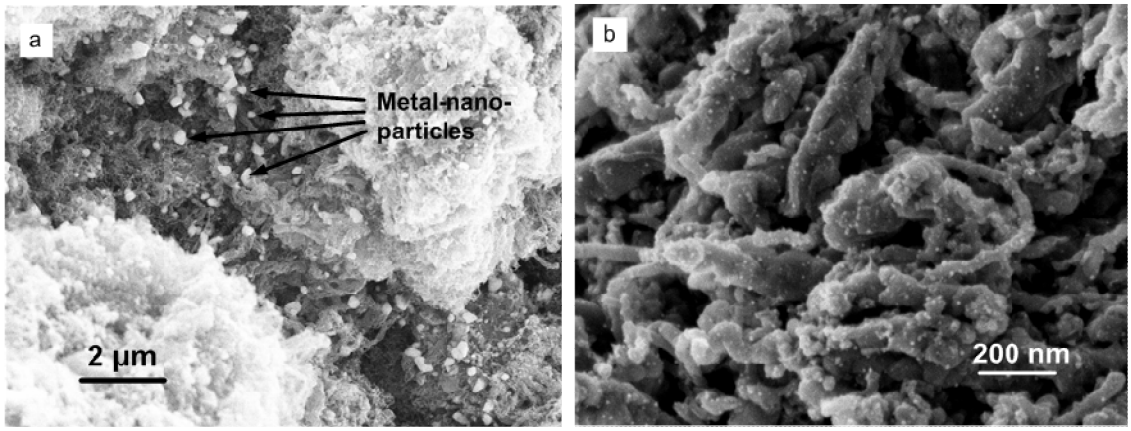

Figure 4.6: *carbon nanofibers grown on the porous stainless steel surface. (a) Metal nano-particles (iron, nickel) on the tip of the grown CNFs; (b) Pd particles immobilized on the surface of CNFs*

After the catalyst immobilization, the average Pd weight percentage on the sample was ~0,1wt% (measured by XRF). The immobilized Pd particles on the CNFs are displayed in **figure 4.6b**. Unfortunately, the Pd distribution along the cross-section of the hollow fiber could not be characterized by the EDX measurements due to the excessive amount of carbon on the stainless steel surface.

Each sample was coated with a selective PDMS layer before the operation. The thickness of the PDMS coating was ~20μm and was able to keep the liquid inside the microchannel at our operation conditions.

4.3.2 Catalytic performance

Catalytic reduction (hydrogenation) of nitrite (NO_2^-) is chosen as a model reaction to test the developed microreactors. Hydrogenation of NO_2^- is known to be a fast reaction that induces mass transfer limitations. In addition, NO_2^- is a harmful compound for human health and removal of NO_2^- ions from water is environmentally relevant due to its increased amount in ground waters. During the catalytic reduction, NO_2^- is converted to nitrogen (N_2) (**eq. 4.1**) and the undesired product ammonia (NH_4^+) (**eq. 4.2**). The Pd-catalyzed hydrogenation of nitrite in the presence of hydrogen gas (H_2) typically takes place as follows [3, 16, 25-26]:

$$2NO_2^- + 3H_2 \xrightarrow{Pd} N_2 + 2OH^- + 2H_2O \qquad \textbf{(eq. 4.1)}$$

$$2NO_2^- + 6H_2 \xrightarrow{Pd} 2NH_4^+ + 4OH^- \qquad \textbf{(eq. 4.2)}$$

In the present study, the conversion of NO_2^- and the formation of NH_4^+ are measured to characterize the performance of our reactors. Our main performance criterion in this model reaction is the NO_2^- conversion. The concentration of NH_4^+ is only measured to confirm the NO_2^- reduction process. **Figure 4.7** shows an overview of the NO_2^- conversion results for the prepared reactors *SS* (stainless steel), *SS+CNF* (stainless steel + carbon nanofibers) and *SS+CNF+Pd* (stainless steel + carbon nanofibers + palladium) with the supply of H_2 as gaseous reactant or argon (Ar) as inert gas to the shell side of the membrane reactor.

Results demonstrate that the reactor *SS+CNF+Pd* shows the highest nitrite reduction performance (**figure 4.7)**. The *SS* reactor shows no considerable activity for the conversion of NO_2^-. On the other hand, with the *SS+CNF* reactor almost 20% of the NO_2^- ions in the initial reaction solution are reduced, even though no Pd catalyst is present in the reactor, which will be discussed later. For the*SS+CNF* and *SS+CNF+Pd* reactors formation of the reaction product ammonia (NH_4^+) was observed. The selectivity values to NH_4^+ under H_2 supply were ~49% (*SS+CNF*) and 67% (*SS+CNF+Pd*). The NH_4^+ production with the *SS* reactor was negligible.

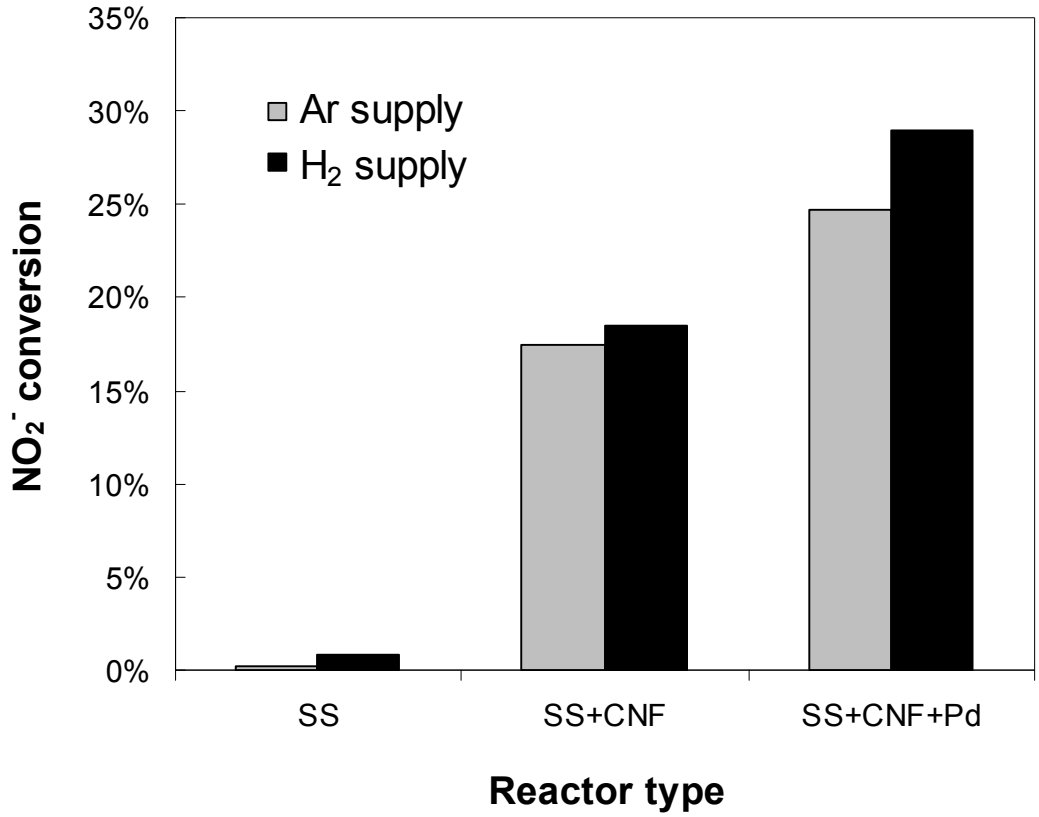

***Figure 4.7**: nitrite reduction performances (liquid flow rate = 0,1ml/min, initial nitrite concentration = 50mg/l) of the prepared microreactors: SS (stainless steel), SS+CNF (SS with carbon nanofibers), SS+CNF+Pd (SS with CNF and palladium catalyst)*

An extraordinary result is that the reaction was also taking place even without the supply of the reactant gas H_2 to the reactor (**figure 4.7**- Ar supply). Both *SS+CNF* and *SS+CNF+Pd* reactors converted significant amounts of NO_2^- and formed NH_4^+. Experiments show that, for the *SS+CNF* reactor, the conversion of NO_2^- and the formation of NH_4^+ are comparable for the experiments with and without H_2 supply. The only considerable contribution of the H_2 supply on the reactor performance is observed for the reactor *SS+CNF+Pd,* which is due to the presence of Pd as hydrogenation catalyst (**figure 4.8**).

Figure 4.8 displays the changes in concentration of NO_2^- and NH_4^+ at the reactor outlet with and without H_2 supply during the operation. At the initial stage of the experiment (**1**), the reaction proceeds under inert argon (Ar) flow in the gas side, resulting in a NO_2^- conversion of ~25%. When the gas phase composition is switched to pure H_2 (**2**), the final NO_2^- concentration decreases indicating a higher

NO_2^- conversion of ~30%. Moreover, the concentration of NH_4^+ increases. At the final stage of the experiment (**3**), when the H_2 gas is substituted again with Ar, the outlet concentrations of NO_2^- and NH_4^+ reach the same values as the initial stage of the experiment.

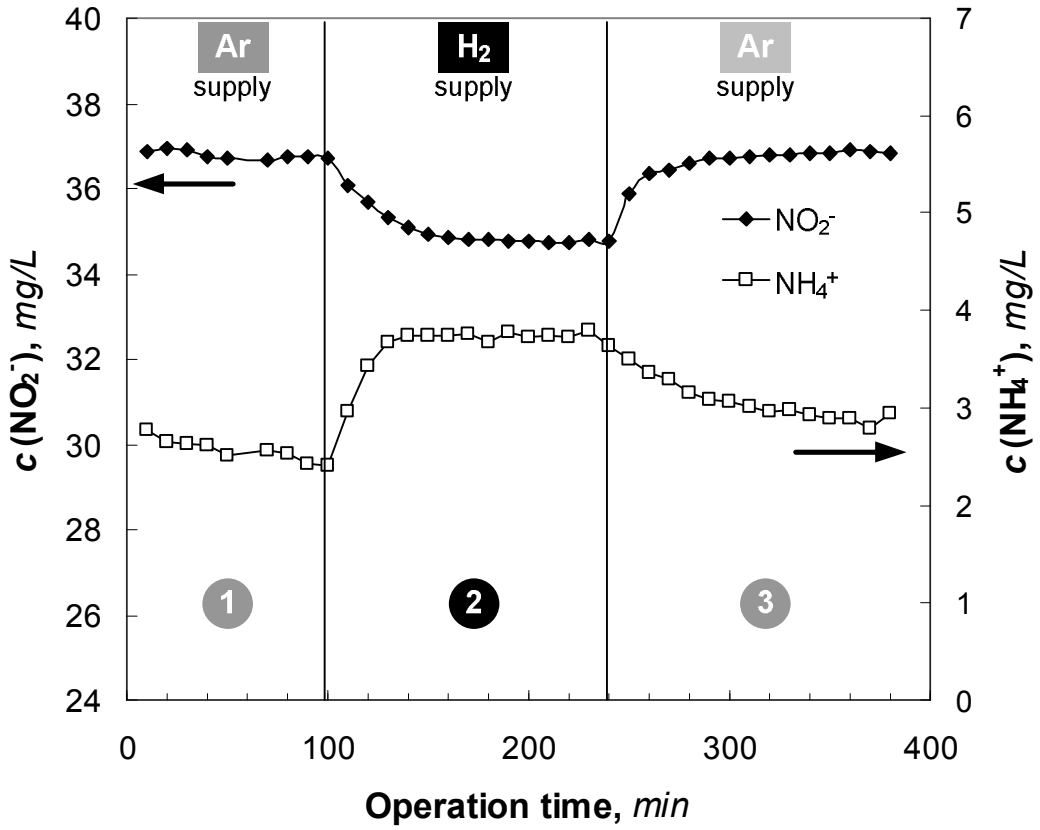

Figure 4.8: *effect of the gas phase composition on the performance of SS+CNF+Pd reactor: c(NO_2^-), c(NH_4^+): concentrations of nitrite (reactant) and ammonia (reaction product) at the reactor outlet. (Liquid flow rate= 0,1ml/min, initial nitrite concentration= 50mg/l)*

In all the reactors, *SS*, *SS+CNF* and *SS+CNF+Pd,* we observe a decrease in the NO_2^- concentration and a simultaneous increase in the NH_4^+ concentration. However, the reactors show significantly different NO_2^- conversion rates (*ξ)*, as *ξ(SS) <<ξ(SS+CNF) <ξ(SS+CNF+Pd)*. Interestingly, the reaction also proceeds in the absence of external hydrogen supply, as shown in **figure 4.7**. Additionally, in the reactor *SS+CNF* no Pd catalyst is present, but the NO_2^- conversion still proceeds drastically, even at lower rates compared to the *SS+CNF+Pd* reactor. The

remarkable performance of our reactors in the absence of hydrogen gas or Pd catalyst is discussed in the next paragraphs.

Firstly, during the growth of CNFs the porous stainless steel fibers were exposed to H_2 gas for more than 1h at elevated temperatures (T≥ 700°C). This method of CNF growth may be responsible for the storage of hydrogen inside the metal bulk of our microreactors. It is well known that some metals and metal alloys, when exposed to hydrogen gas, form metal hydrides and store significant amounts of hydrogen. The formation of the hydrides takes place by adsorption of hydrogen on the metal surface and formation of a solid hydrogen solution phase in the metal, followed by the growth of the metal hydride phase [27-29]. In our case, the stainless steel contains large amounts of Fe, Ni and Cr. The hydrides of these metal mixtures may form as a result of the exposure to hydrogen gas at high temperatures. Later, during the NO_2^- conversion reaction, these metal hydrides may act as an additional source of hydrogen and release their stored hydrogen into the reaction medium. Previous studies show that the metal hydrides act both as a catalyst and as a hydrogen source. Snijder *et al*. [30], in a cyclohexene hydrogenation reaction, observed that the complex metal hydride ($LaNi_{5-x}Al_xH_n$) acted as an additional source of hydrogen.

To understand whether the metal components of our microreactors can act as a source of hydrogen, we prepared the *SSH2* reactor. The *SSH2* reactor, similar to the *SS* reactor, does not contain any CNFs but involves a pretreatment step under hydrogen atmosphere at 725°C. Using the *SSH2* reactor, we performed the NO_2^- conversion experiments with and without an external hydrogen gas source. The observed NO_2^- conversion values were small: 3 and 2%, respectively for the cases with and without external hydrogen supply. Additionally, at the outlet of the *SSH2* reactor a considerable amount of NH_4^+ concentration (up to 0,2mg/l) was observed, which was notably higher than the *SS* reactor that was prepared with no hydrogen pretreatment step. These results support the idea that the storage of atomic hydrogen inside the metal compartments of our microreactors is possible. However, the reactor performance was significantly lower than that of *SS+CNF* reactors. Obviously, the presence of CNFs is crucial for the efficiency of our microreactors.

Secondly, carbon nanofibers (CNFs) and carbon nanotubes (CNTs) are known to store hydrogen via physisorption. Accordingly, the binding energy of hydrogen to these materials is low and hydrogen storage takes place only under specific conditions, such as low temperatures and high hydrogen pressures [31-34]. Since our experiments are performed at room temperature and under low or no hydrogen gas pressure, we assume that the amount of physisorbed hydrogen on the CNFs inside our microreactors is very limited.

Thirdly, the reductive properties of metal particles on the CNFs with high surface area may be responsible for the NO_2^- reduction process. CNFs are known to grow catalytically on metal surfaces, particularly on Fe, Ni and Co [17-19, 22, 35], as shown in **chapter 2**. In this study, the preparation of the porous stainless steel hollow fibers was carried out with 316L powder, consisting of ~67% Fe and ~13% Ni. These metals promote the CNF growth on the porous stainless steel surface with the help of a carbon source, in our case ethylene. Typically, the growth of CNFs occurs by deposition of carbon under these metal growth-catalysts (Fe, Ni). Therefore, the metal particles are squeezed out of the surface and stay at the tip of the fibers (tip growth) [19, 22], also observed in **chapter 2**. Accordingly, in our case, the CNFs do not only support the Pd catalyst, but also contain other metal nanoparticles (Fe, Ni) in an open and available form on their surfaces (**figure 4.6a**), although part of the particles may be encapsulated by carbon.

Among these particles, literature studies show that metallic iron (Fe^0) particles act as a reductant of nitrite (NO_2^-) and nitrate (NO_3^-) ions in water, where an additional supply of hydrogen gas is not present [36-40]. Similarly, Fe particles in their oxidized state (Fe^{2+}) were reported to act as a reducing agent [38-39]. According to Hu *et al*. [37], the NO_2^- reduction process can occur by the direct reduction on Fe^0, or by the indirect reduction with the hydrogen that is generated from the proton reduction reaction of Fe^0. They showed that the reaction takes place much faster in acidic conditions, rather than in neutral or alkaline conditions [37]. In our study, no pH adjustment was carried out. Similarly, Liang *et al.* [36] used nanoscale Fe^0 for the NO_2^- reduction; however, they did not observe a dependence on pH of the initial NO_2^- solutions. They suggested the following reduction mechanism for the nitrite ions in water:

$$3Fe^0 + NO_2^- + 8H^+ \rightarrow 3Fe^{2+} + NH_4^+ + 2H_2O \quad \textbf{(eq. 4.3)}$$

$$3Fe^0 + 2NO_2^- + 8H^+ \rightarrow 3Fe^{2+} + N_2 + 4H_2O \quad \textbf{(eq. 4.4)}$$

$$3Fe^0 + NO_2^- + 6H_2O \rightarrow 3Fe(OH)_2 + NH_4^+ + 2OH^- \quad \textbf{(eq. 4.5)}$$

We observe that the conversion values of our *SS+CNF* microreactor is significantly higher than that of our *SS* microreactor, revealing that the presence of the CNFs is very important in the conversion process. The CNFs do not only increase the surface area, but also increase the availability of metal particles, particularly Fe. The total amount of Fe within the reactors is approximately 12mmol (reactor weight without CNFs = 1g), while the calculated reduction rate of nitrite using the *SS+CNF* reactor is only $2 \cdot 10^{-5}$mmol/min. Evidently, not all of Fe inside our reactors is available for reaction. Still, even if 1% of the Fe in the reactor is available for the nitrite reduction, the reactor can be operated for 100h until this effect will end.

Accordingly, these metal nanoparticles on the tips of the CNFs shall be responsible for the reduction of NO_2^- in our microreactors with H_2 supply, noticeably more than the other factors discussed in here.

4.4 Conclusions

Porous metallic membrane microreactors with carbon nanofibers (CNF) catalyst support were developed and applied for catalytic nitrite (NO_2^-) reduction in water. Porous stainless steel (SS) hollow fibers with high porosity and mechanical strength were fabricated and CNFs with high surface area were successfully grown on the porous SS surface. For particular samples, also palladium (Pd) catalyst was immobilized on the CNFs as a hydrogenation catalyst. Finally, all the reactors were encapsulated with a gas permeable polymeric coating. The fabricated microreactors showed to have a high surface area, mechanical strength and catalytic activity, which was tested for the catalytic reduction of nitrite (NO_2^-) reaction.

The presence of the CNF on the SS surface had a significant effect on the reactor performance. Even without the presence of H_2 and Pd, the NO_2^- ions were successfully reduced, which was confirmed by the disappearance of NO_2^- reactant and formation of ammonia (NH_4^+). These results indicate the reductive properties of the reactor material. We proposed that the reductive properties of iron (Fe) particles, which are located on the tip of the grown CNFs, shall be responsible for the reduction of NO_2^- without hydrogen supply. We also demonstrated that in our Pd-immobilized reactors the NO_2^- reduction proceeds by both catalytic reduction (with Pd and H_2) and reduction by the reactor material itself (*i.e.* by Fe on CNFs). Eventually, the latter effect will exhaust in time and the reaction will still proceed with the immobilized Pd-catalyst on the CNFs and the membrane-assisted supply of H_2.

Therefore, we showed that the porous metallic membrane microreactors decorated with carbon nanofibers are suitable materials for the reduction of nitrite and the reactor design is very promising for the multiphase microreactor technologies.

Acknowledgements

This work was financially supported by Stichting voor de Technische Wetenschappen (STW, Project 07569). This study was originally an idea of the group Soft Matter, Fluidics and Interfaces lead by Prof. Rob Lammertink. I would specially like to thank Can Aran for leading the work included in this chapter and performing the characterization and catalytic tests, apart from fruitful and valuable discussions. I would also like to thank Mieke Luiten-Olieman and Dr. Nieck Benes, from the Inorganic Membranes group of the University of Twente, for the preparation of the sintered stainless steel tubes.

References

[1] A. Gavriilidis, P. Angeli, E. Cao, K.K. Yeong, Y.S.S. Wan, Chem. Eng. Res. Des. 80 (2002) 3.

[2] M.N. Kashid, L. Kiwi-Minsker, Ind. Eng. Chem. Res. 48 (2009) 6465.

[3] H.C. Aran, J.K. Chinthaginjala, R. Groote, T. Roelofs, L. Lefferts*et al.*, Chem. Eng. J. 169 (2011) 239.

[4] V. Hessel, P. Angeli, A. Gavriilidis, H. Löwe, Ind. Eng. Chem. Res. 44 (2005) 9750.

[5] V. Hessel, S. Hardt, H. Löwe, Gas/Liquid Reactions: Sections 5.1–5.3. Wiley-VCH Verlag GmbH & Co. KGaA, 2005.

[6] M.T. Kreutzer, F. Kapteijn, J.A. Moulijn, J.J. Heiszwolf, Chem. Eng. Sci. 60 (2005) 5895.

[7] S. McGovern, G. Harish, C.S. Pai, W. Mansfield, J.A. Taylor, S. Pau, R.S. Besser, Chem. Eng. J. 135 (2008) S229.

[8] R. Abdallah, V. Meille, J. Shaw, D. Wenn, C. de Bellefon, Chem. Comm. (2004) 372.

[9] D.A. Wenn, J.E.A. Shaw, B. Mackenzie, Lab on a Chip 3 (2003) 180.

[10] R. Dittmeyer, K. Svajda, M. Reif, Topics Catal. 29 (2004) 3.

[11] J. Coronas, J. Santamaría, Catal. Today 51 (1999) 377.

[12] M. Vospernik, A. Pintar, G. Bercic, J. Levec, J. Membr. Sci. 223 (2003) 157.

[13] K.P. De Jong, J.W. Geus, Catal. Rev. Sci. Eng. 42 (2000) 481.

[14] N.M. Rodriguez, J. Mater. Res. 8 (1993) 3233.

[15] J.K. Chinthaginjala, K. Seshan, L. Lefferts, Ind. Eng. Chem. Res. 46 (2007) 3968.

[16] J.K. Chinthaginjala, L. Lefferts, Appl. Catal. B: Environmental 101 (2010) 144.

[17] J.K. Chinthaginjala, L. Lefferts, Carbon 47 (2009) 3175.

[18] J.K. Chinthaginjala, D.B. Thakur, K. Seshan, L. Lefferts, Carbon 46 (2008) 1638.

[19] S. Pacheco Benito, L. Lefferts, Carbon 48 (2010) 2862.

[20] M.W.J. Luiten-Olieman, L. Winnubst, A. Nijmeijer, M. Wessling, N.E. Benes, J. Membr. Sci. 370 (2011) 124.

[21] S.M. Dutczak, M.W.J. Luiten-Olieman, H.J. Zwijnenberg, L.A.M. Bolhuis-Versteeg, L. Winnubst *et al.*, J. Membr. Sci. 372 (2011) 182

[22] R.T.K. Baker, M.A. Barber, P.S. Harris, F.S. Feates, R.J. Waite, J. Catal. 26 (1972) 51.

[23] N.A. Jarrah, J.G. van Ommen, L. Lefferts, J. Catal. 239 (2006) 460.

[24] N.M. Rodriguez, M.-S. Kim, R.T.K. Baker, J. Phys. Chem. 98 (1994) 13108.

[25] A. Pintar, G. Berčič, J. Levec, AIChE Journal 44 (1998) 2280.

[26] S.D. Ebbesen, B.L. Mojet, L. Lefferts, J. Catal. 256 (2008) 15.

[27] L. Schlapbach, A. Zuttel, Nature 414 (2001) 353.

[28] S. Er, D. Tiwari, G.A. de Wijs, G. Brocks, Phys. Rev. B 79 (2009) 024105.

[29] S.l. Er, G.A. de Wijs, G. Brocks, J. Phys. Chem. Letters 1 (2010) 1982.

[30] E.D. Snijder, G.F. Versteeg, W.P.M. Van Swaaij, Chem. Eng. Sci. 48 (1993) 2429.

[31] S.K. Bhatia, A.L. Myers, Langmuir 22 (2006) 1688.

[32] S. Banerjee, S. Murad, I.K. Puri, Proceedings of the IEEE 94 (2006) 1806.

[33] S.l. Er, G.A. de Wijs, G. Brocks, J. Phys. Chem. C 113 (2009) 8997.

[34] S.l. Er, G.A. de Wijs, G. Brocks, J. Phys. Chem. C 113 (2009) 18962.

[35] J.K. Chinthaginjala, K. Seshan, L. Lefferts, Ind. Eng. Chem. Res. 46 (2007) 3968.

[36] F. Liang, J. Fan, Y. Guo, M. Fan, J. Wang, H. Yang, Ind. Eng. Chem. Res 47 (2008) 8550.

[37] H.-Y. Hu, N. Goto, K. Fujie, Water Research 35 (2001) 2789.

[38] Y.H. Huang, T.C. Zhang, Chemosphere 64 (2006) 937.

[39] I.F. Cheng, R. Muftikian, Q. Fernando, N. Korte, Chemosphere 35 (1997) 2689.

[40] A. Shukla, J. Pande, A. Bansiwal, P. Osiceanu, R. Biniwale, Catal. Letters 131 (2009) 451.

Chapter 5

Direct growth of CNF layers on carbon microfibers and direct one-side only Pt deposition for PEM fuel cell applications

"Everything should be made as simple as possible, but not simpler" (Albert Einstein)

Abstract

A high surface area carbon nanofiber (CNF) layer was grown from Ni nanoparticles previously deposited on a carbon paper. Subsequently, Pt nanoparticles were deposited directly on the top of the CNF layer by a sputtering method and a chemical method based on the in-situ reduction of Pt with ethylene glycol, named polyol method. Pt nanoparticles are shallower located when sputtered than when deposited by the polyol method. However, the average Pt particle size increases with Pt loading for sputtered samples, whereas the particle size is better controlled by using the polyol method. Moreover, the electrochemical surface area of Pt/CNFs is higher than that of commercial Pt/Vulcan. Samples prepared by the polyol method present higher intrinsic electrocatalytic activity for the oxygen reduction reaction than sputtered samples at similar loadings, and higher activity than Pt/Vulcan at lower loadings. The external oxygen diffusion is higher for the Pt/CNFs, as compared to Pt/Vulcan, due to the specific CNF morphology. However, a deeper location of Pt particles prepared by the polyol method, as compared to Pt/Vulcan, leads to higher oxygen internal diffusion limitations.

This chapter is based on the publication: S. Pacheco Benito, G. Cadafalch Gazquez, M. Duca, G.E.L Merle, J.R.C. Salgado, K. Nijmeijer, M. Koper, L. Lefferts. *Journal of Power Sources* (in preparation)

Chapter 5

5.1 Introduction

Proton exchange membrane fuel cells (PEMFCs) are non-polluting and efficient electrochemical energy conversion devices that are expected to play a dominant role in the energy solutions of the future [1-2]. Hydrogen is introduced in the anode and is oxidized forming protons, which travel through a proton conductive membrane (*e.g*. Nafion®), and electrons, which travel through an external circuit to the cathode where oxygen is reduced to water. The transfer of protons and electrons generates the electricity. However, PEMFCs still need to overcome technological roadblocks such as the high cost of materials, *e.g.* platinum (Pt) used as catalyst, inefficient utilization of Pt particles, water flooding and slow oxygen reduction reaction (ORR) kinetics in the cathode [1]. Currently ca. 0,3-0,4 mg of Pt per cm^2 of electrode are used in the cathode. However, the target is to decrease the Pt loading at least two fold for a viable technology [3].

To achieve higher efficiency and reduce the usage of Pt, nanoparticles are dispersed on an inert support with high surface area, porosity and thermal and electrical conductivity, such as carbon supports [4]. The most used carbon support is carbon black from Vulcan, which, despite the relatively low surface area in comparison with other microporous active carbons, yields better fuel cell performance [5]. However, the still high level of microporosity of Vulcan carbon limits the oxygen transport to the Pt nanoparticles, decreasing the Pt utilization, in comparison with mesoporous carbons [6-8]. Moreover, the decrease of fuel cell performance in long term experiments is related to corrosion of the carbon support during operation, leading to Pt sintering and dissolution, and formation of CO_2 [9-10]. Recently, carbon nanofibers (CNFs) and carbon nanotubes (CNTs) have been suggested as new catalyst supports for fuel cells showing promising results [4, 11-16].

CNFs are graphitic materials with high surface area, low microporosity and high thermal and electrical conductivity [14, 17]. CNFs are mostly used in powder form, as Vulcan carbon, to prepare a catalyst layer for electrodes in fuel cells,*i.e.* depositing a mixture of Nafion and pre-deposited Pt/CNFs on a teflonated carbon gas diffusion layer, or directly on the Nafion membrane [2, 18]. The presence of PTFE on the carbon substrate facilitates the water management in the cell, but it

decreases conductivity and also performance when it degrades during operation [19-21]. Therefore, the presence of a hydrophobic CNF layer [22-24], as will be shown in **chapter 6**, could decrease or eliminate the need for PTFE. To avoid the synthesis and purification of loose CNF powder, which will eventually end up in the carbon substrate, and increase electrical contact, the direct growth of a CNF layer on the carbon substrate has been suggested [25-30]. Pt nanoparticles must be located in close proximity to the central membrane that separates the anode and the cathode [2, 31-32]. Currently used methods to deposit Pt particles directly on a porous carbon substrate, such as wet impregnation or electro-deposition [26, 33-43], do not allow an optimal control of both the Pt location and particle size. Therefore, the direct synthesis of tunable Pt loadings on only one side of the CNF layer with controlled Pt particle size remains a challenge.

To overcome this, here we propose the direct synthesis of CNF layers on a carbon paper substrate followed by the deposition of Pt nanoparticles by physical and chemical methods (**figure 5.1**). The goal is the synthesis of a Pt/CNF layer directly on a carbon paper with low Pt loadings and high potential for the use in fuel cells. We report the preparation and the characteristics of the CNF and Pt layer, as well as the influence of the Pt loading on the particle size. Moreover, we report the electrochemical characterization of the electrodes and the oxygen reduction reaction (ORR) performance in comparison with commercial Pt deposited on Vulcan carbon.

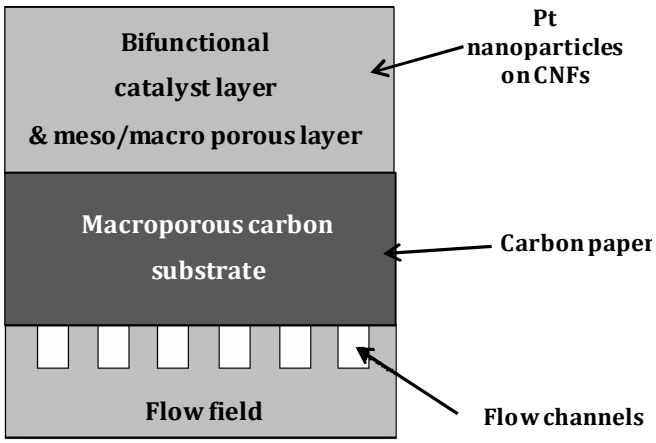

Figure 5.1: *proposed concept of electrodes for PEMFCs based on the direct growth of a CNF layer on a carbon paper and subsequent Pt deposition*

5.2 Experimental

5.2.1 Materials

Non-hydrophobized Toray TGP H-060 carbon paper of 140 μm thick was used. Samples of 32 mm in diameter were cut from the as-received sheets. $H_2PtCl_6 \cdot H_2O$ (99,999%) and ethylene glycol (>99%) were supplied by Sigma-Aldrich. $Ni(NO_3)_2 \cdot 6H_2O$ (>99%) and pure ethanol were supplied by Merck. Solutions of 0,5M H_2SO_4 was prepared by diluting concentrated H_2SO_4 supplied by Merck. Hydrogen, nitrogen and air (99,999%, Praxair), and ethylene (99,95%, Praxair) were used for pretreatment and CNF formation without further purification. Water was deionized using a Millipore Synergy equipment before usage.

5.2.2 Nickel deposition

Ni particles were deposited on the carbon substrate by wet impregnation using a metal precursor salt. 15 mg of $Ni(NO_3)_2 \cdot 6H_2O$ was dissolved in 5 ml ethanol and the solution was heated to 50°C. Afterwards, the solution was sprayed on one side of a heated carbon paper at 50°C using a Badger 200 airbrush using N_2 at 0,5 bar.

5.2.3 Carbon nanofiber growth

Samples were placed in an in-house built quartz reactor of 32 mm inner diameter for the CNF growth by catalytic chemical vapor deposition. The pretreatment and CNF growth parameters were adjusted based on the results shown in the **chapter 3** that lead to good attachment [44]. The total flow of the gases was permanently kept constant to 100ml/min. Samples impregnated with Ni particles were subjected to a pretreatment as follows. First, the temperature was raised from room temperature to 500°C at a rate of 7,5°C/min in a mixture of N_2 and H_2 (20% v/v) and the temperature was kept for 15 min. Second, a mixture of N_2 and Air (10% v/v) was introduced for 15min. Pure N_2 was flushed for 5 min before introducing air to avoid direct contact between H_2 and O_2 from the air. The temperature was adjusted to 450°C in N_2 and a mixture of H_2 (5% v/v) and C_2H_4 (25% v/v) in balance N_2 was fed for 60 minutes. Finally, ethylene and hydrogen gas streams were shut off and the system was cooled down to room temperature under 100ml/min of N_2 at a rate of 10°C/min.

5.2.4 Pt deposition

Pt nanoparticles were deposited by two different methods: sputtering and *in-situ* chemical reduction method. For the first method, a JEOL JFC-1300 Autofine Pt coater equipment was used to sputter the samples at 10mA and 0,5bar of argon. The sputtering time was 60, 120 or 240s. The second method involves *in-situ* formation of Pt nanoparticles by a solution of ethylene glycol, here termed the polyol method, modified from those reported in literature [45-47]. 1, 5 or 10mg of $H_2PtCl_6 \cdot H_2O$ were dissolved in 0,5, 2,5 or 5,0ml of ethylene glycol respectively, the pH was adjusted to 7, and 10ml of ethanol were added. The solution was then heated under reflux to 150°C for ca. 30min and then sprayed on the carbon substrate using a Badger 200 airbrush, on the side of the CNF layer. Afterwards, the samples were washed with water to remove any excess of ethylene glycol or non-adsorbed Pt species.

The electrode for comparison of the results was prepared from a commercial 60% Pt/Vulcan XC-72 from E-TEK (Pt/Vulcan will be used hereafter). An ink of the catalyst in ethanol was directly sprayed on the carbon paper until the loading was ca. 0,4mg/cm^2.

5.2.5 Characterization

The weight of the CNF layer was determined using a Metler Toledo AE163 balance with precision up to 0,01mg. The low resolution morphology and cross sections of the carbon layers were studied using a scanning electron microscope (SEM) JEOL 6250LV. Top and cross section morphology of CNFs were examined with a high resolution LEO 1550 FEG SEM, in combination with energy dispersive X-ray (EDX) elemental mapping. Cross sections were obtained by cutting the samples with a pair of scissors after immersing shortly in liquid N_2. A Phillips CM300ST-FEG transmission electron microscope (TEM) was used to estimate the size of the Pt particles, after scratching gently the top of the sample and dispersing the carbon in ethanol. The average Ni and Pt nanoparticle sizes were calculated from measurements on 100 individual particles on different SEM and TEM pictures, respectively, using the freeware ImageJ [48]. The surface area of the CNFs was calculated by the BET method in a Micromeritics Tristar equipment after degassing the samples overnight at 300°C in flushing N_2.

The Pt loading of the samples was determined by Panalytical PW 1480 X-ray fluorescence (XRF) equipment, without destroying the samples. The Pt L-alpha line was measured with the LIF200 crystal 60kV, 40mV and the Pt M-alpha line with the PE crystal 50kV, 50mV. The loadings were calculated from the measurements with Panalytical software SuperQ with IQ+ module for the L-line and the XRFSMPLX method described by Bos and Vrielink [49] for the M-line. The software Superq with FP-Multi module was used for estimating the depth of information for the Pt L- and M-line, taking into account the composition, weight and area of the sample.

Cyclic voltammetry and linear sweep voltammetry of the samples were performed in a three electrode system in 0,5M H_2SO_4. The potential was controlled with an Autolab 302N potentiostat. Samples of 12mm in diameter were used in all cases. A Pt wire was used as a counter electrode and an Ag/AgCl electrode was used as reference. Cyclic voltammetry was acquired from -0,25V to 1V *vs* Ag/AgCl after bubbling N_2. ORR linear sweep voltammograms were acquired by pre-saturating the solution with pure oxygen and scanning from 0,85V to 0,45V *vs* Ag/AgCl. Rotating disk electrode (RDE) experiments were carried out with a Motomatic rotor using 0,5M H_2SO_4 as electrolyte. The sample was attached to a glassy carbon (GC) disk electrode (5mm in diameter) by means of two gold wires. Prior to the experiment, the GC was polished and thoroughly rinsed with ultra-pure water. The potential was controlled with an Autolab 12 potentiostat. A Pt wire and a reversible hydrogen electrode (RHE) were used as counter and reference electrode, respectively. Although the ORR currents measure is negative, we will refer to them by their magnitude.

5.3 Results and discussion

5.3.1 Growth of CNF layer on carbon paper

Figure 5.2a shows the as-received carbon microfibers of the carbon paper with a typical diameter of 10μm. **Figure 5.2b** shows small Ni nanoparticles, with an average size of 35±15nm, deposited on a carbon microfiber after the heat pretreatment. Ni particles are distributed all over the surface of the fibers, although certain parts contain more and larger particles (**figure 5.2b**). **Figure 5.2c** shows the top view of the resulting CNFs covering the entire surface the carbon

paper and closing the existing macrovoids. The typical carbon yield, as a result of the CNF growth, is ca. 20mg per sample. The resulting samples (32mm in diameter) were treated with a flow of 120l/min of air parallel to the samples and only 1-2% of CNFs were detached. The cross section of the sample (**figure 5.2d**) shows that the CNF layer grows only on one side of the carbon paper (~80μm), therefore leaving the other side with only naked microfibers. CNFs have a typical diameter of 50nm and a BET surface area of 256m^2/g, similar to Vulcan [50-51].

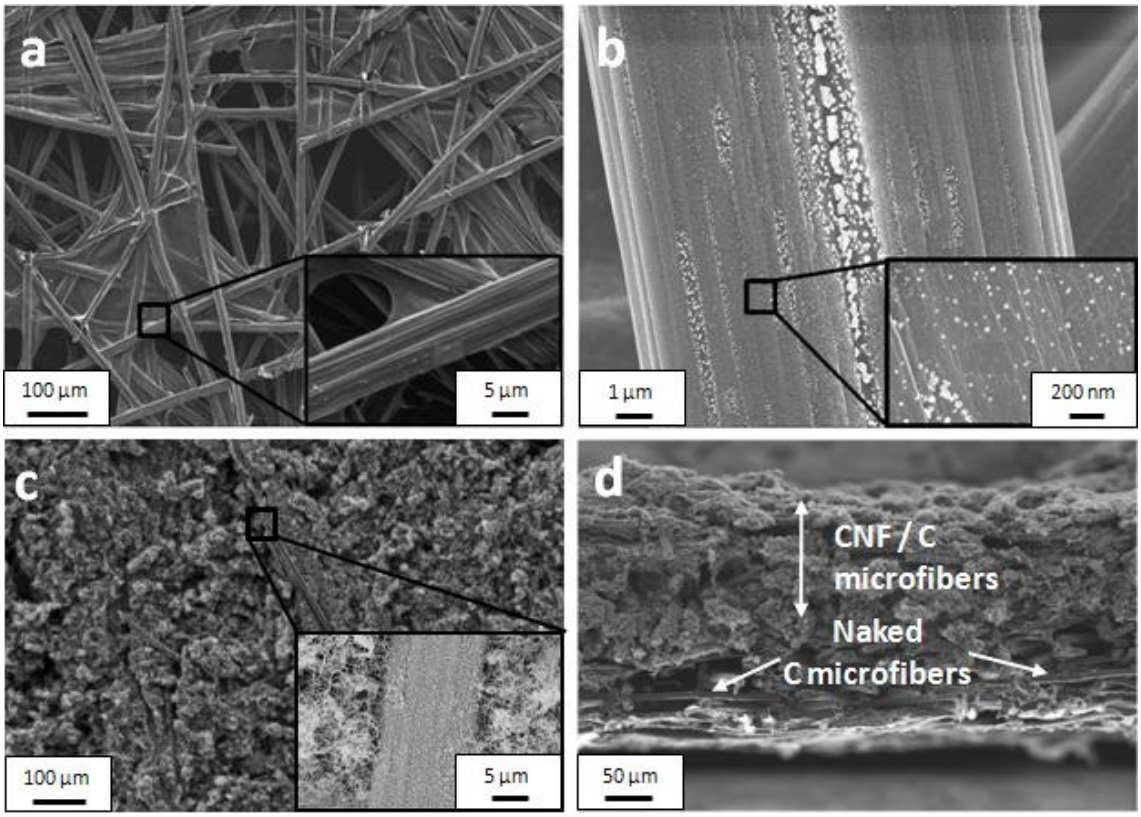

Figure 5.2: *a) As-received carbon microfibers; b) Ni nanoparticles deposited on the carbon microfibers; c) CNFs grown on top of the carbon microfibers; d) cross section of a representative ~ 80μm thick CNF / C microfiber composite and naked ~ 100μm C microfibers*

5.3.2 Pt nanoparticles deposition

By varying the sputtering time, different Pt loadings are obtained: 0,024, 0,049 and 0,078 mg Pt/cm^2 after 60, 120 and 240s respectively. On the other hand, loadings of 0,023, 0,14 and 0,31mg Pt/cm^2 are obtained by varying the amount of Pt precursor to 1, 5 or 10mg, respectively, using the polyol method. **Figure 5.3**

shows the morphological SEM pictures of representative most superficial CNFs with Pt particles (white spots) deposited using sputtering (**figures 5.3a and 5.3b**) and the polyol method (**figures 5.3c and 5.3d**). In all cases the particles are homogenously deposited on the CNFs, however, the concentration of Pt particles on the surface obtained with sputtering is higher than that obtained with the polyol method for similar or even lower Pt loadings (**figures 5.3a and 5.3c**).

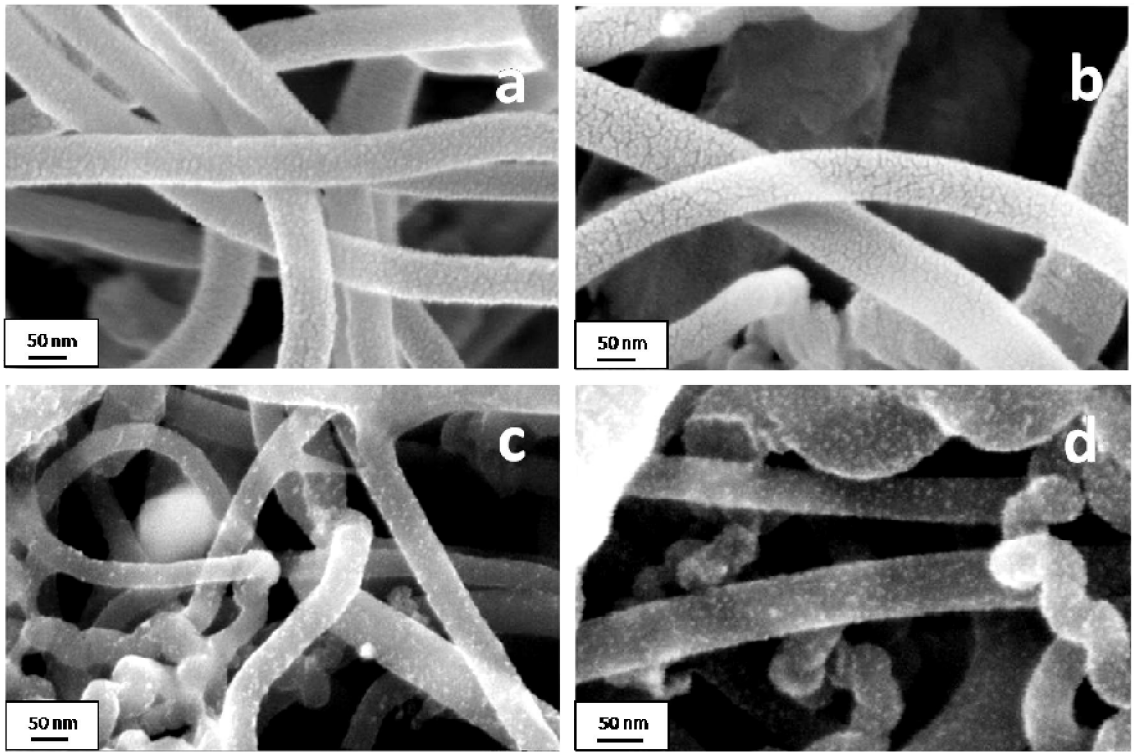

Figure 5.3: *representative high resolution SEM images of the Pt nanoparticles deposited by sputtering with a) 0,024 and b) 0,078mg Pt/cm² and by the polyol method with c) 0,023 and d) 0,31mg Pt/cm².*

5.3.3 Pt particle size

Figure 5.4 shows representative high resolution TEM images of the Pt nanoparticles deposited by sputtering (**figure 5.4a**) and the polyol (**figure 5.4b**) methods. It is clear that Pt nanoparticles are more densely concentrated at the sputtered samples than at the samples subjected to the polyol method for similar or even lower loadings.

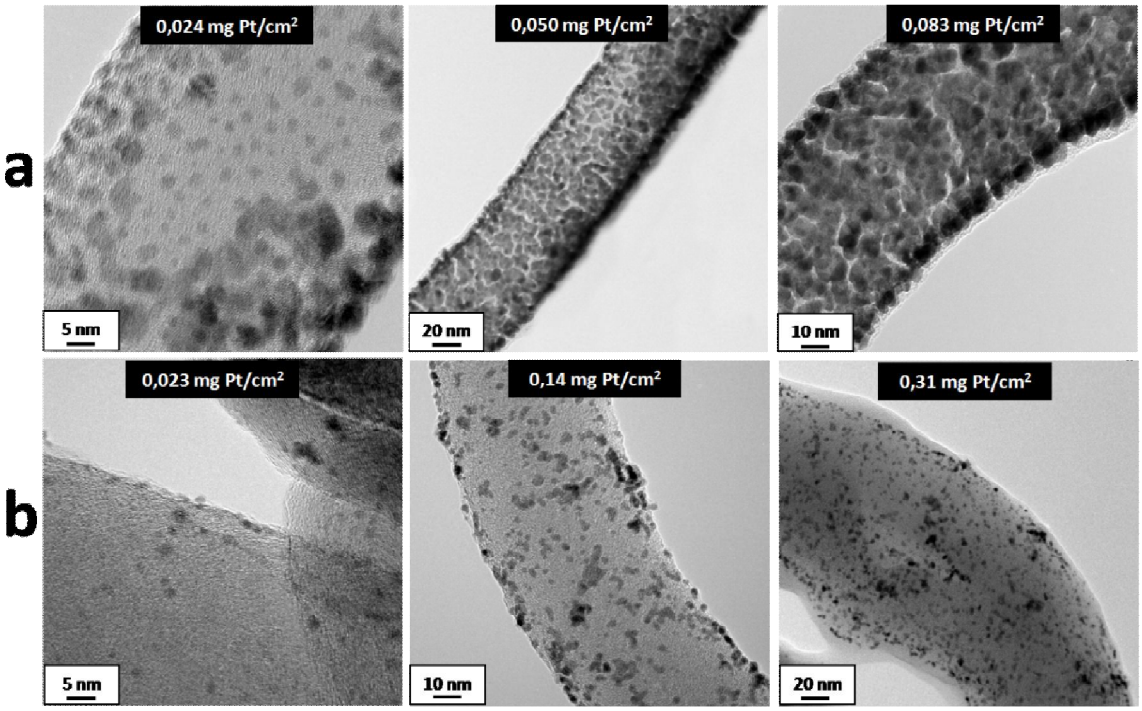

Figure 5.4: *TEM images of platinum nanoparticles deposited on CNFs for different loadings prepared by a) sputtering and b) polyol method*

Figure 5.5 shows the particle size distribution for the different Pt loadings for both methods. It is clear that the particle size and size distribution increase with Pt loading when sputtering is used (**figure 5.5a**), in agreement with literature [52-53]. It is known that at higher loadings, sputtered samples start developing a continuous Pt layer [52, 54-55]. In contrast, the average Pt particle size remains more or less constant, between 3,0 and 3,3nm, when the polyol method is used (**figure 5.5b**), independent of the Pt loading. These values are in fair agreement with values of ca. 3nm reported in literature when the polyol method was used *ex-situ* to deposit Pt on CNFs [56-58]. Moreover, the size distribution is narrower for particles deposited by using the polyol method as compared to sputtering. Therefore, control of the Pt particle size on a CNF layer is more easily obtained using the polyol as compared to sputtering.

Unfortunately, the Pt particle size of Pt/CNFs samples could not be determined by XRD line broadening because the Pt loading appeared too low.

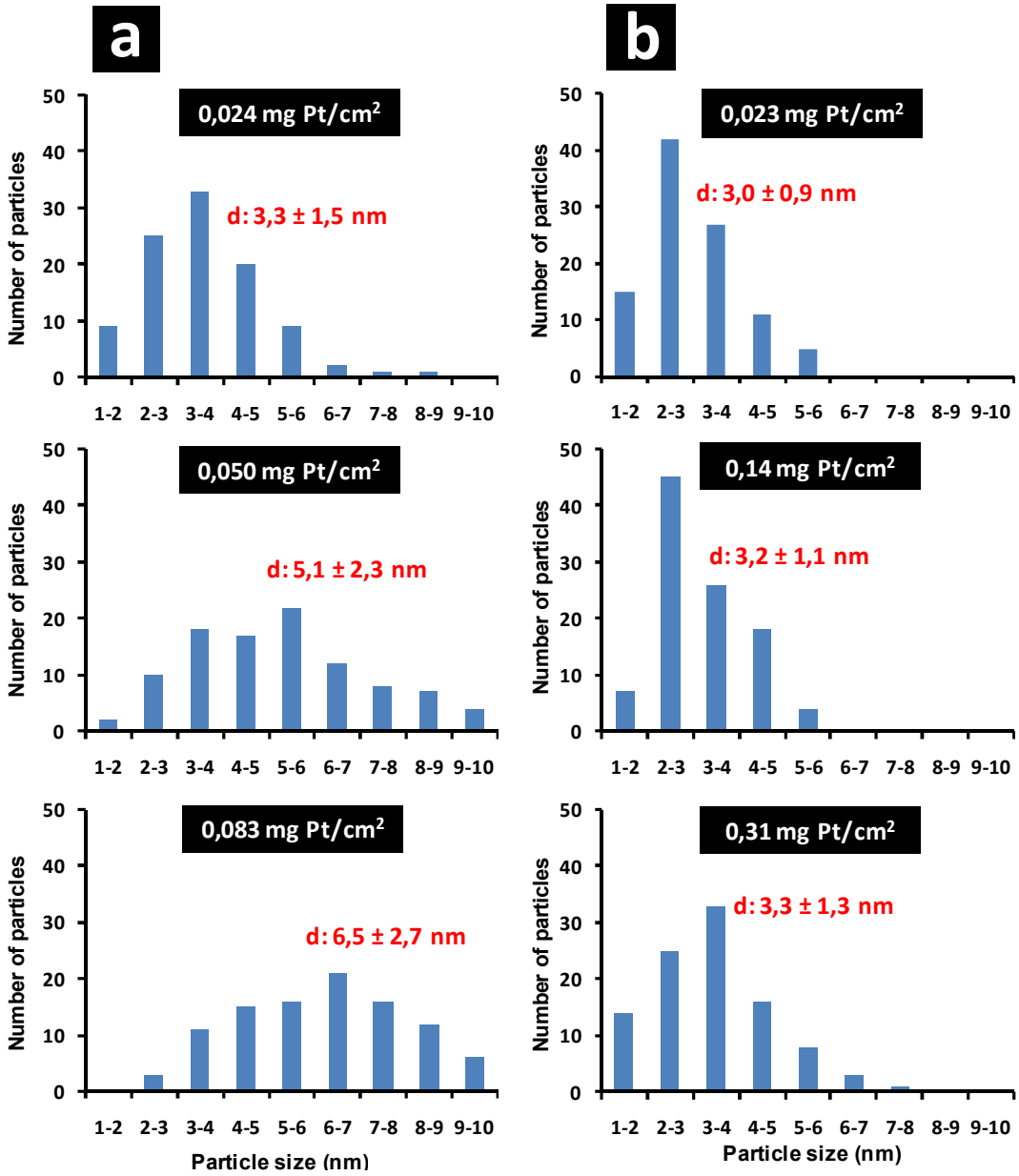

Figure 5.5: *platinum particle size distribution for different loadings prepared by a) sputtering; b) polyol method*

5.3.4 Pt location

Figure 5.6 shows the XRF spectra of the Pt L- and M-line for a sample with sputtered Pt and a sample with Pt deposited *via* the polyol method. The concentration of Pt seems lower for both samples when calculated from the Pt L-line than when calculated from the M-line. Similar results were obtained for all other samples (not shown). The information depth of the L-line is estimated to be much higher than the total thickness of the sample (ca. 180µm), whereas the depth

of information for the M-line is approximately 60µm. Therefore, the Pt concentration obtained from the L-line is used to calculate the Pt loading (in mg/cm²) of the samples, taking into account the weight and geometrical area of the samples. On the other hand, the seemingly higher Pt concentrations as calculated from the M-line reveal that Pt particles are located asymmetrically at one side of the carbon paper. This is confirmed when the samples are turned upside down, as no Pt is detected with the M-line in that case, whereas the Pt loading according to the L-line remained unchanged (not shown).

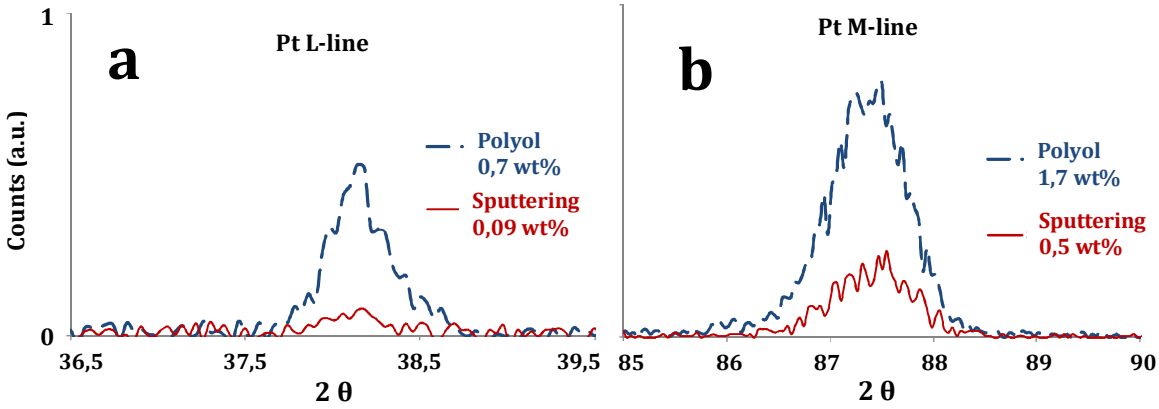

Figure 5.6: *XRF spectra of a sputtered sample with 0,024mg Pt/cm² and a sample prepared by the polyol method with 0,14mg Pt/cm²; a) Pt L-line and b) Pt M-line. The Pt loadings (in wt%) calculated from each line are indicated in the graphs*

Figure 5.7 shows the Pt signals for SEM cross sections of a sputtered sample with 0,024mg Pt/cm², samples prepared using the polyol method with 0,023 and 0,31mg Pt/cm², and a sample with commercial Pt/Vulcan with 0,38mg Pt/cm². It is clear that in all samples, the Pt nanoparticles are mostly located at the top part of the sample. However, Pt particles prepared by sputtering with 0,023mg Pt/cm² are located mostly in the first 5µm (**figure 5.7a**), in agreement with other studies on sputtered Pt in literature [55, 59]. The catalyst layer with commercial Pt/Vulcan as prepared in the present work has a Pt penetration of ca. 10µm (**figure 5.7d**). On the other hand, using the polyol method, the layer containing Pt is ca. 20µm thick (**figures 5.7b and 5.7c**), although this is less clear for the sample with lower loading (**figure 5.7b**). Nevertheless, it is clear that sputtered and Pt/Vulcan samples contain Pt closer to the surface as compared to the polyol based samples with respectively similar Pt loading.

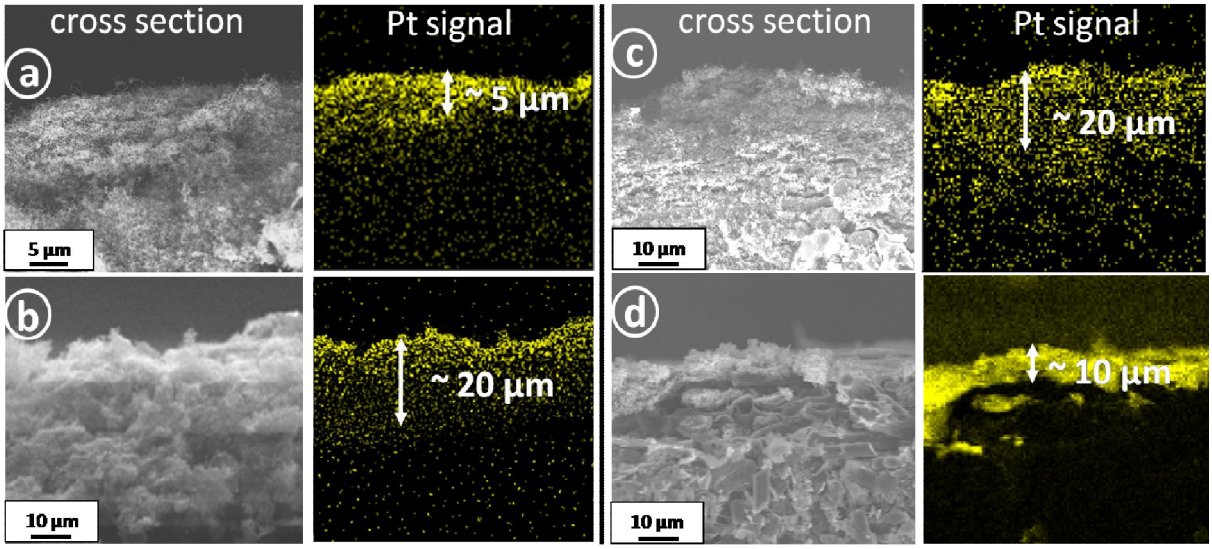

Figure 5.7: *cross section SEM images and EDX signals of Pt for samples prepared by a) sputtering 0,024 mg Pt/cm²; b) polyol 0,023 mg Pt/cm²; c) polyol; 0,31 mg Pt/cm²; d) Pt/Vulcan; 0,38 mg Pt/cm²*

5.3.5 Cyclic voltammetry

Figure 5.8 shows the cyclic voltammograms of samples prepared by the polyol and sputtering methods. Data of a blank sample (only CNFs, **figure 5.8a**) and those of the commercial Pt/Vulcan (**figure 5.8b**) are also shown. For all Pt containing samples we observe the typical hydrogen and oxygen adsorption and desorption peaks, similar to polycrystalline Pt [60]. **Figure 5.8a** shows the cyclic voltammograms of samples prepared by the polyol and sputtering methods with similar loadings and Pt particle size (**figure 5.5**). The blank sample does not show any characteristic peak (**figure 5.8a**), confirming that the deposited Pt nanoparticles are responsible for the peaks of the cyclic voltammograms. **Figure 5.8b** shows the cyclic voltammograms of a sample prepared by the polyol method with 0,31mg Pt/cm^2 and a sample prepared with commercial Pt/Vulcan with 0,38mg Pt/cm^2. The polyol sample shows higher current densities than the Pt/Vulcan sample. Moreover, the samples of Pt deposited on CNFs show a higher double layer capacitance (in the region ~0,1-0,3V *vs* Ag/AgCl) as compared to Pt/Vulcan, in agreement with literature [61], especially for sputtered samples (**figure 5.8a**). A high capacitance is typically associated with high surface area and highly rough carbon surfaces [30].

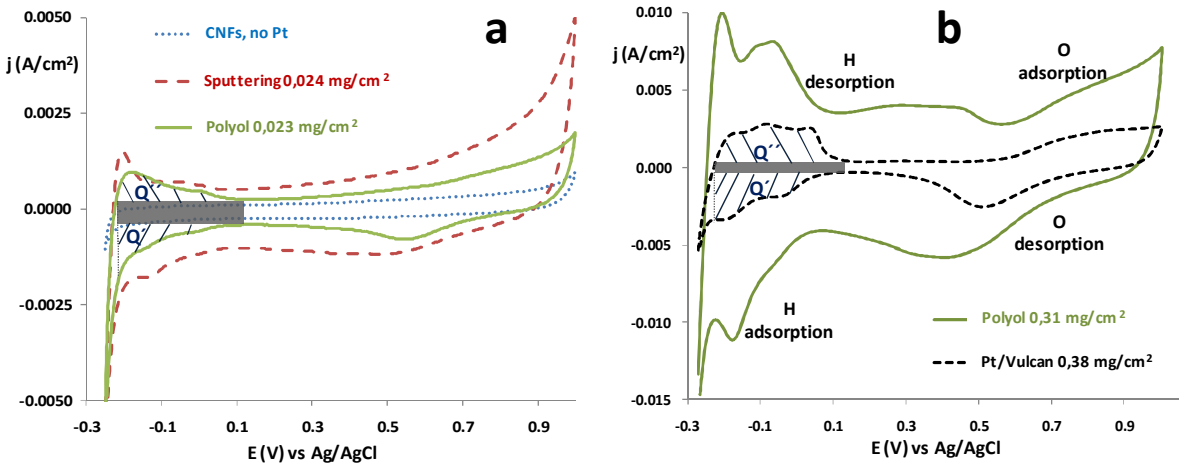

Figure 5.8: *cyclic voltammograms (3rd scan) in 0,5M H_2SO_4 at 20mV/s of a) samples with similar loadings and different preparation methods, including a blank; b) sample prepared by the polyol method and commercial Pt/Vulcan*

The electrochemical surface area of Pt (ECSA) was calculated from the adsorption and desorption peaks of hydrogen for all the samples (**eq. 5.1**) after removing the double layer contribution and assuming that the charge of mono-layer hydrogen adsorption on a polycrystalline Pt surface (H:Pt = 1:1) is 210μC/cm² [62].

$$ECSA\ (m^2/\ g\ Pt) = \frac{100\ \frac{Q´+Q´´}{2}}{0,21\ l} \qquad \textbf{(eq. 5.1)}$$

where $Q´$ is the charge associated with the adsorption of hydrogen, $Q´´$ is charge associated with the desorption of hydrogen, and l is the Pt loading (mg Pt/cm²).

The surface area (SA) of Pt can also be estimated from TEM data according to **eq. 5.2** assuming spherical Pt nanoparticles [42]:

$$SA\ (m^2/\ g\ Pt) = 0,01 \sum \frac{6000\ N_i}{\rho d_i} \qquad \textbf{(eq. 5.2)}$$

where ρ is the density of Pt (21,4g/cm³) and N_i is the percentage of particles having a size d_i (as determined with TEM).

Table 5.1 shows the calculated values for the ECSA and SA of Pt for all samples. It is clear that samples with Pt deposited on CNFs show higher ECSA and SA than commercial Pt/Vulcan. This is probably due to a higher average Pt particle size for Pt/Vulcan, which is 4,1nm according to XRD (not shown) and in agreement with literature [63], as compared to samples with CNFs having an average Pt particle size in the range of 3,0-3,3nm (**figure 5.5**). We observe that the ECSA and the SA are in good agreement for all Pt/CNFs samples, but they disagree significantly for the Pt/Vulcan sample. This might be due to a relatively broad Pt particle size distribution in the Pt/Vulcan sample. Moreover, the existence of inaccessible Pt particles due to micropores of the Vulcan carbon can possibly also limit the contribution of Pt particles to the adsorption and desorption of hydrogen, therefore leading to Pt with a less electroactive area [6, 64].

Table 5.1: *Pt electrochemical surface area (ECSA) and surface area (SA) of Pt for samples prepared by different methods and with different Pt loadings*

	Sputtering 0,024	***Polyol 0,023***	***Polyol 0,31***	***Pt/Vulcan 0,38***
ECSA (m^2/g Pt)	***98 ± 11***	***95 ± 8***	***86 ± 7***	***34 ± 9***
SA (m^2/g Pt)	***97 ± 9[a]***	***98 ± 6[a]***	***91 ± 8[a]***	***68[b]***

[a] Estimated from TEM values

[b] Estimated from XRD peak broadening

5.3.6 Oxygen reduction reaction (ORR): stationary electrode

Figures 5.9a and 5.9b show the linear sweep voltammograms, normalized per geometrical area and per mass of Pt respectively, of the oxygen reduction reaction (ORR) of samples prepared by sputtering and the polyol method, as well as the commercial Pt/Vulcan. In all cases, the absolute current density values increase as the voltage decreases following three different regions. The first region is mainly controlled by kinetics. Second, there is a steep region where both kinetics and diffusion control the process. Third, there is a more or less flat region which is mainly controlled by diffusion, corresponding to the depletion of oxygen in the diffusion layer adjacent to the Pt active sites.

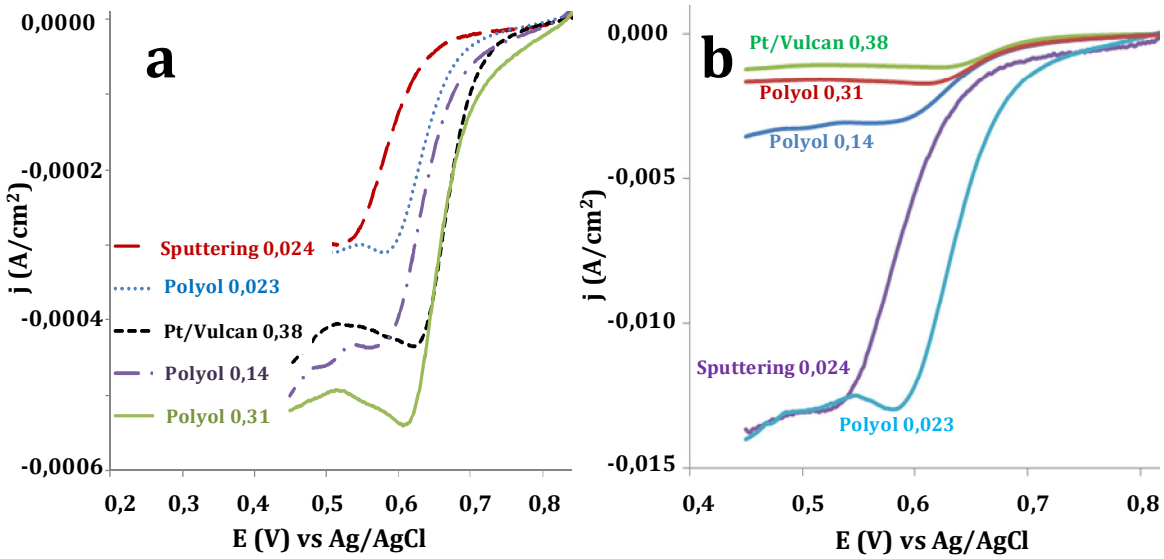

Figure 5.9: *linear sweep voltammograms at 1mV/s of samples prepared by sputtering and polyol methods with different loadings, and commercial Pt/Vulcan, in 0,5M H_2SO_4 saturated with O_2. Current normalized per a) geometrical area and b) mass of Pt*

Figure 5.9a shows that sputtered and polyol samples with similar loadings, 0,024 and 0,023mg Pt/cm^2 respectively, lead to similar diffusion limiting currents although the Pt particles are located deeper for samples prepared by the polyol method as compared to the sputtered sample (**figures 5.7a and 5.7b**). Since the diffusion lengths are different, this indicates that Pt/CNF samples do not suffer from internal diffusion limitations at these Pt loadings. The shift of the curve to the right observed for the sample prepared by the polyol method, as compared to the sputtered sample with similar Pt loading (**figure 5.9a**), indicates that polyol samples are intrinsically more active than sputtered samples. Differences in the preparation procedure and the relatively broad Pt size distribution of the sputtered sample (**figure 5.5**) might contribute to this effect.

Figure 5.9a shows that the diffusion limiting current increases with Pt loading for samples prepared by the polyol method. This indicates that the external diffusion is not limiting for samples prepared by the polyol method. However, when the current is normalized per mass of Pt, the diffusion limiting current increases with a decrease of the loading (**figure 5.9b**). This suggests that at relatively high loadings the process is under internal diffusion control. This is in agreement with other studies on Pt/Vulcan [65] or Pt/CNTs [66] that report an

increase of internal diffusion limitations for increasing Pt loading. However, at low Pt loadings the process is under kinetic control since there are not external or internal diffusion limitations, as discussed before. The balance between diffusion limitations and kinetics is clearly influenced by the Pt loading, in agreement to other studies in literature [67].

Figure 5.9a also shows that, when the current is normalized per geometrical area, the curves for samples prepared by the polyol method shift to the right with increasing loading, in agreement with studies on Pt/Vulcan [68]. This is obviously caused by a higher intrinsic electrocatalytic activity for the ORR when the Pt loading increases. Moreover, the sample prepared by the polyol method with 0,31mg/cm^2 presents a higher current density in the kinetic region as compared to Pt/Vulcan with 0,38mg/cm^2. The relatively low intrinsic electrocatalytic activity of Pt/Vulcan is probably due to its relatively low Pt surface area, as compared to Pt/CNFs (**table 5.1**).

Samples prepared by the polyol method with 0,14 and 0,31mg Pt/cm^2 show larger diffusion limiting currents than Pt/Vulcan with 0,38mg Pt/cm^2 (**figure 5.9a**). This could be due to differences in the electroactive Pt surface area (**table 5.1**) or in both external and internal diffusion, as discussed below.

5.3.7 Oxygen reduction reaction (ORR): rotating disk electrode (RDE)

In order to better understand differences in diffusion limitations, a study with RDE is performed. **Figures 5.10a and 5.10b** show the linear sweep voltammograms, normalized per geometrical area and per mass of Pt respectively, of the sample prepared by the polyol method with 0,31mg Pt/cm^2 and Pt/Vulcan with 0,38mg Pt/cm^2 at different rotation speeds. The current density increases when the voltage decreases, similar to stationary electrodes (**figure 5.9**), and reaches a plateau indicating the diffusion limiting current. The diffusion limiting current increases as the rotation rate increases (**figures 5.10a and 5.10b**), in agreement with other studies in literature [67-68]. In both graphs (**figures 5.10a and 5.10b**) the sample prepared by the polyol method presents a diffusion limiting current higher than that observed for the Pt/Vulcan sample at lower rotation speeds. However, the difference in diffusion limiting currents between the Pt/Vulcan and polyol sample decreases as the rotation speed increases.

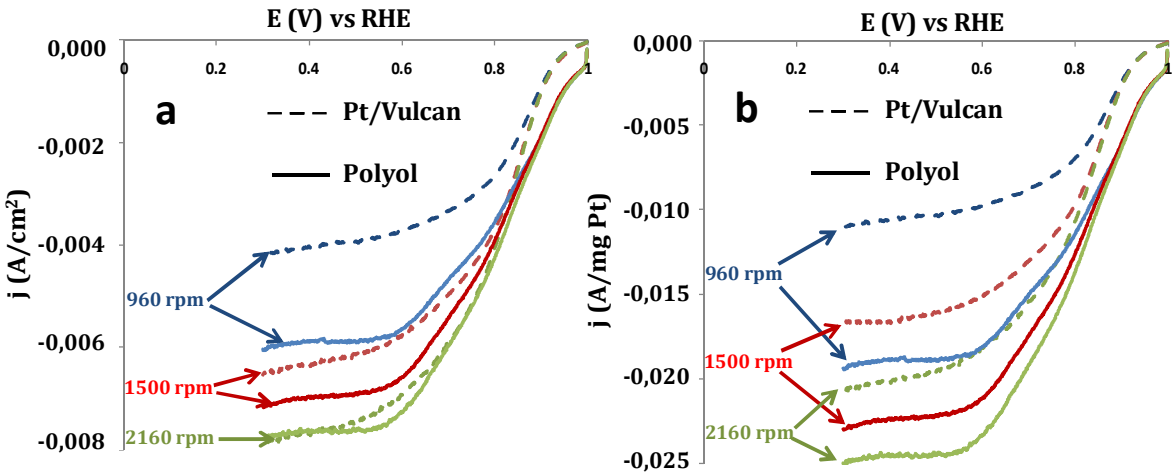

Figure 5.10: *linear sweep voltammograms of samples prepared by the polyol method with 0,31mg Pt/cm² and the commercial Pt/Vulcan with 0,38mg Pt/cm² in 0,5M H_2SO_4 saturated with O_2 at 5mV/s and at different rotation speeds. a) Current normalized per geometrical area; b) Current normalized per mass of Pt*

When the rotation speed is low, the diffusion layer is relatively thick [69] and the process is mainly limited by external diffusion. In this case, the sample prepared by the polyol method appears to have less external resistance than Pt/Vulcan. This leads to higher diffusion limiting currents for the Pt/CNFs at low rotation speeds (**figures 5.9 and 5.10**), in agreement to RDE studies on thin layers of Pt/CNTs with much lower loadings [70]. We propose this is due to the intrinsic morphology of the CNF layer, in terms of roughness and tortuosity, as compared to the Vulcan carbon [7-8], enhancing the accessibility of Pt particles to oxygen diffusion at low rotation speeds. Changes from laminar to turbulent flow on very rough surfaces [71] might decrease the external diffusion limitations. Moreover, a higher effective surface area of a rough surface [72], as compared to the geometrical area, might also explain the differences in the diffusion limiting current.

On the other hand, when the rotation speed increases, the diffusion layer becomes thin and the process is mainly limited by internal diffusion. We observe that, at the same rotation speed, the difference in diffusion limiting currents between both samples decreases as the rotation speed increases (**figures 5.10a and 5.10b**). Therefore, Pt/Vulcan appears to have less internal resistance than the sample prepared by the polyol method. We hypothesize this is due to the fact that

Pt deposited by the polyol method is located deeper, as compared to Pt/Vulcan (**figures 5.7c and 5.7d**), inducing stronger internal diffusion limitation in the Pt/CNF layer. Nevertheless, similar or higher limiting diffusion currents are found for the polyol sample at high rotation speeds (**figures 5.10a and 5.10b**), although its Pt loading (0,31mg Pt/cm^2) is lower than Pt/Vulcan (0,38mg Pt/cm^2). The negative effect of the relatively longer internal diffusion length is apparently compensated by enhanced external mass transfer because of roughness, and/or by enhanced internal diffusion because of high porosity and low tortuosity.

5.4 Conclusions

Pt nanoparticles deposited on a CNF layer by the sputtering method are located shallower than Pt nanoparticles deposited by the polyol method. However, the average Pt particle size increases with Pt loading for sputtered samples, whereas the particle size can be better controlled by the polyol method at different loadings. The Pt electrochemical surface area, when deposited on CNFs, is much higher than that obtained for commercial Pt/Vulcan independent of the method used. However, sputtered samples have lower catalytic activity for the ORR than samples prepared by the polyol method with similar Pt loading and particle size. The intrinsic ORR kinetic current is higher for samples prepared by the polyol method for relatively lower loadings than Pt/Vulcan. Samples prepared by the polyol method suffer more from internal mass transfer limitations than Pt/Vulcan due to a deeper Pt location. However, the external oxygen diffusion is higher for Pt/CNFs at lower Pt loadings, as compared to Pt/Vulcan, due to the intrinsic morphology of the CNFs. The CNF based electrode holds promise at low Pt loadings, especially when Pt could be positioned closer to the outer surface.

Acknowledgements

I would like to thank Dr. K. Nijmeijer, Dr. G. Merle (Membrane Technology group) and Prof M. Koper (University of Leiden), for letting me use their electrochemical facilities and for the fruitful discussions. I also thank M. Duca, G. Cadafalch and Dr. R. Salgado (Technical University of Lisbon) for electrochemical assistance provided to achieve the work in this chapter and for fruitful discussions. I also thank Dr. Ties Bos for his contribution on XRF characterization.

References

[1] Y. Shao, G. Yin, Z. Wang, Y. Gao, J. Power Sources 167 (2007) 235.

[2] S. Litster, G. McLean, J. Power Sources 130 (2004) 61.

[3] H.A. Gasteiger, S.S.Kocha, B. Sompalli, F.T. Wagner, Appl. Catal. B 56 (2005) 9.

[4] E. Antolini, Appl. Catal. B: Environmental 88 (2009) 1.

[5] A. Guha, T.A. Zawodzinski Jr, D.A. Schiraldi, J. Power Sources 172 (2007) 530.

[6] V. Raghuveer, A. Manthiram, J. Electrochem. Soc. 152 (2005) A1504.

[7] I. Kvande, J. Zhu, T.J. Zhao, N. Hammer, M. Rønning*et al.*, J. Phys. Chem. C 114 (2010) 1752.

[8] J. Kaiser, P.A. Simonov, V.I. Zaikovskii, C. Hartnig, L. Jörissen*et al.*, Appl. Electrochem. 37 (2007) 1429.

[9] L. Li, Y. Xing, J. Power Sources 178 (2008) 75.

[10] H.S. Oh, K.H. Lim, B. Roh, I. Hwang, H. Kim, Electrochim. Acta 54 (2009) 6515.

[11] R. Kannan, V.K. Pillai, J. Indian Inst. Sci. 89 (2009) 425.

[12] W. Zhang, P. Sherrell, A.I. Minett, J.M. Razal, J. Chen, Energy Environm. Sci. 3 (2010) 1286.

[13] Y. Shao, J. Liu, Y. Wang, Y. Lin, J. Mater. Chem. 19 (2009) 46.

[14] K. Lee, J. Zhang, H. Wang, D.P.Wilkinson, J. Appl. Electrochem. 36 (2006) 507.

[15] F. Zaragoza-Martín, D. Sopeña-Escario, E. Morallón, C.S.M. de Lecea, J. Power Sources 171 (2007) 302.

[16] X. Wang, W. Li, Z. Chen, M. Waje, Y. Yan, J. Power Sources 158 (2006) 154.

[17] K.P. De Jong, J.W. Geus, Catal. Rev. - Sci. Eng. 42 (2000) 481.

[18] L. Calvillo, M. Gangeri, S. Perathoner, G. Centi, R. Moliner *et al.*, J. Power Sources 192 (2009) 144.

[19] L. Cindrella, A.M. Kannan, J.F. Lin, K. Saminathan, Y. Ho *et al.*, J. Power Sources 194 (2009) 146.

[20] G. Lin, T. Van Nguyen, J. Electrochem. Soc. 152 (2005) A1942.

[21] M. Schulze, N. Wagner, T. Kaz, K.A. Friedrich, Electroch. Acta 52 (2007) 2328.

[22] P.A. Stuckey, J.F. Lin, A.M. Kannan, M.N. Ghasemi, Fuel Cells 10 (2010) 369.

[23] Q. Duan, B. Wang, J. Wang, H. Wang, Y. Lu, J. Power Sources 195 (2010) 8189.

[24] S. Pacheco Benito, L. Lefferts, J. Colloid Interface Sci. (in press)

[25] A.M. Kannan, P. Kanagala, V. Veedu, J. Power Sources 192 (2009) 297.

[26] V. Kamavaram, V. Veedu, A.M. Kannan, J. Power Sources 188 (2009) 51.

[27] S. Celebi, T.A. Nijhuis, J. Van Der Schaaf, F.A. De Bruijn, J.C. Schouten, Carbon 49 (2011) 501.

[28] T. Zhao, I. Kvande, Y. Yu, M. Ronning,*et al.*, J. Phys. Chem. C 115 (2011) 1123.

[29] C. Du, B. Wang, X. Cheng, J. Power Sources 187 (2009) 505.

[30] T. Bordjiba, M. Mohamedi, L.H. Dao, Nanotechnology 18 (2007).

[31] E.A. Ticianelli, J.G. Beery, S. Srinivasan, J. Appl. Electrochem. 21 (1991) 597.

[32] J.H. Wee, K.Y. Lee, S.H. Kim, J. Power Sources 165 (2007) 667.

[33] M.S. Saha, R. Li, X. Sun, J. Power Sources 177 (2008) 314.

[34] X. Wang, M. Waje, Y. Yan, Electrochem. Solid-State Lett. 8 (2005) A42.

[35] A. Esmaeilifar, S. Rowshanzamir, M.H. Eikani, E. Ghazanfari, Energy 35 (2010) 3941.

[36] X. Sun, R. Li, D. Villers, J. Dodelet, S. Désilets, Chem. Phys. Lett. 379 (2003) 99.

[37] M.M. Waje, X. Wang, W. Li, Y. Yan, Nanotechnology 16 (2005) S395.

[38] H. Tang, J. Chen, L. Nie, D. Liu, W. Deng J. Colloid Interface Sci 269 (2004) 26.

[39] X. Chen, N. Li, K. Eckhard, L. Stoica, W. Xia *et al.*, Electrochem. Commun. 9 (2007) 1348.

[40] M.C. Tsai, T.K. Yeh, C.H. Tsai, Electrochem. Commun. 8 (2006) 1445.

[41] K. Saminathan, V. Kamavaram, V. Veedu, A.M. Kannan, Int. J. Hydrogen Energy 34 (2009) 3838.

[42] D. Villers, S.H. Sun, A.M. Serventi, J.P. Dodelet, S. Désilets, J. Phys. Chem. B 110 (2006) 25916.

[43] M. Gangeri, G. Centi, A. La Malfa, S. Perathoner, R. Vieira *et al.*, Catal. Today 102-103 (2005) 50.

[44] S. Pacheco Benito, L. Lefferts, Surf. Coat. Technol. (submitted)

[45] C. Bock, C. Paquet, M. Couillard, G.A. Botton, B.R. MacDougall, J. Am. Chem. Soc. 126 (2004) 8028.

[46] H.S. Oh, J.G. Oh, Y.G. Hong, H. Kim, Electrochim. Acta 52 (2007) 7278.

[47] S.L. Knupp, W. Li, O. Paschos, T.M. Murray, J. Snyder*et al.*, Carbon 46 (2008) 1276.

[48] W.S. Rasband: ImageJ, http://rsb.info.nih.gov/ij/download.html

[49] M. Bos, J.A.M. Vrielink, Anal. Chim. Acta 373 (1998) 291.

[50] M.S. Mamat, S.A. Grigoriev, K.A. Dzhus, D.M. Grant, G.S. Walker, Int. J. Hydrogen Energy 35 (2010) 7580.

[51] G.J.M. Janssen, E.F. Sitters, J. Power Sources 171 (2007) 8.

[52] J.A. Poirier, G.E. Stoner, J. Electrochem. Soc. 141 (1994) 425.

[53] A. Caillard, C. Charles, R. Boswell, P. Brault, Nanotechnology 18 (2007).

[54] M.D. Gasda, R. Teki, T.M. Lu, N. Koratkar, G.A. Eisman*et al.*, J. Electrochem. Soc. 156 (2009) B614.

[55] K.L. Huang, Y.C. Lai, C.H. Tsai, J. Power Sources 156 (2006) 224.

[56] I. Kvande, S.T. Briskeby, M. Tsypkin, M. Rønning, S. Sunde*et al.*, Top. Catal. 45 (2007) 81.

[57] W. Li,C. Liang, W.Zhou, J. Qiu, Z. Zhou *et al.*, J. Phys. Chem. B 107 (2003) 6292.

[58] A. Guha, W. Lu, T.A. Zawodzinski Jr, D.A. Schiraldi, Carbon 45 (2007) 1506.

[59] P. Brault, A. Caillard, A.L. Thomann, J. Mathias, C. Charles *et al.*, J. Phys. D: Appl. Phys. 37 (2004) 3419.

[60] J.B. Floriano, E.A. Ticianelli, E.R. Gonzalez, J. Electroanal. Chem. 367 (1994) 157.

[61] G. Zhao, J. He, C. Zhang, J. Zhou, X. Chen, J. Phys. Chem. C 112 (2008) 1028.

[62] R.N. Carter, S.S. Kocha, F. Wagner, M. Fay, H.A. Gasteiger, ECS Trans. 11 (2007) 403.

[63] Y.-M. Tsou, L. Cao, E.D. Castro, ACS, Division Fuel Chemistry 49 (2004) 679.

[64] L. Gan, H.D. Du, B.H. Li, F.Y. New Carbon Materials 25 (2010) 53.

[65] Y.H. Shih, G.V. Sagar, S.D. Lin, J. Phys. Chem. C 112 (2008) 123.

[66] D.Geng, H. Liu, Y.Chen, R. Li, X. Sun, *et al.*, J. Power Sources 196 (2011) 1795.

[67] K.J.J. Mayrhofer, D. Strmcnik, B.B. Blizanac, V. Stamenkovic, M. Arenz,*et al.*, Electrochim. Acta 53 (2008) 3181.

[68] J. Jiang, B. Yi, J. Electroanal. Chem. 577 (2005) 107.

[69] A.J. Bard, L.R. Faulkner, Electrochemical methods: fundamentals and applications. 2nd ed. ed., John Wiley & Sons, New York, 2001.

[70] X. Li, S. Ge, C.L. Hui, I.M. Hsing, Electrochem. Solid-State Lett. 7 (2004) A286.

[71] S. Bruckenstein, J.W. Sharkey, J.Y. Yip, Anal. Chem. 57 (1985) 368.

[72] G. March, F. Volatron, F. Lachaud, X. Cheng, B. Baret,*et al.*, Electrochim. Acta 56 (2011) 5151.

Chapter 6

Wettability of CNF layers on Ni foils

"If you think you're too small to have an impact, try going to bed with a mosquito in the room" (Anita Roddick)

Abstract

Carbon nanofiber (CNF) layers have been directly synthesized on nickel foils by chemical vapor deposition at 450°C using different H_2 concentrations and reaction times. The addition of 5% H_2 produces thicker, rougher and more porous CNF layers than when 1% H_2 is used. The roughness and porosity increases with reaction time when 5, 10 or 20% H_2 are used; however, this effect is less pronounced when 1% H_2 is used. CNFs are 50-55nm in diameter and have a fishbone type structure. We have studied the influence of CNF layer thickness, porosity and surface roughness on the interaction with water by measuring the contact angle. The water wetting properties of the samples are more significantly influenced by the CNF layer thickness than both surface roughness and porosity. When the CNF layer is thicker than ca. 20μm, the surface is hydrophobic and the contact angle increases with surface roughness and porosity. When the CNF layer is thinner than ca. 20μm, the surface is hydrophilic and the contact angle decreases with increasing surface roughness and porosity. This behavior is attributed to penetration of water, making contact with the hydrophilic C layer between the CNF layer and the foil.

This chapter is based on the publication: S. Pacheco Benito, L. Lefferts. *Journal of Colloid and Interface Science* (in press)

Chapter 6

6.1 Introduction

Carbon nanostructures, such as nanofibers (CNFs), are graphitic materials that offer various properties such as high surface area, high thermal and electronic conductivity and high inertness [1-8]. These properties make carbon nanostructures promising for many applications such as catalyst supports [9-12], batteries and fuel cells [13-15], hydrogen storage [16-17], polymer reinforcements [18-19], super-capacitors [20], sensors [21], and super-hydrophobic layers [22]. In many of these applications, the interaction of thin layers of CNFs on a supporting material with liquids is important for the performance, *e.g.* influencing the yield of a heterogeneous catalyzed conversion, the pressure drop in a micro-channel reactor and capacity of transfer of protons, electrons and oxygen or hydrogen in membrane-electrode-assemblies in fuel cells. The interaction of carbon films with water can be attractive (hydrophilic, contact angles, *i.e.* CA, <90°) or repulsive (hydrophobic CA >90°, super-hydrophobic CA >150°), depending on any chemical modification and the morphology of the carbon film [23-30]. For example, the wettability of CNFs can be modified by graphitization treatments [31-32] and incorporation of oxygen-containing surface moieties [33-36].

Liquid wettability and repellency are important properties of solid surfaces from both fundamental and practical aspects. There has been special interest in the preparation of super-hydrophobic surfaces [37-42], as well as their applications as self-cleaning surfaces [43] and for drag reduction in micro-fluidic devices [44-46]. Two different wetting behaviors have been suggested depending on the nature and extent of the surface roughness: the Wenzel state [47], assuming that the bottom of the droplet maintain contact with the entirety of the rough surface, and Cassie-Baxter state [48], assuming that the bottom of the droplet partially wets the rough substrate due to the existence of air pockets in between the microstructures. However, these models are normally used to describe the properties of two dimensional isotropic surfaces and they are not easily applicable for three dimensional anisotropic surfaces, as indicated already in literature for carbon nanostructured layers [49-51].

Examples of super-hydrophobic materials in nature [52], such as the lotus leaf or water strider´s leg, reveal a unique micro- and nano-roughness [53]. According to literature, there are three main conditions that have to be met in order to obtain super-hydrophobicity [54-55]: 1) the existence of enough air in between the microstructures so that the forces of the liquid-solid contact line overcome the forces of the partly-unsupported droplet weight; 2) sufficient height of the microstructures is to prevent the liquid bridging microstructures to touch the base of the microstructures; 3) intrinsic hydrophobic or low surface energy surfaces such as teflon®-like [56-57] or silanes [45, 58-59]. Graphite and untreated graphitized carbons are considered intrinsically hydrophobic, although the CA of flat dense graphite is slightly below 90° [23, 60-61].

It is known that modification of surface roughness on carbon films leads to either very hydrophilic or very hydrophobic surfaces, although the effect is not well understood [51, 62]. However, there are no systematic studies on the effect of both CNF layer thickness and roughness on wettability. In **chapter 2** we showed the growth of homogeneous CNF layers directly on various metal foils [63]. And in **chapter 3** we showed that the thickness of an apparent dense C layer, which is between the CNF layer and the Ni foil, determines the attachment of CNFs to the substrate. In the present work we select samples with controllable well-attached CNF layer thickness, based on those previous results, aiming to understand the effect of the CNF layer thickness, CNF surface roughness and porosity, on water wettability without any further post-treatment. We also report on the type of CNFs, CNF diameters and CNF surface chemistry.

6.2 Experimental

6.2.1 Materials

Nickel foils (0,1mm thick, 99,5%, Alfa Aesar) were used as active catalytic substrates. Square sample pieces (10 x 10mm) were prepared from the as-received sheet by wire cut electrical discharge machining (Agiecut Challenge 2). The foils were degreased ultrasonically in acetone and dried at room temperature before being loaded into a quartz tube. Hydrogen, nitrogen and air (99,999%, Praxair), and ethylene (99,95%, Praxair) were used for pretreatment and CNF formation without further purification.

6.2.2 Carbon nanostructures formation

An in-house built quartz reactor of 12mm inner diameter was used to place the samples for CNF growth by catalytic chemical vapor deposition (C-CVD). The temperature was raised in N_2 from room temperature to the desired temperature at a rate of 7,5°C/min. The samples were first pretreated in air (20% air and balance N_2) under a total flow rate of 100ml/min for 1h at 500°C. After the pretreatment, the temperature was adjusted to 450°C in N_2. The CNFs were grown using a gas mixture of hydrogen and ethylene (C_2H_4) in nitrogen with a total flow rate of 100ml/min. The concentration of C_2H_4 (25% v/v) was kept constant in all experiments and the nitrogen flow was adjusted whenever hydrogen concentration (0–20%) was modified. The CNF growth time was varied between 15 and 300 minutes. Finally, ethylene and hydrogen (if used) gas streams were shut off and the system was cooled down to room temperature under 100ml/min of N_2 at a rate of 10°C/min.

6.2.3 Characterization

The amount of well-attached carbon was assessed by weighing after removing any poorly attached CNFs by flowing nitrogen (120l/min) for 1 minute over the flat samples in a cylindrical quartz tube (11mm in diameter) at a linear speed of 21m/s. The weights were determined using a Metler Toledo AE163 balance with precision up to 0,01mg. The morphology and cross sections of the carbon layers were studied using a scanning electron microscope (SEM) JEOL 6250LV, equipped with a secondary electrons detector. Cross sections were obtained by cutting the samples with a pair of scissors after immersing shortly in liquid N_2. High resolution images were taken using a LEO 1550 FEG SEM. The averaged thicknesses of the carbon layers were calculated from 10 measurements of the thickness at different locations at cross section in SEM pictures using the freeware ImageJ [64]. The average CNF diameter was calculated from 100 individual nanofibers also using ImageJ.

For calculating the surface roughness, three stereoscopic images of the same region (~ 450µm x 300µm) were taken by SEM with eucentric tilting at 0, 5 and 10°. Due to the anisotropy of our samples, the use of area (3D) roughness parameters such as *Sa* (**eq. 6.1**), also called average height of the surface, is more convenient than the classical profile (2D) roughness measurement.

$$Sa = \frac{1}{L_x L_y} \int_0^{l_x} \int_0^{l_y} |h(x, y)| dx\, dy \qquad \textbf{(eq. 6.1)}$$

where L_x and L_y are the side lengths of the sampling area and h is the height distance from the reference plane. MeX® software (Alicona) was used to convert the stereoscopic images to 3D images and determine *Sa* as described in literature [65]. Three different spots of the same samples were used to obtain an average*Sa*. It has been demonstrated [66] that determination of 3D roughness parameters based on reconstruction of stereoscopic images lead to comparable results as obtained with classical stylus and white light profilometers.

The bulk porosity of the CNF layer was calculated assuming that the bulk densities of the CNFs as well as the dense C layer are equal to the bulk density of graphite, *i.e.* 2,2g/cm^3:

$$\varepsilon_{CNF\,layer}(\%) = 100\ \frac{V_{bulk} - V_{CNFs}}{V_{bulk}} \qquad \textbf{(eq. 6.2)}$$

where ε is the porosity, V_{CNFs} is the volume of the solid CNFs and V_{bulk} is the sum of the volume of the solid CNFs and void volume, which are calculated as follows:

$$V_{bulk} = h_{CNF\,layer}\, S \qquad \textbf{(eq. 6.3)}$$

$$V_{CNFs} = \frac{w_{CNFs}}{d_{CNFs}} \qquad \textbf{(eq. 6.4)}$$

where $h_{CNF\ layer}$ is the thickness of the CNF layer and S is the geometrical surface area of the sample. Moreover, d_{CNFs} is the density of the CNFs and w_{CNFs} is the weight of the CNFs calculated as follows:

$$w_{CNFs} = \frac{w_{total}}{2} - w_c \qquad \textbf{(eq. 6.5)}$$

$$w_c = d_c\, V_c \qquad \textbf{(eq. 6.6)}$$

$$V_c = h_c\, S \qquad \textbf{(eq. 6.7)}$$

where w_{total} is the total weight of C and CNF layers on both sides of the foil, and w_c, d_c, V_c and h_c are the weight, density, volume and thickness of the C layer respectively.

The surface composition of the CNF layers was analyzed at four different points using a Quantera XPS equipment with Al kα radiation. A Phillips CM300ST-FEG TEM was used to analyze the morphology of single CNFs. The initial static CA was measured at six different spots of each sample with a Dataphysics OCA 20 CA meter using 4µl deionized water droplets.

6.3 Results

6.3.1 Influence of H_2 concentration and time of reaction

Figure 6.1 shows the amount of well-attached carbon deposited on the Ni foil at different H_2 %. It is clear that, independent of the H_2 concentration, the amount of well-attached carbon increases with reaction time, but not linearly. The amount of well-attached carbon, at similar reaction time, increases in this order: 0 < 1 < 20 < 10 < 5% H_2 concentration. These data are consistent with the results on **chapter 3** (**figures 3.4 and 3.6**), where we discussed the relationship between the original thicknesses (*i.e.* without removal of poorly attached carbon) of CNF and C layer and the mechanical stability of the carbon deposits.

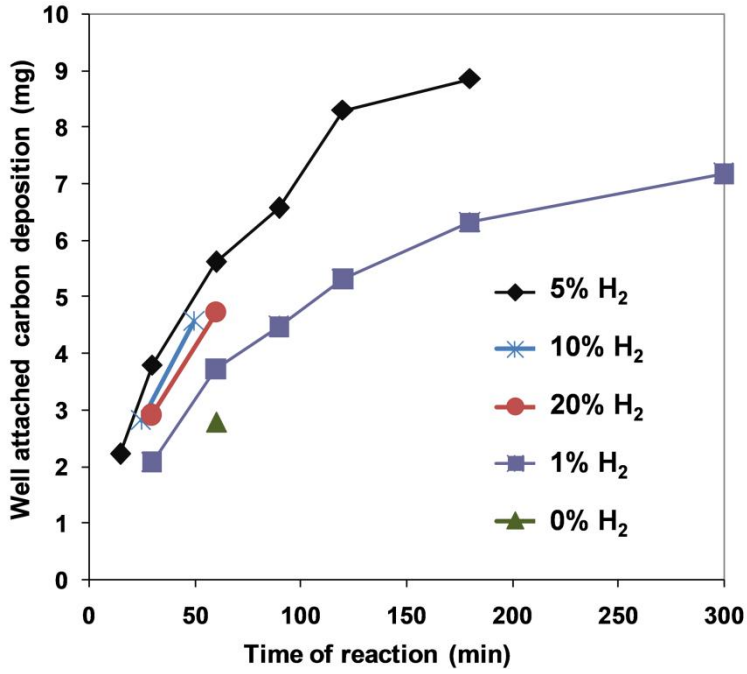

Figure 6.1: *amount of well-attached carbon deposition on Ni foils per time of reaction at different H_2 concentrations*

Figure 6.2 shows representative cross section images of the C and CNF layers when 5% H_2 is used at different reaction times. It is clear that the thickness of the well-attached CNF layer increases with reaction time. Similar observations were obtained for samples prepared using different H_2% (not shown).

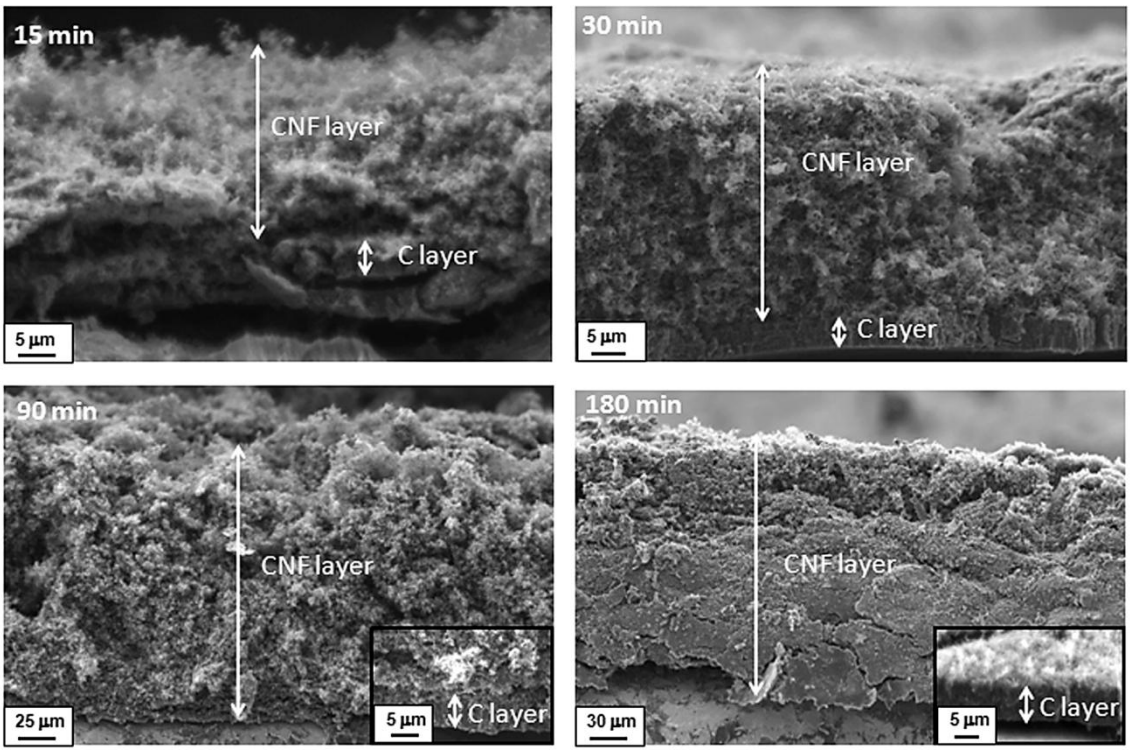

Figure 6.2: *variation of C and CNF layer thickness with time of reaction with 5%H_2 addition. Higher magnification insets of the C layer are added when necessary for clear observation*

Figure 6.3a shows that the increase of the CNF layer is more pronounced when 5%H_2 is used as compared to 1% H_2. For example, after 180min of reaction, 123 and 24µm thick CNF layers are obtained using 5 and 1% H_2 respectively. The addition of 10 or 20% H_2 does not make a noticeable difference for the reaction times used in this study. **Figure 6.3b** shows the increase of the C layer thickness with time of reaction in a similar manner for all the H_2 concentrations. The C layer thickness increases is this order: 5 < 10 ~ 20 < 1 < 0% H_2, in agreement with **figure 3.4b**. It is interesting to note that without any addition of H_2, exclusively the C layer is being formed, whereas no CNFs are observed (**figures 6.3a and 6.3b**), in agreement with **figures 3.4a and 3.4b**.

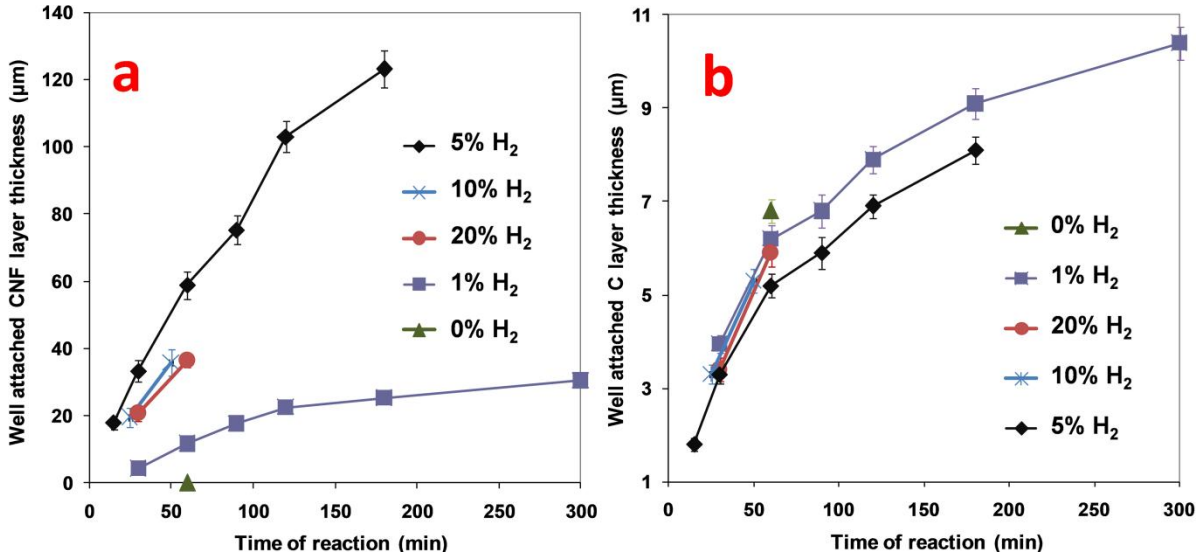

Figure 6.3: *influence of H_2 concentration with reaction time on the increase of the thickness of a) well-attached CNF layer and b) well-attached C layer thickness*

6.3.2 CNF layer roughness and porosity

Figures 6.4a and 6.4b show representative top view morphological images of the samples prepared with 5% and 1% H_2 addition, respectively, during 180min of reaction. In low magnification, we observe that the addition of 5% H_2 produces CNF bumps typically in the order 5-25µm in diameter (**figure 6.4a**), similar to the ones observed on a super-hydrophobic lotus leaf [67]. However, the use of 1% H_2 produces a smoother surface, in the micro scale, composed of entangled CNFs (**figure 6.4b**). The CNF average diameter, calculated from high resolution images (insets **figures 6.4a and 6.4b**), is comparable after the use of both H_2 concentrations, 55 ± 15nm after 1% H_2 and 50 ± 20nm after 5% H_2. The different surface roughness is also observed in the 3D reconstructions (**figures 6.4c and 6.4d**) determined from 3 tilted images similar to the images presented in **figures 6.4a and 6.4b**. It is clear that the average surface roughness, *Sa*, is much bigger when 5% H_2 is used (*Sa* = 1,95µm, **figure 6.4c**) as compared to the use of the 1% H_2, (*Sa* = 0,81µm, **figure 6.4d**). The analysis of **figure 6.4** was done for all samples (not shown).

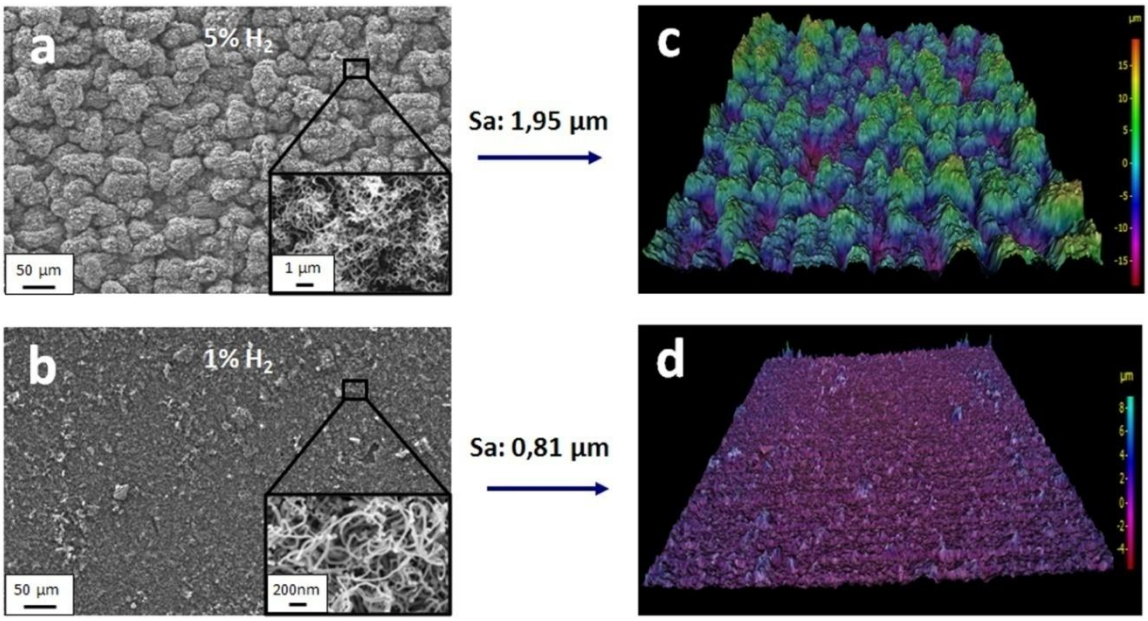

Figure 6.4: *low and high magnification 0° tilted image of CNF layer morphology after 180min of reaction and a) 5% H_2 and b) 1% H_2; c and d) projected images of the 3D reconstructions of 3 tilted images (0, 5 and 10°) at low magnification (~450 x 300µm) by MeX® software, demonstrating the different surface roughness (Sa)*

Figures 6.5a shows how the CNF layer average roughness increases with time of reaction when 5, 10 or 20% H_2 are used; addition of 20% H_2 results in the roughest surfaces. However, the surface roughness remains almost constant when 1% H_2 is added. The porosity of the CNF layer was estimated for all CNF layers according to **eqs. 6.2-6.7**. The total weight of carbon deposited, w_{total}, was determined from **figure 6.1**; the CNF and C layer thicknesses, $h_{CNF\ layer}$ and h_C respectively, were determined from**figure 6.3**. The resulting porosities of the CNF layers are shown in **figure 6.5b**. We observe similar effect as for surface roughness. Porosity is rather stable in time when 1% H_2 is used, whereas it increases with time for 5, 10 and 20% H_2 (**figure 6.5b**).

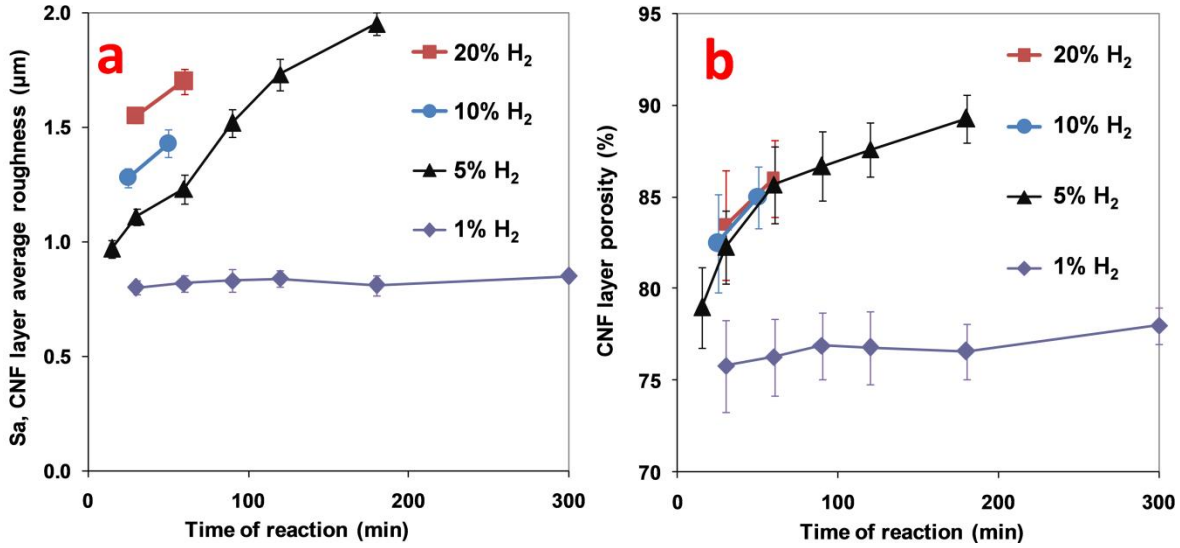

Figure 6.5: *a) variation of the CNF layer average roughness with time of reaction at different H_2 concentrations; b) variation of the CNF layer porosity with time of reaction at different H_2 concentrations*

6.3.3 Oxygen content on the surface

Table 1 shows the oxygen (O) and Ni atomic concentrations as measured with XPS for 6 samples prepared using different H_2 concentrations and reaction times. The O content is lower when 1% H_2 is used, as compared to when 5% H_2 is used. Moreover, the amount of Ni detected on the surface of the CNF layers is rather low in all cases with no significant differences.

Table 1: *XPS oxygen and nickel atomic concentrations on the CNFs at different H_2 concentrations and reaction times*

Sample	O content (%)	Ni content (%)
1% H_2 - 30min	1,68 ± 0,04	0,31 ± 0,02
1% H_2 - 60min	1,29 ± 0,06	0,14 ± 0,04
1% H_2 - 90min	1,42 ± 0,08	0,20 ± 0,03
5% H_2 - 30min	1,97 ± 0,07	0,27 ± 0,05
5% H_2 - 60min	2,35 ± 0,05	0,21 ± 0,03
5% H_2 - 90min	2,24 ± 0,10	0,19 ± 0,04

6.3.4 Morphology of single CNFs

Figure 6.6 shows a representative image of the morphology of CNFs grown from a Ni foil. We observe that CNFs have typically straight morphology, independent of the H_2 concentration; however, few curly nanofibers are also observed (**figure 6.6a**). Ni particles are normally located at the tip of the fibers, and they are rarely either in the middle of a fiber or constituting a multiple growth (**figure 6.6a**). CNFs have a fishbone type morphology (**figure 6.6b**), as would be generally expected for Ni particles and Ni substrates at temperatures ranging from 450-600°C [68].

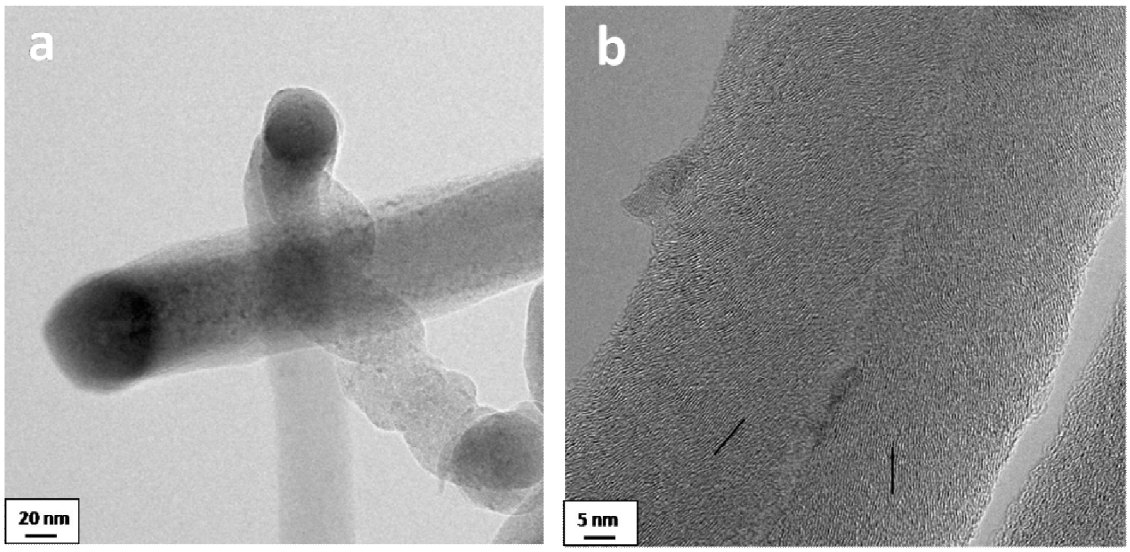

Figure 6.6: *representative CNFs grown on Ni foils. a) Straight and curly CNFs with Ni particle at the top and middle of the fibers after 60min of reaction and 5% H_2 b) fishbone structure of a fiber grown after 60min of reaction and 1% H_2*

6.3.5 Wettability

Figure 6.7 shows the contact angles (CAs) of water on the surfaces for samples prepared with different H_2 concentrations. It is clear that the most hydrophilic layer corresponds with the sample prepared in absence of external H_2, *i.e.* without CNFs (**figure 6.3**). Therefore, the C layer is quite hydrophilic, with a CA of ~10°. Moreover, the CA increases with the reaction time for CNF layers, independent of the H_2 concentration. Samples grown when 1% H_2 is added present lower CAs than samples grown at higher H_2 concentration, for similar reaction times. If 5, 10 or 20% H_2 are used, hydrophobic samples are obtained after 20-

40min of reaction; whereas if 1% H_2 is used, more than 90min are needed to obtain hydrophobic samples. Super-hydrophobic samples (CA >150°) are obtained when 5% H_2 is used combined with at least 90min of reaction time (**figure 6.7**).

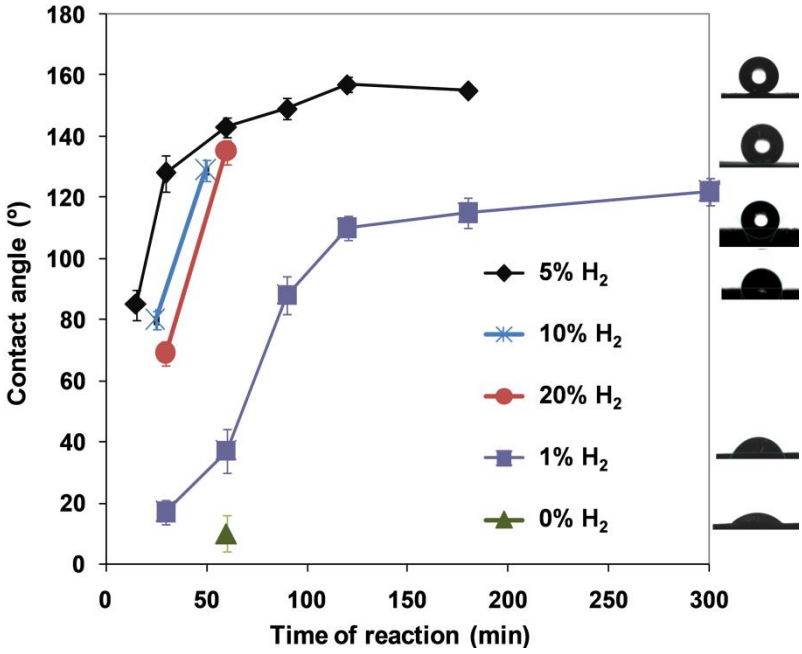

Figure 6.7: *variation of the CA of the carbon layers with reaction time. Insets of representative CA pictures are added on the right side*

6.4 Discussion

6.4.1 Influence of surface chemistry

The oxygen content of samples that were grown by using 5% H_2 appear to be higher than when 1% H_2 is used (**table 1**). However, the CAs of samples using 5% H_2 are higher than when using 1% H_2, for the same time of reaction (**figure 6.7**). This would be opposite to studies that show that the introduction of oxygen containing species, *via* various oxidation pretreatments of CNFs, increases wettability in water [33-36]. Apparently, the range of the oxygen content of our samples (1,3-2,3%, **table 1**) is too low, as compared to values obtained after oxidation pretreatments (typically 5-10%), to draw any conclusion about the effect of the surface chemistry. Therefore, hereafter we assume that the surface chemistry does not have a noticeable effect on the CA in this study and, consequently, we will discuss the variation in wettability exclusively in terms of surface morphology.

6.4.2 Influence of CNF layer thickness and surface morphology

Figure 6.8a shows a good correlation between the CNF average surface roughness and the CNF layer porosity for all samples used in this study. This suggests that rougher CNF layers are also more porous, which is conceptually not surprising as highly porous materials have generally rough surfaces. **Figure 6.8b** shows that, when 5% H_2 is used, the CNF layer average roughness increases with the CNF layer thickness in a similar trend as the CNF layer porosity. These results predict a similar effect of either the CNF layer roughness or porosity on wettability, as it will be shown later.

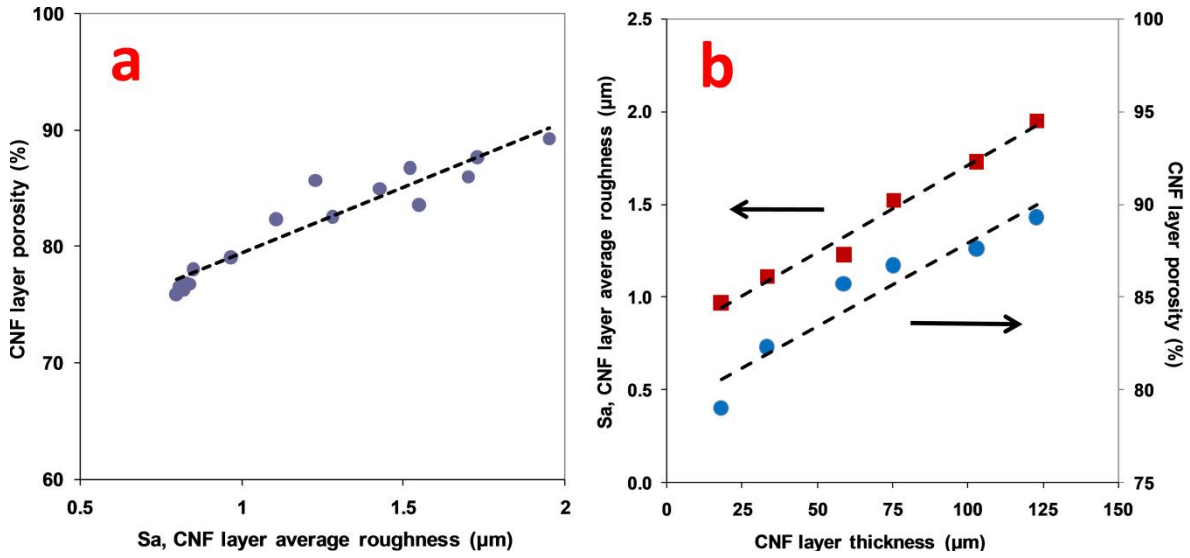

Figure 6.8: *a) correlation between CNF layer roughness and porosity for all samples used in this study; b) effect of the CNF layer thickness on the CNF layer roughness and porosity for samples grown when 5% H_2 is added*

Figure 6.9a shows the variation of the CA as function of the CNF layer thickness, revealing a clear increase of the CA with increasing CNF layer thickness. This is in agreement with studies that indicate a similar trend with increasing height of isotropic patterned micro-structures [57, 69-70]. It is interesting to note that when the CNF layer thickness is 0, *i.e.* the presence of exclusively a C layer (**figure 6.3**), the surface is quite hydrophilic (**figure 6.9a**). This suggests that the C layer present under the CNF layers is more easily wetted than CNFs. This is possibly induced by the relatively low crystallinity of the C layer [68]; CAs close to 0° were reported for highly disordered carbons [71]. The transition from

hydrophilic (CA <90°) to hydrophobic (CA >90°) surfaces occurs when the CNF layer is around 20µm thick. The CA keeps on increasing slowly for CNF layers thicker than 30µm, obtaining super-hydrophobic surfaces (CA >150°) when the CNF layer thickness is at least around 70µm.

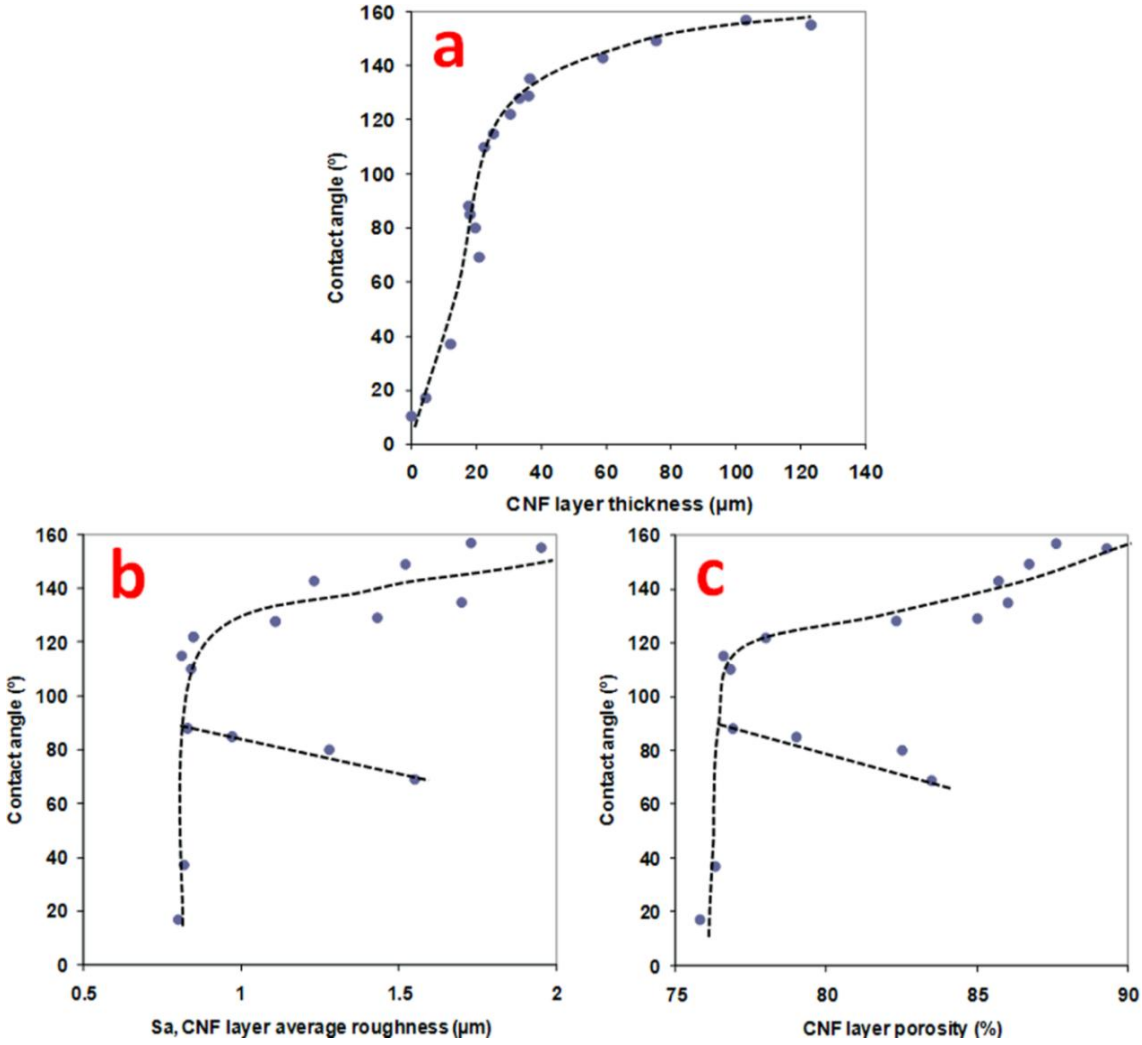

Figure 6.9: *variation of the contact angle with. a) CNF layer thickness; b) CNF layer average roughness; c) CNF layer porosity*

Figures 6.9b and 6.9c show the dependence of the CA with the CNF layer average roughness and CNF layer porosity, respectively, for all samples presented in this study. In both cases the correlation is similar, in agreement to**figure 6.8a**. CA mostly increases with surface roughness and porosity, in agreement with results on single wall CNT layers [72], amorphous carbon layers [62] or hydrophobized Si pillars [57]. The presence of air pockets under the water droplet

is responsible for very high CAs, as has been experimentally shown in literature [73-75]. However, some data points in **figures 6.9b and 6.9c** indicate an opposite trend, originating from the samples prepared with 10 and 20% H_2 concentration resulting in relatively thin (**figure 6.3a**) and rough CNF layers (**figure 6.5a**), as compared to samples prepared with 5% H_2 concentration for similar reaction times. This would indicate a dominant effect of the CNF thickness on wettability as compared to surface roughness and CNF layer porosity. Therefore, in order to discuss the effect of CNF layer thickness and surface roughness and porosity independently, we have selected samples keeping one parameter constant.

Figure 6.10 shows the influence of the CNF layer thickness on the CA for samples with similar surface roughness and porosity. It is clear that the wettability of the CNF layer decreases as the thickness of the CNF layer increases, as also observed in **figure 6.9a**. There is also a steeper increase of the CA when the CNF layer thickness increases up to 25µm, as compared to thicker layers (**figure 6.10**). This is in fair agreement with studies on hydrophobized pillars with similar dimensions that claim that the CA of super-hydrophobic surfaces is independent of the pillar height when the pillar height is larger than 20µm [59, 69, 76].

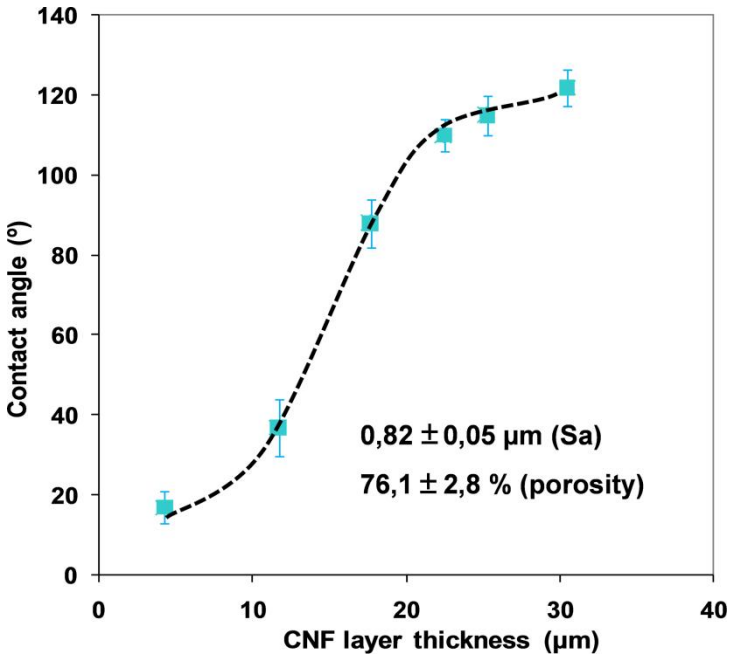

Figure 6.10: *influence of CNF layer thickness on the CA at constant roughness and porosity*

Figures 6.11a and 6.11b show the variation of the CA with the CNF layer surface roughness and CNF layer porosity, respectively, for similar CNF layer thicknesses. The CA increases with increasing roughness and porosity when the CNF layer thickness is approximately 34µm. The fraction of the surface of the droplet in contact with air increases with increasing porosity, at the expense of the interface with solid, which is responsible for the effect observed. This is similar to Cassie-Baxter state [48], as defined for regular surfaces. On the other hand, the CA decreases with increasing roughness and porosity when the CNF layer thickness is approximately 19µm (**figures 6.11a and 6.11b**).

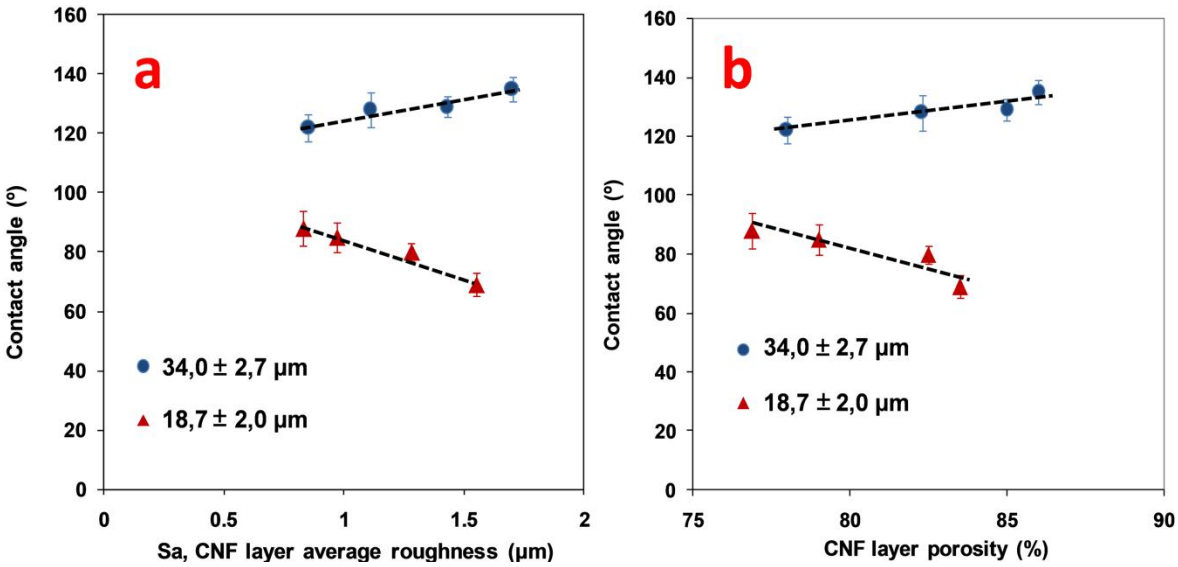

Figure 6.11: *influence of a) CNF layer average roughness and b) CNF layer porosity, on the CA for two different CNF layer thicknesses*

In this work, we observe a dominant effect of the CNF layer thickness on wettability (**figure 6.10**) as compared to the effect of surface roughness and porosity (**figure 6.11**). States in between Wenzel (total droplet penetration) and Cassie-Baxter (no droplet penetration) have been suggested in literature to explain the properties of anisotropic hydrophobic or super-hydrophobic layers [77-78], similar to the layers in the present study. The droplet size might also influence the wetting characteristics [79-80], but in this work the volume was kept constant at 4µl. Work is in progress to determine whether the penetration of the droplet is influenced by its size. It is also suggested that whether a liquid penetrates or not is

determined by the cost in surface energy for wetting the internal surface of the layer [81]. We hypothesize that a similar phenomenon is important here. We propose different wetting modes of CNF layers as shown in **figure 6.12**.

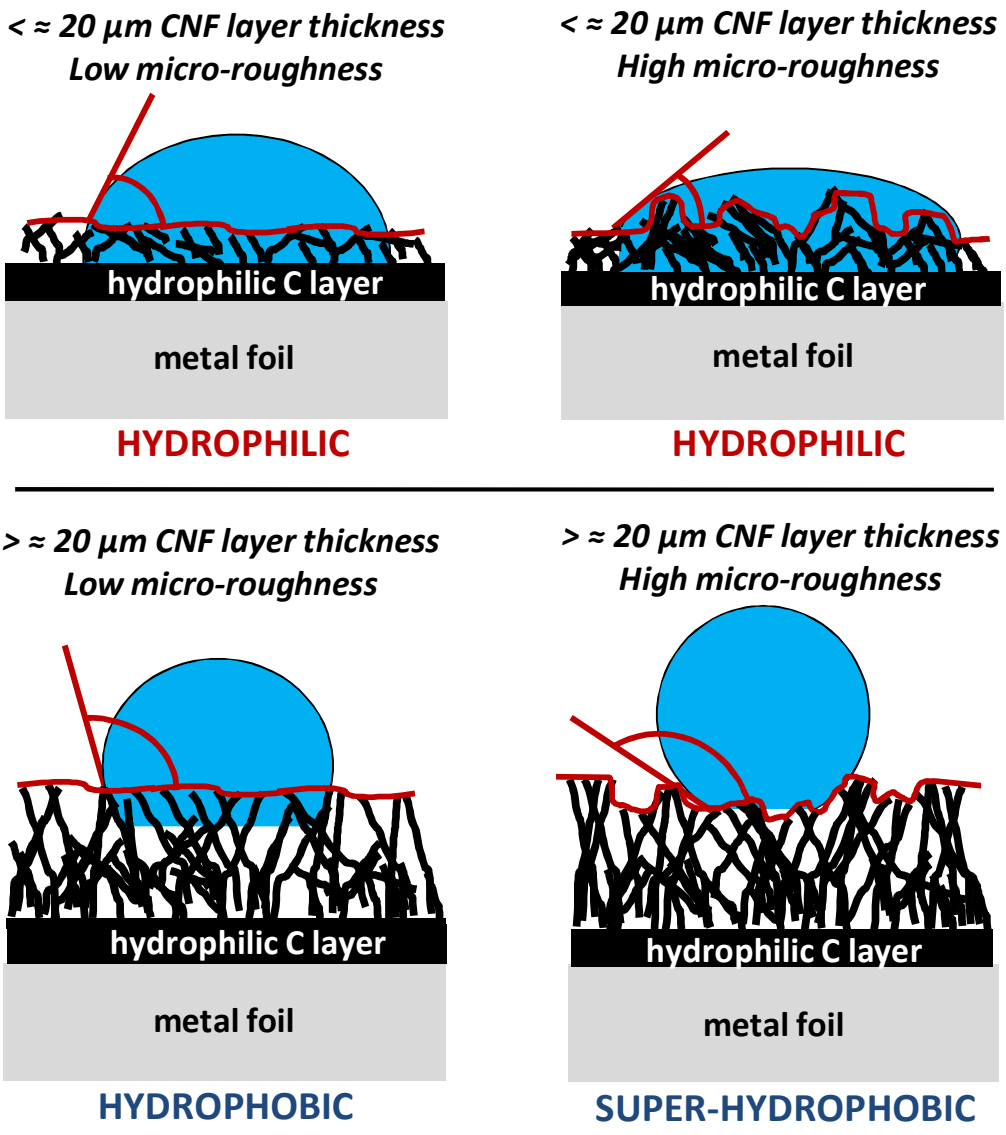

Figure 6.12: *proposed wetting and non-wetting states for well attached CNF layers on a Ni foil. For CNF layer thicknesses lower than ~20µm, the water droplet penetrates into the CNF layer making contact with the hydrophilic C layer, causing a wetted state. For CNF layer thicknesses larger than 20µm, the CA is higher than 90°, reaching a super-hydrophobic state at high surface roughness*

When the CNF layer is thinner than 20μm and has low micro-roughness, the surface is hydrophilic (**figure 6.12**). In this case water probably penetrates deep enough to contact the hydrophilic C layer under the CNF layer, leading to a wetted state. The CA further decreases with surface roughness and porosity because the CNF surface area also decreases concurrently because the diameter of the fibers is constant (typically 50nm). Consequently, less energy is needed to wet the CNF surface and the contact angle thus decreases further. However, for CNF layers thicker than 20μm, the surface becomes hydrophobic (**figure 6.12**). In this case, water droplets cannot penetrate enough to touch the hydrophilic C layer; therefore the droplet is accommodated on the surface of the CNF porous layer, in accordance to the Cassie-Baxter state. With increasing surface micro-roughness, the droplet penetrates even less into the CNF layer leading to super-hydrophobic surfaces.

6.5 Conclusions

CNF layer thickness, roughness and porosity are manipulated by the growth reaction conditions, resulting in a series of Ni foils covered with varying thicknesses of both the CNF layer as well as the C layer in between the Ni foil and CNF layer. Also, the surface roughness and porosity of the CNF layer was determined. The water wetting properties of the samples are more significantly influenced by the CNF layer thickness than the surface roughness and porosity. When the CNF layer is thicker than approximately 20μm, the surface is hydrophobic and the contact angle increases with surface roughness and porosity. When CNF layer is thinner than ca. 20μm, the surface is hydrophilic and the contact angle decreases with surface roughness and porosity. This behavior is attributed to penetration of the water droplet, making contact with the hydrophilic C layer between the CNF layer and the Ni foil.

Acknowledgements

I would like to thank the Department of Mechanical Engineering and the group Soft Matter, Fluidics and Interfaces of the University of Twente for letting me use the MeX® software and the contact angle meter, respectively. I also thank Hrudya Nair for fruitful discussions and on-going collaboration on the wettability related topic.

References

[1] N.M. Rodriguez, J. Mater. Res. 8 (1993) 3233.

[2] R.T.K. Baker, Carbon 27 (1989) 315.

[3] K.P. De Jong, J.W. Geus, Catal. Rev. Sci. Eng. 42 (2000) 481.

[4] V.V. Chesnokov, R.A. Buyanov, Russ. Chem. Rev. 69 (2000) 623.

[5] K.B.K. Teo, C. Singh, M. Chhowalla, W.I. Milne, in: H.S. Nalwa, (Eds.) Encyclopedia of Nanoscience and Nanotechnology, vol 10 (2003) p.1.

[6] R.H. Baughman, A.A. Zakhidov, W.A. De Heer, Science 297 (2002) 787.

[7] P. Serp, M. Corrias, P. Kalck, Appl. Catal. A 253 (2003) 337.

[8] P.M. Ajayan, Chem. Rev. 99 (1999) 1787.

[9] J.K. Chinthaginjala, J.H. Bitter, L. Lefferts, Appl. Catal. A 383 (2010) 24.

[10] N.M. de Almeida Coelho, J.L.B. Furtado, C. Pham-Huu, R. Vieira, Mater. Res. 11 (2008) 353.

[11] C. Pham-Huu, M.J. Ledoux, Top. Catal. 40 (2006) 49.

[12] J.K. Chinthaginjala, K. Seshan, L. Lefferts, Ind. Eng. Chem. Res. 46 (2007) 3968.

[13] K. Lee, J. Zhang, H. Wang, D.P. Wilkinson, J. Appl. Electrochem. 36 (2006) 507.

[14] R. Kannan, V.K. Pillai, J. Indian Inst. Sci. 89 (2009) 425.

[15] R. Chetty, S. Kundu, W. Xia, M. Bron, W. Schuhmann*et al*., Electrochim. Acta 54 (2009) 4208.

[16] R. Strobel, J. Garche, P.T. Moseley, L. Jorissen, G. Wolf, J. Power Sources 159 (2006) 781.

[17] B. Panella, M. Hirscher, S. Roth, Carbon 43 (2005) 2209.

[18] M.H. Al-Saleh, U. Sundararaj, Carbon 47 (2009) 2.

[19] E. Hammel, X. Tang, M. Trampert, T. Schmitt, K. Mauthner*et al*., Carbon 42 (2004) 1153.

[20] D. Hulicova-Jurcakova, X. Li, Z. Zhu, R. de Marco, G.Q. Lu, Energy and Fuels 22 (2008) 4139.

[21] M. Trojanowicz, Trends Anal. Chem. 25 (2006) 480.

[22] P.C. Tsai, S. Pacheco, C. Pirat, L. Lefferts, D. Lohse, Langmuir 25 (2009) 12293.

[23] A. Yan, X. Xiao, I. Kulaots, B.W. Sheldon, R.H. Hurt, Carbon 44 (2006) 3116.

[24] S.C. Ramos, G. Vasconcelos, E.F. Antunes, A.O. Lobo, V.J. Trav*æt al*., Diamond Relat. Mater. 19 (2010) 752.

[25] J. Rafiee, M.A. Rafiee, Z.Z. Yu, N. Koratkar, Adv. Mater. 22 (2010) 2151.

[26] H.J. Li, X.B. Wang, Y.L. Song, Y.Q. Liu, Q.S. Li*et al*., Angew. Chem., Int. Ed. 40 (2001) 1743.

[27] C. Journet, S. Moulinet, C. Ybert, S.T. Purcell, L. Bocquet, Europhys. Lett. 71 (2005) 104.

[28] K.K.S. Lau, J. Bico, K.B.K. Teo, M. Chhowalla, G.A.J. Amaratunga *et al.*, Nano Lett. 3 (2003) 1701.

[29] Y.C. Hong, D.H. Shin, H.S. Uhm, Surf. Coat. Technol. 201 (2007) 5025.

[30] Y.C. Hong, D.H. Shin, S.C. Cho, H.S. Uhm, Chem. Phys. Lett. 427 (2006) 390.

[31] K. Jian, A. Yan, I. Külaots, G.P. Crawford, R.H. Hurt, Carbon 44 (2006) 2102.

[32] D. Martial, M.P. Rossi, B.M. Kim, G. Korneva, H.H. Bau*et al*., J. Phys. Chem. B 110 (2006) 9850.

[33] W. Xia, C. Jin, S. Kundu, M. Muhler, Carbon 47 (2009) 919.

[34] T.G. Ros, A.J. Van Dillen, J.W. Geus, D.C. Koningsberger, Chem.-Eur. J. 8 (2002) 1151.

[35] O. Byl, J. Liu, J.T. Yates Jr, Langmuir 21 (2005) 4200.

[36] W. Brandl, G. Marginean, Thin Solid Films 447-448 (2004) 181.

[37] X. Feng, L. Jiang, Adv. Mater. 18 (2006) 3063.

[38] L. Feng, S. Li, Y. Li, H. Li, L. Zhang*et al*., Adv. Mater. 14 (2002) 1857.

[39] X. Zhang, F. Shi, J. Niu, Y. Jiang, Z. Wang, J. Mater. Chem. 18 (2008) 621.

[40] A. Nakajima, K. Hashimoto, T. Watanabe, Monatsh. Chem. 132 (2001) 31.

[41] X.M. Li, D. Reinhoudt, M. Crego-Calama, Chem. Soc. Rev. 36 (2007) 1350.

[42] M.L. Ma, R.M. Hill, Curr. Opin. Colloid Interface Sci. 11 (2006) 193.

[43] R. Blossey, Nat. Mater. 2 (2003) 301.

[44] P. Joseph, C. Cottin-Bizonne, J.M. Benoit, C. Ybert, C. Journet *et al*., Phys. Rev. Lett. 97 (2006).

[45] J. Ou, B. Perot, J.P. Rothstein, Phys. Fluids 16 (2004) 4635.

[46] J. Hyväluoma, J. Harting, Phys. Rev. Lett. 100 (2008).

[47] R.N. Wenzel, Ind. Eng. Chem. 28 (1936) 988.

[48] A.B.D. Cassie, S. Baxter, Trans. Faraday Soc. 40 (1944) 546.

[49] H. Gelderblom, A.G. Marin, H. Nair, A. van Houselt, L. Lefferts *et al.*, Phys. Rev. E 83 (2011) 026306.

[50] K. Gjerde, R.T.R. Kumar, K.N. Andersen, J. Kjelstrup-Hansen, K.B.K. Teo *et al.*, Soft Matter 4 (2008) 392.

[51] H. Liu, J. Zhai, L. Jiang, Soft Matter 2 (2006) 811.

[52] T. Sun, L. Feng, X. Gao, L. Jiang, Acc. Chem. Res. 38 (2005) 644.

[53] N. Michael, B. Bhushan, Microelectron. Eng. 84 (2007) 382.

[54] C.W. Extrand, Langmuir 20 (2004) 5013.

[55] J. Wang, D. Chen, Langmuir 24 (2008) 10174.

[56] P. van der Wal, U. Steiner, Soft Matter 3 (2007) 426.

[57] Z. Yoshimitsu, A. Nakajima, T. Watanabe, K. Hashimoto, Langmuir 18 (2002) 5818.

[58] L. Gao, T.J. McCarthy, Langmuir 22 (2006) 2966.

[59] D. Öner, T.J. McCarthy, Langmuir 16 (2000) 7777.

[60] I. Morcos, J. Colloid Interface Sci. 34 (1970) 469.

[61] M.E. Schrader, J. Phys. Chem. 79 (1975) 2508.

[62] Y. Zhou, B. Wang, X. Song, E. Li, G. Li *et al.*, Appl. Surf. Sci. 253 (2006) 2690.

[63] S. Pacheco Benito, L. Lefferts, Carbon 48 (2010) 2862.

[64] W.S. Rasband, http://rsb.info.nih.gov/ij/download.html.

[65] J. Löberg, I. Mattisson, S. Hansson, E. Ahlberg, The Open Biom. J. 2 (2010) 18.

[66] P. Schwaller, R. Züst, J. Michler, J. Therm. Spray Tech. 18 (2009) 96.

[67] Z. Burton, B. Bhushan, Ultramicroscopy 106 (2006) 709.

[68] J.K. Chinthaginjala, D.B. Thakur, K. Seshan, L. Lefferts, Carbon 46 (2008) 1638.

[69] N.J. Shirtcliffe, S. Aqil, C. Evans, G. McHale, M.I. Newton *et al.*, Microeng. 14 (2004) 1384.

[70] A.M. Peters, C. Pirat, M. Sbragaglia, B.M. Borkent, M. Wessling *et al.*, Eur. Phys. J. E 29 (2009) 391.

[71] M.E. Schrader, J. Phys. Chem. 84 (1980) 2774.

[72] L. Zhang, D.E. Resasco, Langmuir 25 (2009) 4792.

[73] J. Yang, Z. Zhang, X. Men, X. Xu, X. Zhu, J. Colloid Interface Sci. 346 (2010) 241.

[74] C. Luo, X. Zuo, L. Wang, E. Wang, S. Song *et al.*, Nano Letters 8 (2008) 4454.

[75] C. Luo, H. Zheng, L. Wang, H. Fang, J. Hu *et al.*, Angew. Chem., Int. Ed. 49 (2010) 9145.

[76] D. Bartolo, F. Bouamrirene, É. Verneuil, A. Buguin, P. Silberzan *et al.*, Europhys. Lett. 74 (2006) 299.

[77] M. Nosonovsky, B. Bhushan, Langmuir 24 (2008) 1525.

[78] N.J. Shirtcliffe, G. McHale, S. Atherton, M.I. Newton, Adv. Colloid Interface Sci. 161 (2010) 124.

[79] J. Drelich, J.D. Miller, R.J. Good, J. Colloid Interface Sci. 179 (1996) 37.

[80] S. Vafaei, M.Z. Podowski, Adv. Colloid Interface Sci. 113 (2005) 133.

[81] N.A. Patankar, Langmuir 20 (2004) 7097.

Chapter 7

Conclusions and recommendations

"The best way to cheer yourself up is to try to cheer someone else up" (Mark Twain)

The work presented in this thesis describes the preparation of carbon nanofiber (CNF) layers on flat and porous substrates and their application as catalyst supports for chemical and electrochemical gas-liquid-solid (G-L-S) catalytic reactions. The first part focuses on the synthesis of homogenous and well-attached CNF layers on metal flat substrates. The second part focuses on the preparation and catalytic evaluation of metal loaded CNF layers grown on porous substrates. The final part gives some insight into the water wettability of CNF layers.

7.1 Preparation of CNFs on metal substrates

Carbon, including CNFs, was deposited on metal foils including nickel (Ni), iron (Fe), cobalt (Co), stainless steel (Fe:Ni 70:11wt%) and mumetal (Ni:Fe 77:14wt%) by the decomposition of C_2H_4 at 600°C. Ni is especially active for carbon formation after oxidation pretreatment, particularly when H_2 is added to the stream. Mumetal shows the highest carbon growth rate for all combinations of pretreatments and addition of H_2, but it is especially active after a pretreatment including an oxidation step. The presence of oxidized Ni and Cu in mumetal, in combination with the addition of H_2, is responsible for the high rates on mumetal. Generally speaking, the diameters of CNFs deposited on metal alloys, namely mumetal and stainless steel, are thicker than pure metals. Co and Fe generally grow thin CNFs. Metal nanoparticles growing CNFs are easily formed from NiO, in contrast to Fe and Co oxides, leading to higher carbon deposition rates. However, high activity towards total carbon deposition is generally detrimental for obtaining well-attached and homogenously distributed CNFs, as mainly occurs with Ni and mumetal. CNFs grown from Co and Fe foils are averagely well-attached but not homogenously distributed. Stainless steel presents homogeneous and well-attached CNFs at relatively low carbon growth rates.

Due to the high activity of Ni at 600°C for CNF formation, the second part studies the attachment of CNF layers grown at much lower temperature, *i.e.* 450°C, in presence of different H_2 concentrations and for different reaction times. Dense carbon (C) and entangled CNF layers are deposited on all Ni foils after either oxidation or oxidation-reduction pretreatments. CNFs are more crystalline than

the C layer, although the addition of H_2 during the reaction increases the amount of defects. Both C and CNF layer thicknesses increase with growth time, but the mechanical stability decreases with growth time, especially for oxidized-reduced samples. Thus, samples oxidized at 500°C generally show better mechanical stability than oxidized-reduced samples at 700°C. Oxidized and oxidized-reduced samples present a maximum in the CNF layer thickness, at 5% and 20% H_2 concentration respectively, which coincides with a minimum in the C layer thickness. The stability of the CNF layer is determined by the ratio between the thickness of the C layer and the CNF layer. When the ratio is higher than 0,2, the carbon weight loss is smaller than 7%. For lower ratios the carbon weight loss can increase up to 85%. Therefore, the preparation of stable and thick CNF layers on Ni foils involves a compromise between the deposition of a thick C layer and the amount of weakly attached CNFs.

7.2 Synthesis and application of CNF layers as catalyst support

The second part of the thesis focuses on the growth of CNF layers on porous substrates, the deposition of metal nanoparticles and their performance in a catalytic reaction. First, we report the fabrication and operation of a hybrid metallic-membrane reactor for the catalytic reduction of nitrite (NO_2^-), in an aqueous solution, with H_2. The microreactor consists of a porous stainless steel tube onto which a CNF layer is grown at 700°C. Pd nanoparticles deposition on the CNFs is performed on few samples; but all samples, with or without Pd, are finally externally encapsulated by a H_2 permeable membrane coating. Such reactors benefit from a controlled G-L-S interface of a membrane reactor and high surface area of carbon nanofibers as catalyst support. The presence of the CNFs on the stainless steel surface had a significant effect on the reactor performance. Even without the presence of H_2 and Pd, the NO_2^- ions were successfully reduced, which was confirmed by the disappearance of NO_2^- reactant and formation of ammonia (NH_4^+). These results indicate the reductive properties of the CNF coated reactor. We proposed that the reductive properties of Fe nanoparticles, which are located at the tip of the grown CNFs, are responsible for the reduction of NO_2^- without hydrogen supply. However, the Pd containing samples show a higher NO_2^- conversion which proceeds by the combination of both reductive catalytic

properties of Pd in presence of H_2 and the Fe containing CNFs. Eventually, the latter effect will exhaust in time and the reaction will still proceed with the immobilized Pd-catalyst on the CNFs and the membrane-assisted supply of H_2.

Second, we report the growth of a CNF layer on a carbon paper substrate for polymer exchange membrane (PEM) fuel cell applications, more specifically for the electrocatalytic oxygen reduction reaction (ORR). Ni nanoparticles were previously deposited on the carbon paper as catalyst for the CNF growth at 450°C. Subsequently, Pt nanoparticles were deposited directly on the top of the CNF layer by a sputtering method and a chemical method based on the *in-situ* reduction of Pt with ethylene glycol, named polyol method. Pt nanoparticles are more superficially located when sputtered than Pt when deposited by the polyol method. However, the average Pt particle size increases with Pt loading for sputtered samples, whereas the size and Pt location in the CNF layer does not change significantly for the polyol method at different loadings. The Pt electrochemical surface area, when deposited on CNFs, is much higher than that obtained for commercial Pt/Vulcan independent of the method used. However, sputtered samples have lower catalytic activity for the ORR than samples prepared by the polyol method with similar Pt loading and particle size. The intrinsic ORR kinetic current increases with Pt loading and is higher for samples prepared by the polyol method for relatively lower loadings than Pt/Vulcan. Samples prepared by the polyol method suffer more from internal mass transfer limitations than Pt/Vulcan due to a deeper Pt location. However, the external oxygen diffusion is higher for Pt/CNFs, as compared to Pt/Vulcan, due to the intrinsic morphology of the CNFs that allow a better accessibility to oxygen diffusion.

7.3 Wettability of CNF layers

The last part of the thesis aims at gaining understanding of the water wettability of the CNF layers that can have application is microfluidic devices including microreactors as well as multi-phase microstructured reactors, and for deposition of metal nanoparticles in aqueous phase. For the study we grow CNF layers on Ni foils at 450°C using different H_2 concentrations and reaction times. The CNF roughness and porosity, and the thickness of both the CNF layer as well as the C layer in between the Ni foil and CNF layer are manipulated by the growth

reaction conditions. The addition of 5% H_2 produces thicker, rougher and more porous CNF layers than when 1% H_2 is used. The roughness and porosity increases with reaction time when 5, 10 or 20% H_2 are used; however, this effect is less pronounced when 1%H_2 is used. CNFs are 50-55nm in diameter and have a fishbone type structure. The water wetting properties of the samples are more significantly influenced by the CNF layer thickness than both surface roughness and porosity. When the CNF layer is thicker than ca. 20μm, the surface is hydrophobic and the contact angle increases with surface roughness and porosity. When the CNF layer is thinner than ca. 20μm, the surface is hydrophilic and the contact angle decreases with increasing surface roughness and porosity. This behavior is attributed to penetration of water, making contact with the hydrophilic C layer.

7.4 Recommendations

In the first part of the thesis we observed that Ni based materials are prone to deposit carbonaceous deposits with relatively higher yield as compared to Co and Fe materials. CNFs were grown as temperatures as low as 450°C; however, in order to decrease production costs further, it is suggested to study the minimum temperature necessary for CNF growth after oxidation pretreatments and low amounts of H_2 concentration for instance. Moreover, we saw that the presence of Cu in the Ni foil increases further the carbon yield compromising the attachment. Therefore, the study of addition of small amounts of Cu in Ni materials for the formation of high yield of CNF powders to be used later as catalyst support can be explored.

We observed the important role of the apparently dense carbon layer in the attachment of the CNFs to the substrate. It appears that a balance between the amount of CNFs deposited and the thickness of the C layer is needed. However it is not clear where exactly the CNFs start growing so that the attachment to the substrate becomes better. It is recommended to perform some *in-situ* SEM or TEM characterization to gain more insight about this issue. Moreover, the role of the addition of H_2 depending on the pretreatment on the metal foil is still not clearly understood. It is recommended to perform experiments at very low H_2 concentration during the first seconds of the reaction to study the effect on

fragmentation of the metal particles and on the growth of the C and CNF layer, depending on the pretreatment.

Regarding the study of the porous microreactors, we observed an intrinsic reductive capability of the Fe particles at the top of the CNFs for nitrite hydrogenation in aqueous solution. It is recommended to study the duration of their reductive activity in presence and absence of H_2. Moreover it is suggested to study the catalytic activity of Fe nanoparticles, or alloys with Pd nanoparticles, deposited on CNFs, as compared to the performance of Pd nanoparticles.

The porous carbon materials based on Pt deposited on a CNF layer opens a promising approach for making new electrodes *via* direct CNF growth and direct Pt nanoparticles deposition. However, electrochemical techniques, such as impedance spectroscopy, need to be optimized to gain insight into mass transport limitations of the relatively thick electrodes that contain catalyst layers, as practically used in fuel cells, instead of conventional studies of thin catalyst layers. Moreover, for the fuel cell test the assembly of these new electrodes with a membrane, such as Nafion®, needs an optimization of the Nafion content and hot press conditions, as well as a better understanding of the interaction of water internally in the CNF layer at the fuel cell conditions.

CNF layers have shown to be either hydrophobic or hydrophilic, depending on the thickness, porosity and roughness of the CNF layer, after placing a small water droplet on them. However, the study of the evolution of the droplet in time, and the advancing and receding contact angles (by adding or removing water) would give more information about the stability of the CNF layers. Moreover, the study of the depth of penetration of water inside the CNF layer would confirm possible interactions with the underneath hydrophilic C layer. Also, studies of different droplets sizes might help in understanding possible effects of roughness, especially at nano-level, of the CNF layers; in the latter case the use of environmental SEM might be of interest.

List of publications

- S. Pacheco Benito, L. Lefferts: **"The production of a homogeneous and well-attached layer of carbon nanofibers on metal foils"**
  Carbon 2010, 48 (10) 2862-72

- P.C. Tsai, S. Pacheco Benito, C. Pirat, L. Lefferts, D. Lohse: "**Drop Impact upon Micro- and Nanostructured Superhydrophobic Surfaces**"
  Langmuir 2009, 25 (20) 12293-8.

- S. Pacheco Benito, L. Lefferts: **"Wettability of carbon nanofiber layers deposited on nickel foils"**
  Journal of Colloid and Interface Science 2011 (in press)

- H.C. Aran, S. Pacheco Benito, M.W.J. Luiten-Olieman, S. Er, M. Wessling, L. Lefferts, N. E. Benes, R.G.H. Lammertink: **"Carbon nanofibers in catalytic membrane microreactors**"
  Journal of Membrane Science 2011, 381 (1-2) 244-250

- S. Pacheco Benito, L. Lefferts: "**Influence of reaction parameters on the attachment of a carbon nanofiber layer on Ni foils**"
  Surface and Coating Technology (submitted)

- S. Pacheco Benito, G. Cadafalch Gazquez, M. Duca, G.E.L Merle, J.R.C. Salgado, K. Nijmeijer, M. Koper, L. Lefferts. "**CNF layers grown on carbon microfibers and direct one-side only Pt nanoparticles deposition for PEM fuel cells**"
  Journal of Power Sources (in preparation)

- Tuzovskaya, S. Pacheco Benito, J.K. Chinthaginjala, C. Reed, L. Lefferts, T. van der Meer: "**Heat exchange performance of stainless steel and carbon foams modified with carbon nano fibers**"
  (in preparation)

- Anil V. Gaikwad, Tapan K. Rout,Dirk Van der Plas, S. Pacheco Benito, L. Lefferts, Robert V. Dennis, Sarbajit Banerjee. *"**Homogeneous and Strongly Adhered Layers of Carbon Nanotubes on Sheet Metal Surfaces from Feedstock Typical of Industrial Effluent**"*
  (in preparation)

Conference presentations

- Oral presentation: "*In-situ growth of hydrophobic CNF layers on carbon microfibers and direct one-side only Pt deposition for PEM fuel cell applications*". Carbon conference. **Shangai (China)**, 2011

- Poster: "*Hydrophobic carbon nanostructured layer as bi-functional gas diffusion media and catalyst support for PEM fuel cells*". Impact, Energy & Resources Symposium. **Enschede (Netherlands)**, 2011

- Poster (best poster prize): "*Hydrophobic carbon nanostructured layer as bi-functional gas diffusion media and catalyst support for PEM fuel cells*". Nanomaterial Issues in Electrochemical Energy Conversion: Fuel Cells, Batteries, Supercapacitors. **Helsinki (Finland)**, 2011

- Oral presentation: "*In-situ growth of hydrophobic CNF layers on carbon microfibers and direct one-side only Pt deposition for PEM fuel cell applications*". 2nd Advances in H_2 & Fuel Cells Conference. **Rotterdam (Netherlands)**, 2011

- Poster: "*Hydrophobic carbon nanostructured layer as bi-functional gas diffusion media and catalyst support for PEM fuel cells*". XIIth Netherlands' Catalysis and Chemistry Conference (NCCC). **Noordwijkerhout (Netherlands)**, 2011

- Oral presentation: "*Hydrophobic carbon nanostructured layer as bi-functional gas diffusion media and catalyst support for PEM fuel cells*". 1st International Conference on Materials for Energy. **Karlsruhe (Germany)**, 2010

- Oral presentation: "*Effect of morphology and surface chemistry on the wettability of carbon nanofiber layers*" XIth NCCC. **Noordwijkerhout (Netherlands)**, 2010

- Oral presentation - poster: "*Effect of porosity and thickness of the carbon layer on the hydrophobicity of carbon nanofiber layers*". Faraday Discussions 146. **Richmond-Virginia (USA)**, 2010

- Oral presentation: "*Tunable wettability on carbon nanofibers: towards a super-hydrophobic surface*" Carbon conference. **Biarritz (France)**, 2009

- Poster: "*Tunable wettability on carbon nanofibers: towards a super-hydrophobic surface*". Xth NCCC. **Noordwijkerhout (Netherlands)**, 2009

- Poster: "*Carbon nanofiber jungles: towards a switchable super-hydrophobic surface*". Mesa+ Annual Meeting, **Enschede (Netherlands)**, 2008

- Oral presentation: "*The dynamics of droplet impact upon carbon nanofibre jungles*". 7th Euromech Fluid Mechanics Conference. **University of Manchester (United Kingdom)**, 2008

- Poster (best poster prize): "*Carbon nanofiber jungles: towards a switchable super-hydrophobic surface*". IXth NCCC . **Noordwijkerhout (Netherlands)**, 2008

Acknowledgments

It has taken more than 4 years to succeed in finishing the present PhD thesis and now it is time to thank the people that have contributed to this success. First of all I would like to thank Prof. Leon Lefferts for giving me the opportunity to pursue a PhD despite my mixed background and my limited knowledge on catalysis. I appreciate your guidance, availability and your demanding and critical behavior, despite the disagreements and the efforts to sometimes reach clarity.

I also thank the other staff members of the Catalytic Processes and Materials group of the University of Twente, Prof. Seshan, Dr. Barbara and Dr. Arie for valuable discussions and their efforts of managing the CPM group and organizing various formal and informal activities. I also thank the CPM secretaries that I have seen during my PhD, Sabine, Lidy and Lianne, thanks for your help with administrative and practical things at various stages during my PhD project. Sabine, I especially appreciate your administrative support for a recent project proposal, independent of the result, despite the last minute notice.

Bert, I appreciate your technical, IT and financial support, as well as a good mediation between PhDs and Postdocs and the staff members. Louise, many thanks for the Dutch translation and your always attentive attitude for XRF and BET characterization, apart from fruitful discussions that led to a collaboration in one chapter of the present thesis. Karin, you have greatly contributed to make our labs an organized, clean and safe place to work, thank you for that and for the attempts of chemisorption characterization. Ruben and Tom, many thanks for the technical support that you have provided, not just to my project, but also to the project of the other PhDs and Postdocs. The organization of informal activities, in and outside CPM, for sure helps to motivate us and to know each other better.

I also appreciate the work of MESA+ employees that certainly had an impact in the characterization of the materials included in this thesis. Mark, thanks for SEM and TEM characterization as well as your critical and humorous aptitude. Rico, thanks for your refined TEM experience and discussions. Thank you Gerard for the XPS analysis and valuable discussions. I also thank the IMS group, especially Tomasz, for the assistance provided to use the XRD facilities.

Regarding external collaborations, I would like to thank Dr. Amy for her perseverance and motivation to good work. I also thank Dr. Alvaro for valuable discussions and in general the POF group for the active collaboration with CPM. Can, sincerely thanks for your proactive aptitude and openness towards research, and the SFI and IM group for the collaboration. I also thank Erik and Gerard for the fruitful collaborations, and generally the MTG for letting me use their facilities. Dr. Roald, thanks for your support in some parts of the project and your aptitude to collaborate. I thank Dr. Chieh-Chao, Liza and generally the MCS and PCS groups, for informal and formal discussions. I also appreciate the past and on-going collaboration with Dr. Tapan and Dr. Anil from Tata Steel Company.

I especially want to thank the CNF cluster of the CPM group: Dr. Kumar, Dr. Vijay, Dr. Inga, Dr. Zelko, Hrudya, Joline, Chau and Roger, for the interesting discussions on various aspects of the carbon nanostructures world that have led to past and present collaborations, and hopefully will continue in the future. Chris, thanks for valuable discussions on various topics and for the English corrections. I would also like to thank other current and ex-CPM members: Dr. Jose, Dr. Yejun, Dr. Patrick, Dr. Gacia, Dr. Dejan, Marijana, Dennis, Rao, Yingnan, Masoud, Arturo, Kamila, Gonzalo, Darren, Ifeanyi, Rijan, Maisha, Lars, Bart, Martine, Jann, Martine, Jeroen and Hans, that *via* formal or informal discussions, have also contributed to the realization of this thesis and have contributed to more scientific interactions. Since some of you might expect a bit more from me, a more personal comment will follow personally. For the moment, especial thanks to my dear Paranymphs Son and Shilpa, it is an honor to have you accompanying me during my PhD defense.

I also want to remember all the P-NUT members that I have met during my PhD: Marije, Michel, Maryana, Nicolas, Aimee, Anika, Shashank, Nikolay, Josine, Bjorn, Nicole, Giovane, Juan Carlos, Juan and Silja. Thank you all for working for a good cause. I also thank Dirk from the University of Delft and Davide from the University of Utrecht for taking part in the NIOK PhD platform.

Gracias a JJ, Txemuki, Tigre, Xuba, Dani y Alberto por acompañarme en este viaje de mi vida. Finalmente, gracias a mis padres Laureano y Mercedes por haber apagado la tele hace unos 33 años, a mis hermanos Yolanda y Rober, mis cuñados Aida y Jose Mari y mis sobrinillos Ander y Unai. A todos, gracias por existir. Agur.

Sudoku

		1						
		2		3				4
			5			6		7
5			1	4				
	7						2	
				7	8			9
8		7			9			
4				6		3		
						5		

Find 10 differences

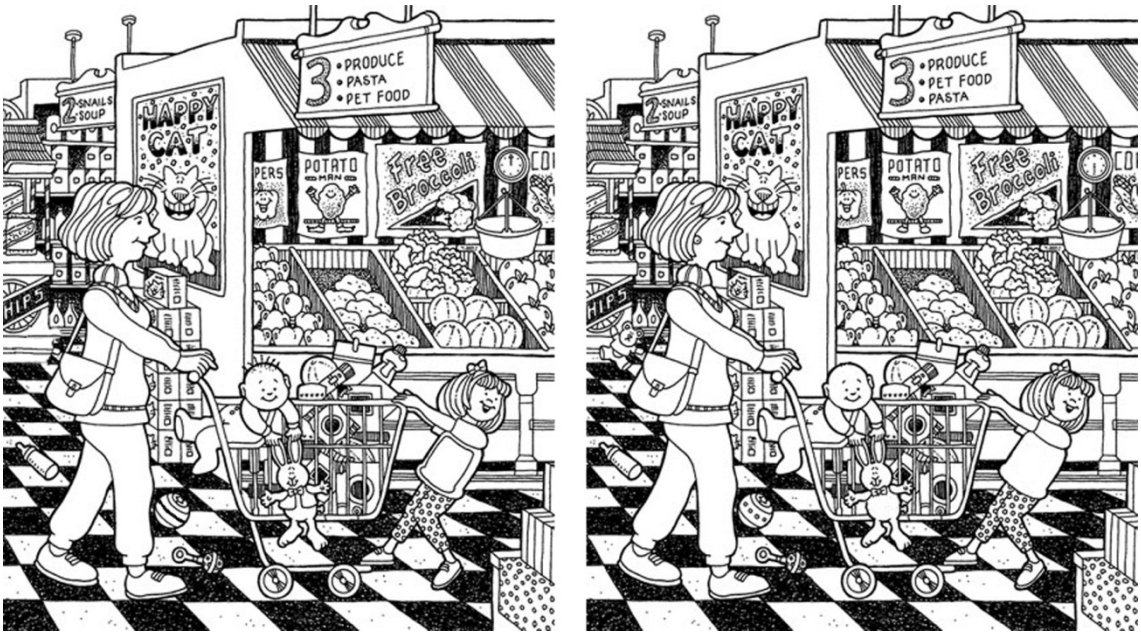

"Love is the difficult realization that something other than oneself is real" (Iris Murdoch)

"The ability to ask questions is the greatest resource in learning the truth" (unknown)

*"The only thing I know is that I do not know what I know, or not" (*myself)